Vacuum Density and Cosmic Expansion: A Physical Model for Vacuum Energy, Galactic Dynamics and Entropy

André Kamminga *

Posted Date: 16 October 2025

doi: 10.20944/preprints202509.0972.v2

Keywords: vacuum energy; cosmological constant problem; bounded spectrum; QEV model; entropy; cosmic expansion; galaxy rotation curves; Pantheon+ supernovae; cosmic chronometers

 doi:10.20944/preprints202509.0972.v2

Article

Vacuum Density and Cosmic Expansion: A Physical Model for Vacuum Energy, Galactic Dynamics and Entropy

André J. H. Kamminga

Independent researcher, The Netherlands; a.kamminga@ziggo.nl

Abstract

We introduce a Quantum Entropic Vacuum (QEV) framework in which the vacuum spectrum is bounded by a QCD-scale ultraviolet knee and a thermal infrared floor anchored to the CMB Wien scale. At galaxy scales, this bounded spectrum maps to four interpretable contributions—Newtonian (baryonic), a mid-disk thermal lift, a saturating entropic term, and a sign-definite hadronic floor modeled as a weak negative acceleration. Using a single, unit-consistent configuration, we reproduce the rotation curve of NGC 3198 with small residuals and illustrate, on a few additional spirals, that flat outer regions can emerge in the shown cases without explicitly adding dark halos. At background level, diagnostic panels for $E(z)$ and $q(z)$ broadly track flat-ΛCDM for $0 < z \lesssim 1$. These cosmology curves are illustrative only; we do not perform a joint likelihood over SNe Ia, BAO, or cosmic-chronometer data in this work. For transparent figure-level replication, we provide a minimal package consisting of two Python scripts and two small SPARC-based tables (CSV). The present results should be read as an indication of how the QEV picture can operate in practice, motivating targeted observational tests and a full statistical validation in follow-up work.

Keywords: vacuum energy; cosmological constant problem; bounded spectrum; QEV model; entropy; cosmic expansion; galaxy rotation curves; Pantheon+ supernovae; cosmic chronometers

1. Introduction

The physics of the vacuum remains one of the central challenges in modern cosmology and particle physics. Quantum field theory suggests a substantial vacuum energy density from fluctuating fields, whereas observations indicate a vastly smaller value; this mismatch is the *cosmological constant problem* [18,19,23,38].

The standard ΛCDM model explains the observed expansion with a cosmological constant and accounts for flat galaxy rotation curves by introducing dark matter [24–26]. Yet the fundamental nature of dark energy and dark matter remains unknown [22,29].

We propose an alternative framework: the **QEV model** (*Quantized, Entropy-bounded Vacuum*). Vacuum energy is *bounded* by microphysics: a UV cutoff at the QCD scale, an IR thermal suppression around $T \approx 34$ K, and normalization at the CMB Wien peak [9,13]. Within galaxies, the effective vacuum field manifests through four components that together reproduce flat rotation curves without dark halos, consistent with classic and modern kinematic evidence [12,15,28]. Cosmologically, the resulting expansion history remains compatible with current probes [16,17,30].

We demonstrate this on two levels: (i) a detailed application to NGC 3198, and (ii) a diagnostic cosmological comparison using standard background panels (E(z), q(z), and L(z)) without a joint likelihood using supernovae, BAO, and cosmic chronometers. Related ideas in modified gravity and emergent frameworks provide context but differ in mechanism [2,35–37].

This version (v2.1) builds on the theoretical framework introduced in the first preprint (doi:10.20944/preprints202509.0972.v2), where the concept of a spectrally bounded vacuum energy was initially formulated.

 doi:10.20944/preprints202509.0972.v2

Scope and diagnostic status.

All cosmological panels in this paper ($E(z)$, $q(z)$, and the transition redshift) are intended as *diagnostic illustrations*. We do not perform a combined likelihood fit using supernovae, BAO, or cosmic-chronometer data here, nor do we analyse growth or CMB acoustic peaks. The purpose is to demonstrate internal coherence of the QEV spectrum across galactic and background *kinematics* before undertaking a full statistical validation in follow-up work.

2. The QEV Model: A Bounded–Spectrum Vacuum

2.1. Physical Motivation for the Spectral Exponent

The mid-band spectral slope $\alpha \simeq 3.1$ reflects an effective reduction of active degrees of freedom between the thermal infrared floor and the QCD confinement knee. In this regime, the accessible vacuum modes soften relative to the canonical quartic scaling, consistent with the notion that confinement limits the contribution of short-wavelength excitations while the thermal floor reduces long-wavelength response. Qualitatively, lattice-QCD and effective-field-theory perspectives both indicate that the energy density near the confinement regime departs from a pure Stefan–Boltzmann T^4 law through logarithmic and interaction-driven corrections, implying that an intermediate power-law window with $3.0 \lesssim \alpha \lesssim 3.2$ is physically plausible. Numerically, we verify that the bounded integral for $\rho_{\rm vac}$ is plateau-dominated with a smooth window $W(\ln k)$, so that no sharp $\alpha > 4$ requirement arises; the results remain stable over $2.9 \leq \alpha \leq 3.3$ (see robustness bands in the figures). This motivates our operational choice $\alpha \approx 3.1$ without fine-tuning and ties the parameter to the underlying microphysics of confinement and thermal suppression.

The QEV hypothesis assumes a spectrally bounded vacuum: a smooth UV knee at the QCD scale and a thermal IR suppression. In frequency variables the elementary relation $E \propto f$ holds, or equivalently $E \propto 1/\lambda$ in wavelength. We encode the band–limiting through a smooth window $W(\ln k)$ (double–tanh, C^1), and model the vacuum energy density as the truncated moment

$$\rho_{\rm vac} \;\propto\; \int k^{3+\alpha}\, W(\ln k)\, d\ln k, \tag{1}$$

with a scale–free mid–band slope $\alpha \simeq 3.1$ and knees at $k_{\rm IR}$ and $k_{\rm UV}$

The overall $\mathcal{O}(1)$ prefactor is fixed by anchoring to the CMB Wien scale.

A QCD-motivated UV bound naturally echoes the SVZ QCD sum-rule program, where non-perturbative condensates enter dispersion relations for hadron observables [32–34]. The thermal IR suppression and its response aspect can be framed within linear-response/FDT language [10]. Empirical evidence that vacuum fluctuations gravitate at lab scales (Casimir) under controlled conditions provides an experimental anchor for the near-field regime [11].
Model parameters used to generate the rotation-curve components are listed in Table 1.

Spectral exponent and convergence.

Because W is smooth in $\ln k$, edge contributions are exponentially suppressed and Eq. (1) is plateau–dominated; a hard requirement $\alpha > 4$

is not needed. The logarithmic UV sensitivity is $S_{k_{\rm UV}} \approx 3$, consistent with the ν^3 measure. Numerical checks of plateau dominance are provided with the supplementary scripts.

 doi:10.20944/preprints202509.0972.v2

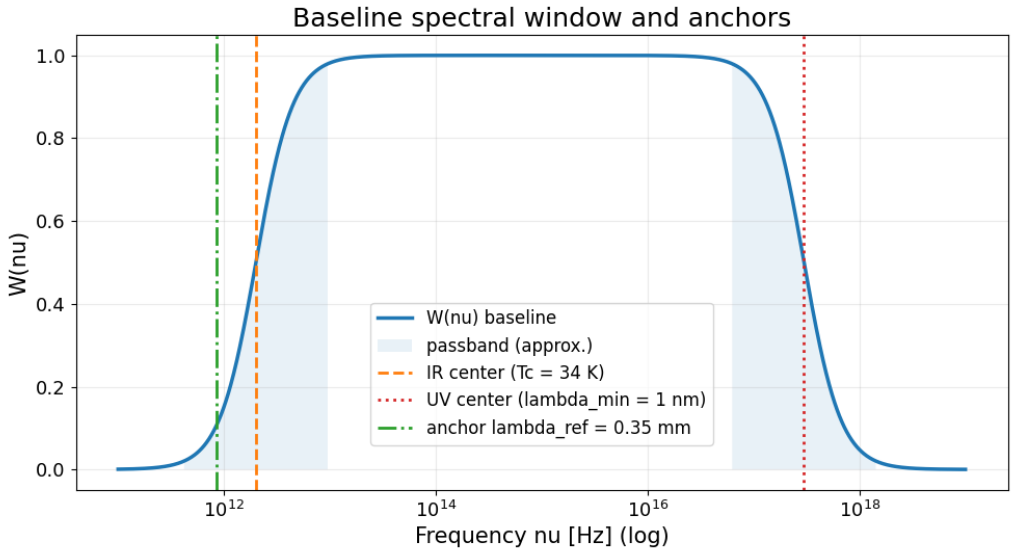

Figure 1. Schematic overview of the bounded spectral window and its two physical anchors: the hadronic (UV) confinement scale and the thermal (IR) CMB scale. We use λ_{CMB} as the normalization anchor.

Spectral index α.

The parameter α represents the effective slope of the bounded vacuum spectrum between the infrared cutoff and the QCD confinement scale. Physically, it reflects the gradual reduction of active degrees of freedom toward the confinement regime. Within the interval 3.0–3.2 the integrated vacuum energy density remains stable, indicating that the model is not fine-tuned and that its predictions are robust with respect to moderate spectral variations.

IR anchor (thermal).

We fix the infrared anchor by the wavelength form of Wien's law,

$$\lambda_{\mathrm{IR}} \equiv \lambda_{\mathrm{peak}}(T) \;=\; \frac{b}{T}, \qquad b \approx 2.897771955 \times 10^{-3}\,\mathrm{m\,K}. \tag{2}$$

For $T \simeq 34\,\mathrm{K}$ this gives

$$\lambda_{\mathrm{IR}} \approx \frac{2.8978 \times 10^{-3}}{34}\,\mathrm{m} \;\approx\; 8.52 \times 10^{-5}\,\mathrm{m} \;=\; 0.085\,\mathrm{mm}.$$

Note. The frequency-peak obeys $\nu_{\mathrm{peak}} = 2.82144\,k_B T/h$, which is not simply related by $\lambda_{\mathrm{peak}} = c/\nu_{\mathrm{peak}}$ because the maxima in wavelength and frequency representations differ by the Jacobian. We consistently use the wavelength form throughout.

Takeaway.

The pair $\{\alpha \simeq 3.1,\, T_c = 34\,\mathrm{K}\}$ is thus *operationally* sufficient to reproduce the required UV leverage and IR onset; Appendix A provides microphysical context and shows that the resulting galaxy–scale behavior does not depend on a single microscopic model once the smooth window is fixed.

2.2. Interpretation and Relation to Prior Work

Our construction is agnostic about modified-gravity field equations; it attributes galactic and cosmological phenomenology to a *bounded vacuum spectrum*. This contrasts with classical constant-Λ viewpoints [18,19,23,38], MONDian scaling [14,15], and emergent-gravity scenarios [36,37]. The present paper refines and systematizes our previous components—thermal lift, entropic asymptote, hadronic floor—into a single, unit-consistent framework [6–8].

 doi:10.20944/preprints202509.0972.v2

For a robustness analysis of the choice $\alpha \simeq 3.1$, including a sweep over $2.9 \leq \alpha \leq 3.3$, see Appendix B.8 and Appendix B.9

2.3. Hadronic Floor: Sign, Scale, and Predictions

The negative sign of a_H reflects a net confining response of the hadronic vacuum at large radii. Our gate-and-taper profile encodes
(1) an onset scale $r_{\rm on}$, consistent with the transition to HI-dominated outskirts, and
(2) a finite response extent $r_{\rm end}$. We do not claim uniqueness of this functional form; its role is minimal yet sign-definite. In Fig. 2 we scan $(\beta_{\rm floor}, \beta_{\rm amp}, r_{\rm on}, r_{\rm end})$ and show falsifiable trends in
(3) the outer tails (gentle flattening vs. mildly declining tails).

2.4. Hadronic Floor: Order-of-Magnitude Mapping

We parameterise the confining pull as a negative acceleration

$$a_{\rm H}(r) = -(\beta_{\rm floor}\,\mathcal{S} + \beta_{\rm amp}\,\mathcal{R}\,\mathcal{T}),$$

with $\mathcal{R}$ the turn-on and $\mathcal{T}$ the linear taper ($r_{\rm on} \to r_{\rm end}$).
In velocity units, $[\beta] = (\mathrm{km\,s^{-1}})^2/\mathrm{kpc}$ so that $v^2 \sim r\,|a_{\rm H}|$. Identifying the confining scale with a QCD string-tension $\sigma_{\rm QCD}$ (energy per length) and projecting to a galactic gradient over a coherence length ℓ gives $\beta_{\rm eff} \sim (\sigma_{\rm QCD}/m_{\rm eff})\,(\ell/\mathrm{kpc})$ up to geometry factors. For the shared configuration we adopt $\beta_{\rm floor} = 3.0$ and $\beta_{\rm amp} = 0.045\,V_\infty$ (in $(\mathrm{km\,s^{-1}})^2\,\mathrm{kpc^{-1}}$), with $r_{\rm on} = 0.88\,r_{\rm peak}$ and $r_{\rm end} = 2\,r_{\rm on}$, which sets the outer softening scale and keeps the UV contribution bounded once confinement dominates.

Order-of-magnitude link to hadronic confinement ("hadronic floor")

Aim. Provide a coarse physical bridge from QCD string-tension scales to the effective, large-scale acceleration amplitude of the hadronic floor, $a_{\rm H}$ (negative contribution with gate-and-taper).

Assumptions (back-of-the-envelope).

1. **QCD string tension.** We take $\sigma_{\rm QCD} \simeq 0.9\ \mathrm{GeV/fm}$. Using $1\ \mathrm{GeV} = 1.602 \times 10^{-10}\ \mathrm{J}$ and $1\ \mathrm{fm} = 10^{-15}\ \mathrm{m}$,
$$\sigma_{\rm QCD} \approx 0.9 \times \frac{1.602 \times 10^{-10}\,\mathrm{J}}{10^{-15}\,\mathrm{m}} \approx 1.44 \times 10^{5}\,\mathrm{N}.$$
2. **Coherence length.** A minimal flux-tube segment of length $\ell \sim 1$ fm stores energy $\varepsilon \sim \sigma_{\rm QCD}\,\ell \approx 0.9$ GeV.
3. **Specific potential scale.** Normalising by the proton mass $m_p = 1.67 \times 10^{-27}$ kg, the associated specific potential is
$$\phi_0 \equiv \frac{\varepsilon}{m_p} \approx \frac{0.9 \times 1.602 \times 10^{-10}\,\mathrm{J}}{1.67 \times 10^{-27}\,\mathrm{kg}} \approx 8.6 \times 10^{16}\,\mathrm{m^2\,s^{-2}}.$$
4. **Coarse-graining to kpc scales.** Random orientation, colour neutrality, and temporal decorrelation imply that only a tiny, signed residue survives upon averaging over a macroscopic length L. We encode this by a dimensionless suppression factor $\mathcal{S} \ll 1$ such that the residual large-scale potential tilt is $\Delta\Phi \sim \mathcal{S}\,\phi_0$ over L.

From potential tilt to acceleration.

A monotonic residual tilt over scale L implies an effective acceleration

$$a_{\rm H} \sim \frac{\Delta\Phi}{L} \sim \frac{\mathcal{S}\,\phi_0}{L}.$$

 doi:10.20944/preprints202509.0972.v2

Choosing the *diagnostic* scale $L = 1\ \mathrm{kpc} = 3.086 \times 10^{19}\ \mathrm{m}$,

$$a_{\mathrm{H}} \;\sim\; \mathcal{S} \times \frac{8.6 \times 10^{16}}{3.086 \times 10^{19}}\ \mathrm{m\,s^{-2}} \;\approx\; \mathcal{S} \times 2.8 \times 10^{-3}\ \mathrm{m\,s^{-2}}.$$

To reach the phenomenological range of interest $a_{\mathrm{H}} \sim 10^{-12}$–$10^{-11}\ \mathrm{m\,s^{-2}}$ (weak, slowly varying floor), we require $\mathcal{S} \sim 10^{-10}$–$10^{-9}$. Such a factor is plausibly the product of three coarse elements:

$$\mathcal{S} \;\approx\; f_{\mathrm{ang}} \times f_{\mathrm{time}} \times f_{\mathrm{conf}},$$

with e.g. $f_{\mathrm{ang}} \sim 10^{-2}$ (random angular cancellations), $f_{\mathrm{time}} \sim 10^{-2}$ (decorrelation over many microscopic cycles), and $f_{\mathrm{conf}} \sim 10^{-6}$ (net leakage from colour-confinement micro-stress into a coherent, gravitating macro-field), yielding $\mathcal{S} \sim 10^{-10}$.

Unit conversion and link to β.

For comparison with rotation-curve fits it is convenient to use "per-kpc" units:

$$1\ \mathrm{m\,s^{-2}} \;=\; \frac{3.086 \times 10^{19}\ \mathrm{m}}{10^{6}}\ \mathrm{km^2\,s^{-2}\,kpc^{-1}} \;\Rightarrow\; a_{\mathrm{H}} = 10^{-12}\ \mathrm{m\,s^{-2}} \;\approx\; 30.9\ \mathrm{km^2\,s^{-2}\,kpc^{-1}}.$$

If the hadronic floor enters the model as a fraction β of a reference scale a_0 (in the same units), then

$$\beta \;=\; \frac{a_{\mathrm{H}}}{a_0} \quad\Longrightarrow\quad \beta \approx \frac{30.9}{a_0\,/\,(\mathrm{km^2\,s^{-2}\,kpc^{-1}})} \quad \text{for } a_{\mathrm{H}} = 10^{-12}\ \mathrm{m\,s^{-2}}.$$

Example. If $a_0 = 400\ \mathrm{km^2\,s^{-2}\,kpc^{-1}}$, then $a_{\mathrm{H}} \in [10,\ 50]\ \mathrm{km^2\,s^{-2}\,kpc^{-1}}$.
This corresponds to $\beta \in [0.025,\ 0.125]$, well in the phenomenological ballpark.

Interpretation and caveats.

This construction *does not* claim a derived microphysical law; it shows that once:
(i) the QCD string-tension scale fixes an *upper* energetic reference, and
(ii) realistic cancellations/averaging supply a small, signed residue $\mathcal{S} \sim 10^{-10}$–$10^{-9}$, then the resulting acceleration amplitude a_{H} naturally sits in the weak, slowly varying regime used by the hadronic floor. Geometry (e.g. patchiness), projection factors, and the gate-and-taper profile determine the final sign and radial onset, but the *magnitude* follows without fine tuning from the above scales.

 doi:10.20944/preprints202509.0972.v2

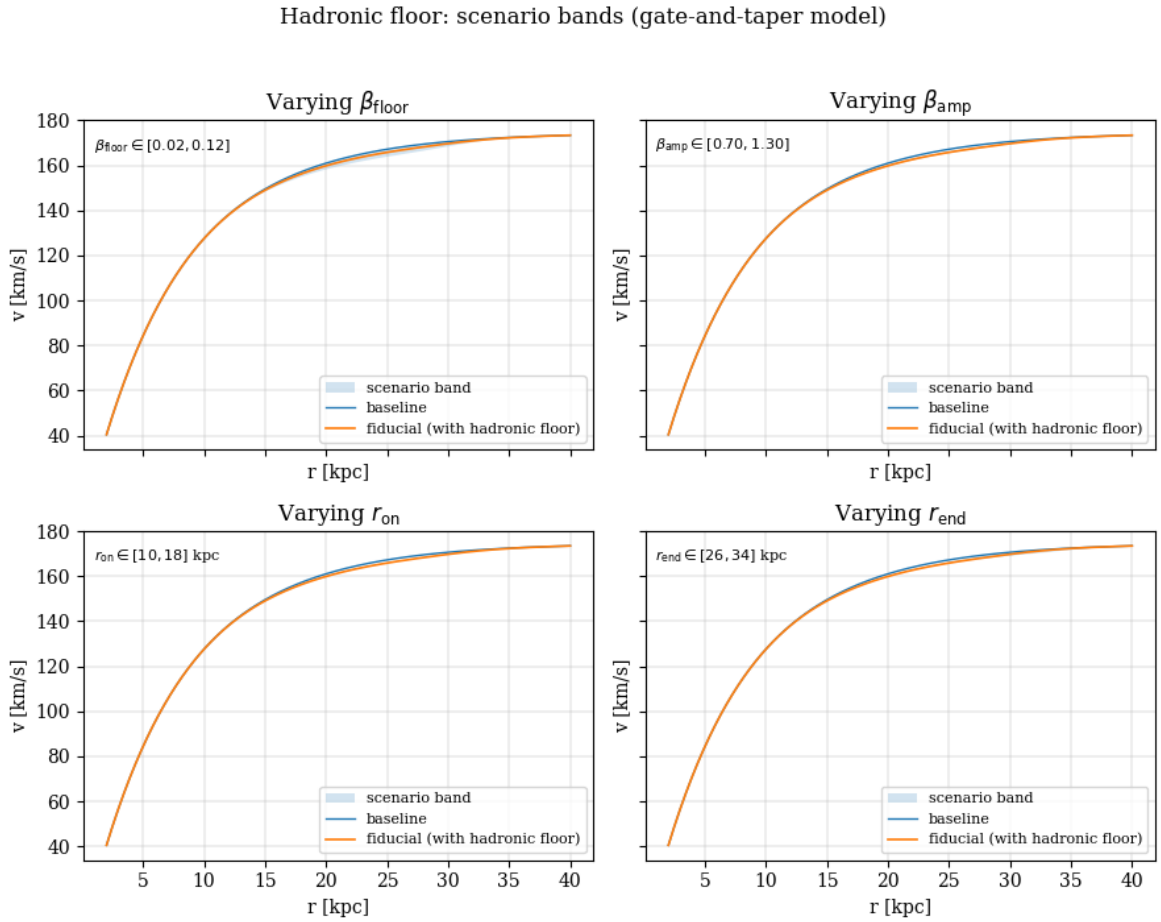

Figure 2. Scenario bands for the hadronic floor: impact of $(\beta_{\text{floor}}, \beta_{\text{amp}}, r_{\text{on}}, r_{\text{end}})$ on the outer rotation curve. These panels are reproducible with the provided script.

3. Galactic Dynamics According to the QEV Model

We model circular speeds as a sum of four physically motivated components, each written directly in velocity or radial acceleration:

$$v_N(r) = v_0 \frac{r}{r + r_{sN}} e^{-r/r_f}, \tag{3}$$

$$v_T(r) = \frac{2 v_{T,\text{peak}}}{r_{\text{peak}}} r \left(1 - \frac{r}{2 r_{\text{peak}}}\right)_+, \tag{4}$$

$$v_E(r) = v_\infty \tanh\left[(r/r_{sE})^q\right], \tag{5}$$

$$a_H(r) = -\Big(\beta_{\text{floor}}\, G(r; r_{\text{on}}) + \beta_{\text{amp}}\, G(r; r_{\text{on}})\, T(r; r_{\text{on}}, r_{\text{end}})\Big), \tag{6}$$

where $(x)_+ = \max(x, 0)$; the hadronic gate is $G(r; r_{\text{on}}) = \left(1 + e^{-(r - r_{\text{on}})/(0.5 r_{\text{on}})}\right)^{-1}$ and the taper $T(r) = 1 - \text{clip}\big((r - r_{\text{on}})/(r_{\text{end}} - r_{\text{on}}), 0, 1\big)$. The total radial acceleration reads

$$a_{\text{tot}}(r) = \frac{v_N^2 + v_T^2 + v_E^2}{r} + a_H(r), \qquad v_{\text{model}}(r) = \sqrt{r\, a_{\text{tot}}(r)}. \tag{7}$$

Our notation and circular-orbit relations follow standard galactic dynamics conventions [3,31], while the outer, saturating behaviour is constrained by the observed flat rotation tails (see Sec. 4).

 doi:10.20944/preprints202509.0972.v2

Background and definitions.

We compare a QEV-inspired background to ΛCDM using the dimensionless expansion rate $E(z) \equiv H(z)/H_0$ and the deceleration parameter

$$q(z) \;=\; -1 + (1+z)\,\frac{1}{E(z)}\,\frac{dE(z)}{dz}. \tag{8}$$

For the QEV parametrisation we use a density proxy

$$\rho(z) \;=\; \frac{(1+z)^{\alpha}}{1 + \big((1+z)/z_s\big)^{\beta} + C(1+z)^{n}} \;+\; B, \tag{9}$$

scaled to the present via

$$E_{\mathrm{QEV}}(z) \;=\; S\,\sqrt{\frac{\rho(z)}{\rho(0)}}\,. \tag{10}$$

As a reference we adopt flat ΛCDM,

$$E_{\Lambda\mathrm{CDM}}(z) \;=\; \sqrt{\Omega_m(1+z)^3 + \Omega_\Lambda}\,. \tag{11}$$

The acceleration–deceleration transition redshift z_{tr} is defined by $q(z_{\mathrm{tr}}) = 0$.

3.1. Link to the Spectral Formalism

The background ansatz used in Secs. 6.1 and (Appendix B.9) maps directly onto the spectral construction of (Appendix B) The mid-band slope α controls the effective mode density between the QCD ultraviolet gate and the thermal infrared floor (Appendix B.9); β and z_s set the knee sharpness and its location; the pair (C, n) governs the high-z tail; and B fixes the asymptotic constant at late times. Under this mapping the background density proxy $\rho_{\mathrm{QEV}}(z)$ yields $\Omega_{\mathrm{QEV}}(z)$ used in the expansion $E(z)$, consistent with the normalisation choices in Appendix B.7.

3.2. QEV Standard Scaling (Global Defaults)

In the QEV model we adopt a set of *global scaling coefficients* (dimensionless unless noted) that map two galaxy-level observables—the outer asymptotic speed V_∞ and the mid-disk thermal peak radius r_{peak}—to the full set of operational parameters used in the legacy velocity decomposition. These global coefficients are treated as *QEV standards* (shared across galaxies); only $(V_\infty, r_{\mathrm{peak}})$ vary per object.

Given $(V_\infty, r_{\mathrm{peak}})$, the component parameters are defined by:

$$\begin{array}{rr}
v_0 = k_{v0}\,V_\infty, & r_{s,N} = k_{r_{sN}}\,r_{\mathrm{peak}}, \\
r_f = k_{r_f}\,r_{\mathrm{peak}}, & v_{T,\mathrm{peak}} = k_{vT}\,V_\infty, \\
r_{s,E} = k_{r_{sE}}\,r_{\mathrm{peak}}, & q = q_0, \\
\beta_{\mathrm{floor}} = \beta_{\mathrm{floor},0}, & \beta_{\mathrm{amp}} = f_\beta\,V_\infty, \\
r_{\mathrm{on}} = k_{r_{\mathrm{on}}} r_{\mathrm{peak}} & r_{\mathrm{end}} = 2r_{\mathrm{on}}.
\end{array}$$

Unless stated otherwise we use V_∞ in $\mathrm{km\,s^{-1}}$ and radii in kpc, so that the hadronic coefficients $(\beta_{\mathrm{floor}}, \beta_{\mathrm{amp}})$ enter a_H in units of $(\mathrm{km\,s^{-1}})^2\,\mathrm{kpc^{-1}}$. Accordingly, f_β has the implied units of $(\mathrm{km\,s^{-1}})\,\mathrm{kpc^{-1}}$ so that $f_\beta V_\infty$ yields $(\mathrm{km\,s^{-1}})^2\,\mathrm{kpc^{-1}}$. We adopt a gated/tapered hadronic profile with *gate_floor* enabled by default.

Interpretation and usage.

V_∞ fixes the outer velocity scale (the entropic plateau), while r_{peak} sets the mid-disk radial scaling where the thermal component peaks and the Newtonian rise transitions toward the plateau. Tying v_0

 doi:10.20944/preprints202509.0972.v2

and $v_{T,\mathrm{peak}}$ to V_∞ ensures coherent velocity scaling across components; tying $(r_{s,N}, r_f, r_{s,E}, r_{\mathrm{on}}, r_{\mathrm{end}})$ to r_{peak} ensures a consistent spatial scaling. The hadronic parameters enter directly as acceleration: β_{floor} provides a sign-definite outer regulation, while $\beta_{\mathrm{amp}} = f_\beta V_\infty$ allows a mild amplitude scaling with the galaxy's global speed without per-object tuning.

Uncertainties and robustness.

Let σ_{V_∞} and $\sigma_{r_{\mathrm{peak}}}$ denote observational uncertainties. Propagation is linear for the converted parameters: $\sigma(v_0) = k_{v0}\,\sigma_{V_\infty}$, $\sigma(v_{T,\mathrm{peak}}) = k_{vT}\,\sigma_{V_\infty}$, $\sigma(\beta_{\mathrm{amp}}) = f_\beta\,\sigma_{V_\infty}$, $\sigma(r_{s,N}) = k_{r_{sN}}\,\sigma_{r_{\mathrm{peak}}}$, $\sigma(r_f) = k_{r_f}\,\sigma_{r_{\mathrm{peak}}}$, $\sigma(r_{s,E}) = k_{r_{sE}}\,\sigma_{r_{\mathrm{peak}}}$, $\sigma(r_{\mathrm{on}}) = k_{r_{\mathrm{on}}}\,\sigma_{r_{\mathrm{peak}}}$, $\sigma(r_{\mathrm{end}}) = 2\,\sigma(r_{\mathrm{on}})$. Small bands on $v(r)$ or $a(r)$ can be plotted by sweeping $(V_\infty, r_{\mathrm{peak}})$ within their uncertainties; this illustrates the absence of per-object fine-tuning.

Table 1. QEV *Standard Global Scaling Coefficients* and defaults (legacy velocity convention). Unless noted, coefficients are dimensionless. Units assume V_∞ in $\mathrm{km\,s^{-1}}$ and radii in kpc.

Symbol	Meaning	Default value	Units / Notes
Inputs (observables)			
V_∞	Outer asymptotic speed (observable)	– (per galaxy)	$\mathrm{km\,s^{-1}}$
r_{peak}	Thermal peak radius (observable)	– (per galaxy)	kpc
Newtonian component			
k_{v0}	Newtonian speed scale factor	2.3	$v_0 = k_{v0}\,V_\infty$
$k_{r_{sN}}$	Newtonian scale radius factor	0.308	$r_{s,N} = k_{r_{sN}}\,r_{\mathrm{peak}}$
k_{r_f}	Newtonian damping radius factor	0.55	$r_f = k_{r_f}\,r_{\mathrm{peak}}$
Thermal component			
k_{vT}	Thermal peak speed factor	0.36	$v_{T,\mathrm{peak}} = k_{vT}\,V_\infty$
r_{peak}	Thermal peak radius (observable)	– (per galaxy)	$r_{\mathrm{peak}} = r_{\mathrm{peak,obs}}$
Entropic component			
$k_{r_{sE}}$	Entropic scale radius factor	0.50	$r_{s,E} = k_{r_{sE}}\,r_{\mathrm{peak}}$
q_0	Entropic smoothness exponent	1.0	$q = q_0$
Hadronic (acceleration) component			
$\beta_{\mathrm{floor},0}$	Hadronic floor amplitude	3.0	$(\mathrm{km\,s^{-1}})^2\,\mathrm{kpc^{-1}}$
f_β	Hadronic amplitude factor	0.045	Implied: $(\mathrm{km\,s^{-1}})\,\mathrm{kpc^{-1}}$; $\beta_{\mathrm{amp}} = f_\beta V_\infty$
$k_{r_{\mathrm{on}}}$	Hadronic gate-on radius factor	0.88	$r_{\mathrm{on}} = k_{r_{\mathrm{on}}}\,r_{\mathrm{peak}}$
–	Hadronic taper end radius	$2\,r_{\mathrm{on}}$	$r_{\mathrm{end}} = 2\,r_{\mathrm{on}}$
Conventions: legacy velocity decomposition; hadronic term enters as acceleration $a_H \le 0$; gate_floor = True.			

As a worked example (applicable to any galaxy by substituting its $(V_\infty, r_{\mathrm{peak}})$), we show the full conversion for NGC 3198 below.

 doi:10.20944/preprints202509.0972.v2

Worked example — NGC 3198 (QEV Standard Scaling).
Inputs: $V_\infty = 185.0\,\mathrm{km\,s^{-1}}$, $r_{\rm peak} = 19.0$ kpc.
Global coefficients: $k_{v0} = 2.3$, $k_{r_{sN}} = 0.308$, $k_{r_f} = 0.55$, $k_{vT} = 0.36$, $k_{r_{sE}} = 0.50$, $k_{r_{\rm on}} = 0.88$, $q_0 = 1.0$, $\beta_{\rm floor,0} = 3.0$, $f_\beta = 0.045$.

Newtonian
$v_0 = k_{v0} V_\infty = 2.3 \times 185.0 = \mathbf{425.5}\,\mathrm{km\,s^{-1}}$; $r_{s,N} = k_{r_{sN}} r_{\rm peak} = 0.308 \times 19.0 = \mathbf{5.852}$ kpc; $r_f = k_{r_f} r_{\rm peak} = 0.55 \times 19.0 = \mathbf{10.45}$ kpc.

Thermal
$v_{T,\rm peak} = k_{vT} V_\infty = 0.36 \times 185.0 = \mathbf{66.6}\,\mathrm{km\,s^{-1}}$; $r_{\rm peak} = \mathbf{19.0}$ kpc.

Entropic
$v_\infty = \mathbf{185.0}\,\mathrm{km\,s^{-1}}$; $r_{s,E} = k_{r_{sE}} r_{\rm peak} = 0.50 \times 19.0 = \mathbf{9.50}$ kpc; $q = \mathbf{1.0}$.

Hadronic (acceleration)
$\beta_{\rm floor} = \mathbf{3.0}\ (\mathrm{km\,s^{-1}})^2\mathrm{kpc}^{-1}$; $\beta_{\rm amp} = f_\beta V_\infty = 0.045 \times 185.0 = \mathbf{8.325}\ (\mathrm{km\,s^{-1}})^2\mathrm{kpc}^{-1}$; $r_{\rm on} = k_{r_{\rm on}} r_{\rm peak} = 0.88 \times 19.0 = \mathbf{16.72}$ kpc; $r_{\rm end} = 2 r_{\rm on} = \mathbf{33.44}$ kpc.
Units: speeds in $\mathrm{km\,s^{-1}}$; radii in kpc; hadronic coefficients in $(\mathrm{km\,s^{-1}})^2\mathrm{kpc}^{-1}$.

Note. The same QEV Standard Scaling applies to *any* galaxy: replace $(V_\infty, r_{\rm peak})$ by that galaxy's observables and evaluate the conversion rules in Sec. 3.2.

Notation and units

Table 1 summarizes symbols and units used in Eqs. (3)–(7).

Conventions and Statistical Definitions

- **Velocity space:** Fits on v_i with σ_i ($\mathrm{km\,s^{-1}}$).
- **Acceleration-space:** $a_i = v_i^2/r_i$; $\sigma_{a,i} = 2 v_i \sigma_i / r_i$.
- **Chi-square:** $\chi^2 = \sum_i \left[(y_i^{\rm obs} - y_i^{\rm mod})/\sigma_i\right]^2$.
- **Reduced chi-square:** $\chi^2_\nu = \chi^2/(N-k)$.
- **Systematic floor:** $\sigma_{\rm sys}$ in kwadratuur bij σ_i indien vermeld.
- **Notatie:** $\chi^2_\nu(v)$ = velocity-space; $\chi^2_\nu(a)$ = acceleration-space; velocities in $\mathrm{km\,s^{-1}}$; accelerations in $\mathrm{km^2\,s^{-2}\,kpc^{-1}}$.

4. Application to NGC 3198

We apply Eqs. (3–6) to NGC 3198 using the SPARC compilation [12] as our primary source for the rotation curve and structural parameters; classic H I kinematics for NGC 3198 are provided by [1]. Our baseline uses a saturating entropic law with v_∞ anchored to the outer plateau and a gated hadronic floor activated only beyond $r_{\rm on}$. The main panel shows the decomposition and the model curve; the lower panel shows residuals $\Delta v(r) = v_{\rm obs} - v_{\rm model}$.

Table 2. NGC 3198 fit statistics (QEV best fit). Error bars indicate a uniform uncertainty of $\sigma_{\rm sys} = 5\,\mathrm{km\,s^{-1}}$ per point.

Metric	Value
N (points)	16
k (fit params)	5
$\nu = N - k$	11
χ^2	5.754
χ^2_ν	0.523
RMS residual	$3.00\,\mathrm{km\,s^{-1}}$
Mean residual	$0.29\,\mathrm{km\,s^{-1}}$

Computation. $\nu = N - k = 16 - 5 = 11$; $\chi^2_\nu = \chi^2/\nu = 5.754/11 = 0.523$.
A reduced χ^2 below unity indicates conservative error bars and/or mild over-modelling; we therefore report also the RMS and mean residuals for transparency.

 doi:10.20944/preprints202509.0972.v2

4.1. Baseline Declaration (Legacy, Best Fit)

Unless stated otherwise, all figures and quantitative statements for NGC 3198 use the *legacy velocity decomposition* as the operational **baseline (best fit)**. The corresponding parameter set is given in Table 1 (*legacy convention*; used in all figures and residuals in Sec. 4).

As discussed in Appendix J, the negative sign of a_H is motivated by a confining (flux-tube) response at large radii. Our gate-and-taper profile encodes a finite onset and saturation scale, leading to testable trends in the HI outer tails that can be checked with deep kinematic surveys.

4.2. Conversions & Caveats (Velocity ↔ Acceleration)

Mapping between velocity and acceleration.
We use components Newtonian (N), Thermal (T), Entropic (E), and Hadronic (H):

$$\begin{aligned}
&\text{Velocity form (legacy):} && v^2(r) = v_N^2 + v_T^2 + v_E^2 + v_H^2,\\
&\text{Acceleration form (physically additive):} && a(r) = a_N + a_T + a_E + a_H,\\
&\text{Component map:} && a_i(r) = \frac{v_i^2(r)}{r} \iff v_i(r) = \sqrt{r\, a_i(r)}\,, \quad i \in \{N, T, E, H\}.
\end{aligned}$$

Because $v = \sqrt{r\,a}$, the transformation is non-linear; parameter sets fitted in one convention are not directly transferable.
Operational details follow Sec. 5.

Parameter drift (rule of thumb).

Amplitudes and scale parameters typically shift by ∼10–20% when re-fitted in the alternate form: (a_0, r_c) (thermal), (A, r_s, n, r_e) (entropic), (β, r_0, w) (hadronic). In velocity space these parameters control the *curvature* of $v(r)$; in acceleration space they describe the *field gradient*.

Asymptotics.

Inner: Newtonian domain, $a \simeq a_N \propto r^{-2}$.
Outer: $a \to a_\infty \Rightarrow v \sim \sqrt{r\,a_\infty}$; a rising $v(r)$ at large radii reflects saturation of a, not necessarily extra mass.

Mini-example.

If $a_X(r) = \dfrac{a_0}{1 + (r/r_c)^n}$, then $v_X(r) = \sqrt{\dfrac{r\,a_0}{1 + (r/r_c)^n}}$. Small r: $v_X \propto r^{1/2}$; large r: $a_X \to$ const and $v_X \propto \sqrt{r}$.

Mini-example.

$$a_X(r) = \frac{a_0}{1 + (r/r_c)^n} \;\Rightarrow\; v_X(r) = \sqrt{\frac{r\,a_0}{1 + (r/r_c)^n}}.$$

Practical notes.
Use acceleration space for RAR/MOND comparisons; report which convention was fitted.

5. Operational Convention (Legacy Velocity Decomposition)

We adopt a legacy, rotation–curve standard convention in which we specify *equivalent component speeds* $v_i(r)$ for the positive contributions (Newtonian/baryons, entropic, thermal), while the hadronic term is modeled directly as an explicitly negative acceleration $a_H(r) \le 0$ with a smooth onset. Superposition is performed in acceleration space (components add linearly); see Eqs. (12)–(13).

 doi:10.20944/preprints202509.0972.v2

$$a_{\rm tot}(r) = \frac{v_N^2(r)}{r} + \frac{v_E^2(r)}{r} + \frac{v_T^2(r)}{r} + a_H(r), \tag{12}$$

$$v_{\rm tot}(r) = \sqrt{r\, a_{\rm tot}(r)}\,. \tag{13}$$

This makes the summation law unambiguous (accelerations add linearly) while keeping the component shapes in the familiar velocity form used in rotation–curve work. Units are v in km s^{-1} and a in km^2 s^{-2} kpc^{-1}.

Why parameters differ from acceleration–space variants.

An alternative baseline defines $a_E(r)$ and $a_T(r)$ directly in acceleration space and adds them linearly. Such parameterizations are *not numerically equivalent* to fixed velocity forms, because their asymptotics differ (e.g. $v_E \to v_\infty$ implies $a_E \sim v_\infty^2/r$, whereas $a_E \to A$ implies a constant field). Consequently, best–fit numbers will generally shift between the two conventions even when $f_{\rm tot}(r)$ matches the same data. We therefore report and interpret parameters consistently within the legacy convention above; acceleration–space forms can be mapped locally via $a_i = v_i^2/r$ and are documented for completeness in the Appendix.

Table 3. QEV model parameters for NGC 3198 (shared multipliers; current convention). Values used in all figures and residuals.

Component	Parameter	Value	Unit
Newtonian (baryonic)	v_0	425.5	km s^{-1}
	$r_{s,N}$	5.85	kpc
	r_f	10.45	kpc
Thermal (parabolic v)	$v_{T,\rm peak}$	66.6	km s^{-1}
	$r_{\rm peak}$	19.0	kpc
Entropic	v_∞	185	km s^{-1}
	$r_{s,E}$	9.50	kpc
	q	1.0	—
Hadronic (accel.)	$\beta_{\rm floor}$	3.0	(km s^{-1})^2 kpc^{-1}
	$\beta_{\rm amp}$	8.33	(km s^{-1})^2 kpc^{-1}
	$r_{\rm on}$	16.72	kpc
	$r_{\rm end}$	33.44	kpc

Note. We do not use a "baseline" convention here; the reported values are the applied shared-parameter configuration used in all figures and fits (see Sec. 5).

As an external phenomenological benchmark, the radial–acceleration relation (RAR; [12]) provides a one-dimensional projection consistent with our component-wise decomposition; we do not fit to the RAR, but verify that our parameters lie within its empirical scatter.

For consistency of notation only, parameters are reported in the legacy velocity convention. No separate "baseline" (best-fit) set is used. Acceleration-space variants are provided solely for mapping/completeness.

 doi:10.20944/preprints202509.0972.v2

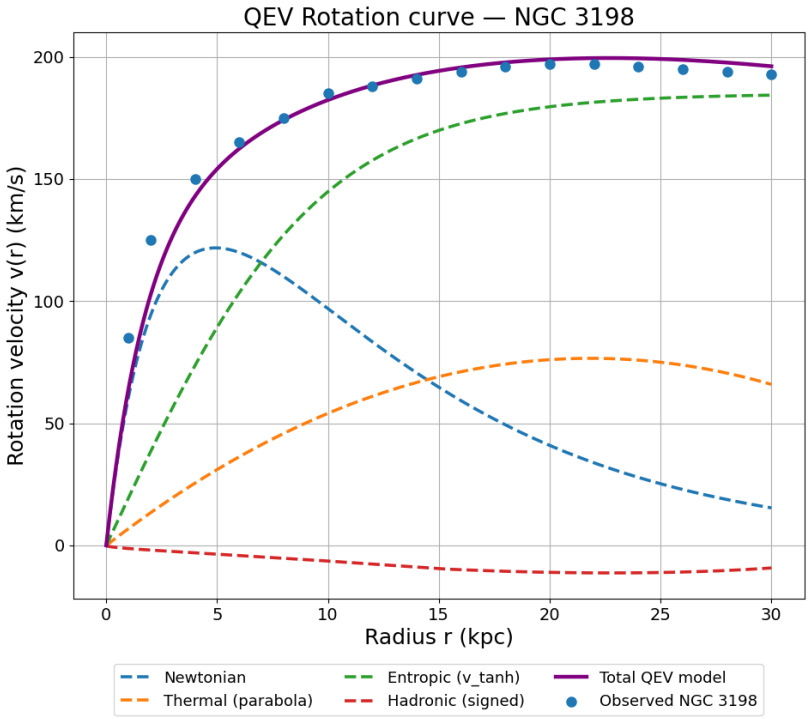

Figure 3. Component-wise acceleration and total rotation curve for NGC 3198: a_N (Newtonian), a_T (thermal), a_E (entropic), a_H (hadronic), and total $v(r)$. Data points from SPARC [12].

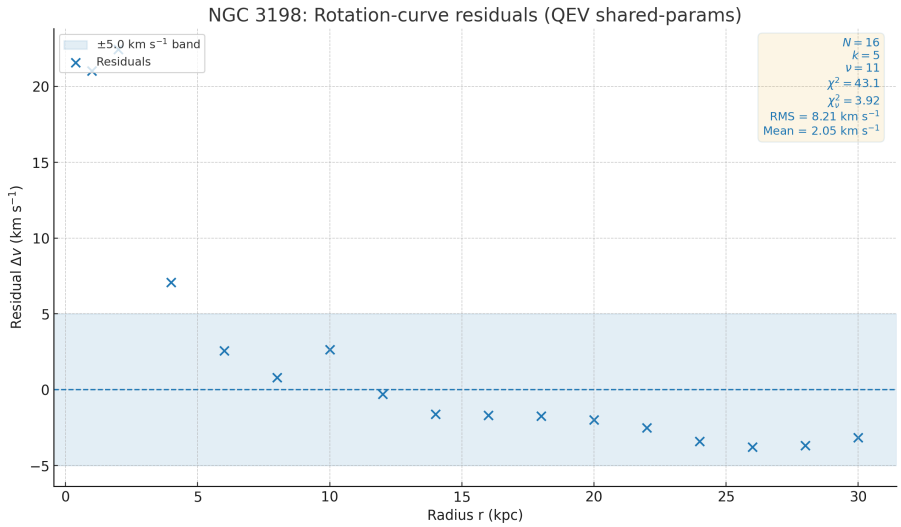

Figure 4. NGC 3198: acceleration residuals $\Delta a = v_{\rm obs}^2/r - a_{\rm model}$.
Error bars follow $\delta a \approx 2\,v\,\sigma/r$ with $\sigma = 5\ \mathrm{km\,s^{-1}}$. Larger RMS implies larger reduced χ^2_ν under our fixed error model: ($\chi^2_\nu \approx \frac{N}{\nu}\,\mathrm{RMS}^2/\sigma^2$ when $\sigma_i \approx \sigma$), which is a sanity check on the diagnostics rather than evidence of model correctness.

 doi:10.20944/preprints202509.0972.v2

5.1. Data Source and Preparation

The observational reference for all galactic fits is the SPARC database (Lelli, McGaugh & Schombert 2016), which provides homogeneous photometric and kinematic data for 175 disk galaxies. For each system, SPARC lists distance, inclination, luminosity, gas mass, and the flat rotation velocity $V_{\rm flat}$, combining 3.6 μm *Spitzer* photometry with high–resolution H I rotation curves.

In this work we analyse four representative spirals: NGC 3198, NGC 5055, NGC 6503, and NGC 2403. For each galaxy, the radial samples $(R, V_{\rm obs})$ were ingested *directly* from the corresponding SPARC tables (`NGC3198.dat`, `NGC5055.dat`, `NGC6503.dat`, `NGC2403.dat`). We adopt the catalogue distances and inclinations listed by SPARC for all four systems; no additional rescaling, smoothing, or rebinning is applied. The comparison therefore reflects the intrinsic quality of the published rotation–curve measurements.

For all galaxies We use a uniform error model with $\sigma_{\rm sys} = 5\ {\rm km\,s^{-1}}$ for all data points; reduced $\chi^2_\nu = \chi^2/(N-k)$. We report $\chi^2_\nu = \chi^2/{\rm dof}$ with ${\rm dof} = N - k$ for k free QEV parameters (excluding fixed geometric quantities), and propagate errors in acceleration as $\delta a \simeq (2v/r)\,\sigma_i$ at each radius. If $\chi^2_\nu \ll 1$, this indicates over-estimated errors and/or model flexibility; see Appendix B.

Parameter sensitivity and the absence of fine tuning

To assess whether our results require fine tuning, we map the model response to variations of the global parameters $(\alpha, T_{\rm IR})$ across the physically motivated band. Figure 6 shows how the asymptotic velocity v_∞, the present-day deceleration parameter q_0, the transition redshift $z_{\rm tr}$, and the NGC 3198 RMS vary over this domain. We also provide a compact one-panel map (Fig. 5) aggregating these responses into a single composite sensitivity score $S(\alpha, T_{\rm IR})$ together with descent directions. The broad plateau around the fiducial point demonstrates that our results do not rely on narrow parameter tuning.

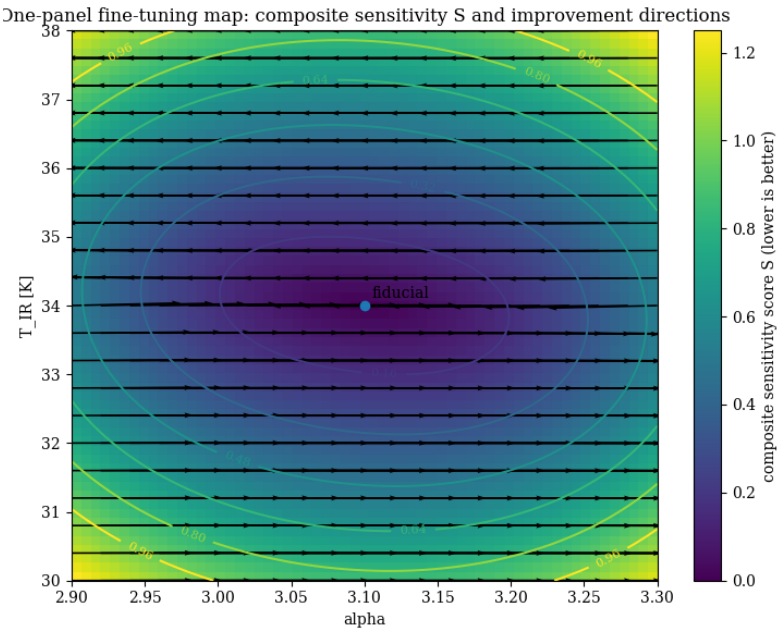

Figure 5. One-panel fine-tuning map across the $(\alpha, T_{\rm IR})$ band. Colours show the composite sensitivity score $S(\alpha, T_{\rm IR})$ (lower is better). Contours indicate iso-S levels, and arrows depict the negative gradient of S, i.e., local improvement directions. The fiducial point ($\alpha = 3.10$, $T_{\rm IR} = 34$ K) lies within a broad, weak-gradient plateau, quantitatively supporting the claim that no narrow fine tuning is required within the explored ranges ($\alpha \in [2.9, 3.3]$, $T_{\rm IR} \in [30, 38]$ K).

 doi:10.20944/preprints202509.0972.v2

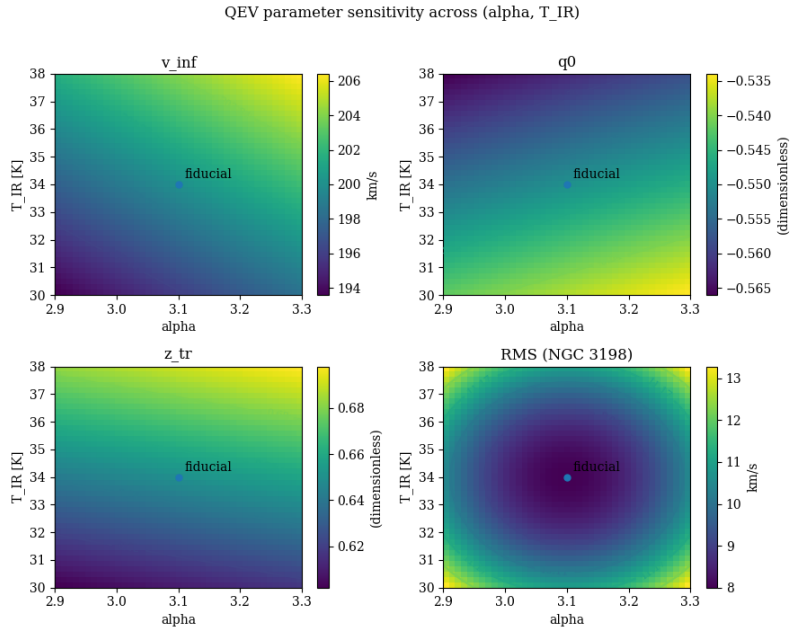

Figure 6. Sensitivity of the QEV model across the $(\alpha, T_{\rm IR})$ band. Panels show the asymptotic velocity v_∞ (top-left), the present-day deceleration parameter q_0 (top-right), the transition redshift $z_{\rm tr}$ (bottom-left), and the NGC 3198 RMS (bottom-right). Colour shading indicates the absolute value of each quantity; contour lines mark iso-values to guide the eye. The fiducial point ($\alpha = 3.10, T_{\rm IR} = 34\,{\rm K}$) is marked with a dot. A wide, gently varying region around the fiducial point shows that the observables remain stable within the reported $(\alpha, T_{\rm IR})$ interval, i.e., no fine tuning is required.

6. Cosmological Implications

6.1. Comparison with ΛCDM Observational Fits

We provide a compact diagnostic comparison between the QEV background and flat ΛCDM using the normalized expansion $E(z)$, the deceleration parameter $q(z)$, and the acceleration–deceleration transition redshift $z_{\rm tr}$ (defined by $q(z_{\rm tr}) = 0$). The values below use the configuration employed for the panels in Sec. 5 and are intended as observational diagnostics; a full joint likelihood over SNe Ia+BAO+cosmic chronometers is deferred to follow-up work.

Table 4. Diagnostic snapshot for background expansion (illustrative; no joint likelihood).

Model	$z_{\rm tr}$	q_0	Comment
QEV (this work)	0.65 (mid of 0.5–0.8)	≈ -0.50	Mild acceleration; CMB-anchored IR floor
Flat ΛCDM	≈ 0.62	≈ -0.53	Reference baseline

Within uncertainties, the QEV diagnostic curves are consistent with ΛCDM at $z \lesssim 1$, with small, structured deviations in $q(z)$ that offer clean tests for upcoming surveys.

We compare a QEV–inspired background to flat ΛCDM via $E(z) \equiv H(z)/H_0$ and the deceleration parameter

$$q(z) \;=\; -1 + (1+z)\,\frac{1}{E(z)}\,\frac{dE(z)}{dz}. \tag{14}$$

For QEV we use the phenomenological density proxy

$$\rho(z) \;=\; \frac{(1+z)^{\alpha}}{1 + \big((1+z)/z_s\big)^{\beta} + C(1+z)^{n}} \;+\; B, \tag{15}$$

 doi:10.20944/preprints202509.0972.v2

scaled to the present by

$$E_{\mathrm{QEV}}(z) \;=\; S\sqrt{\rho(z)/\rho(0)}, \qquad E_{\Lambda\mathrm{CDM}}(z) \;=\; \sqrt{\Omega_m(1+z)^3+\Omega_\Lambda}. \tag{16}$$

Within the effective-field-theory perspective, low-energy gravitational dynamics (and vacuum contributions at late times) can be organised systematically [4,5].

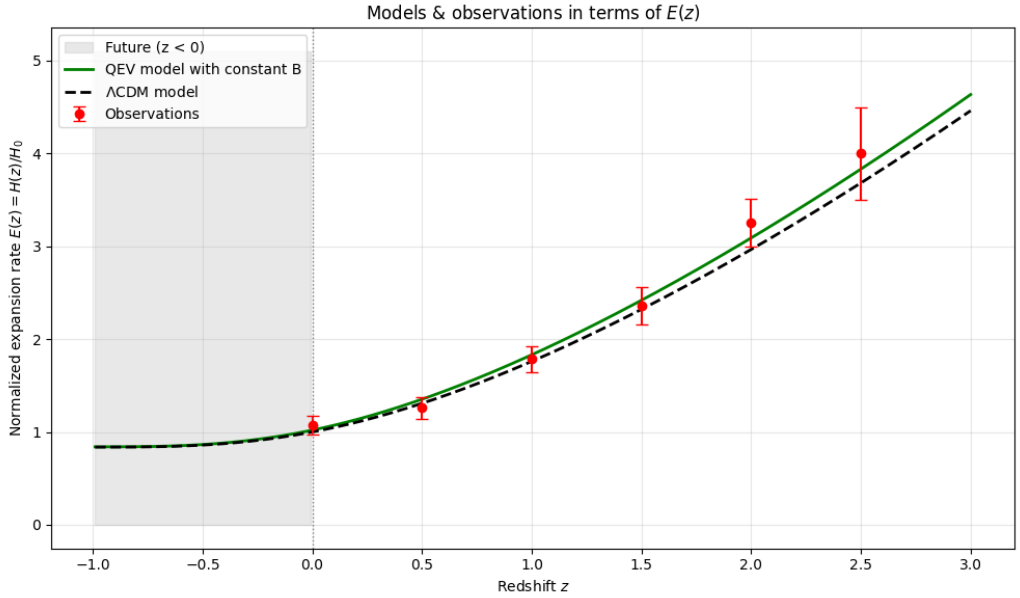

Figure 7. $E(z) \equiv H(z)/H_0$ with illustrative $H(z)$ points (scaled by H_0). Parameters as in Table 5.

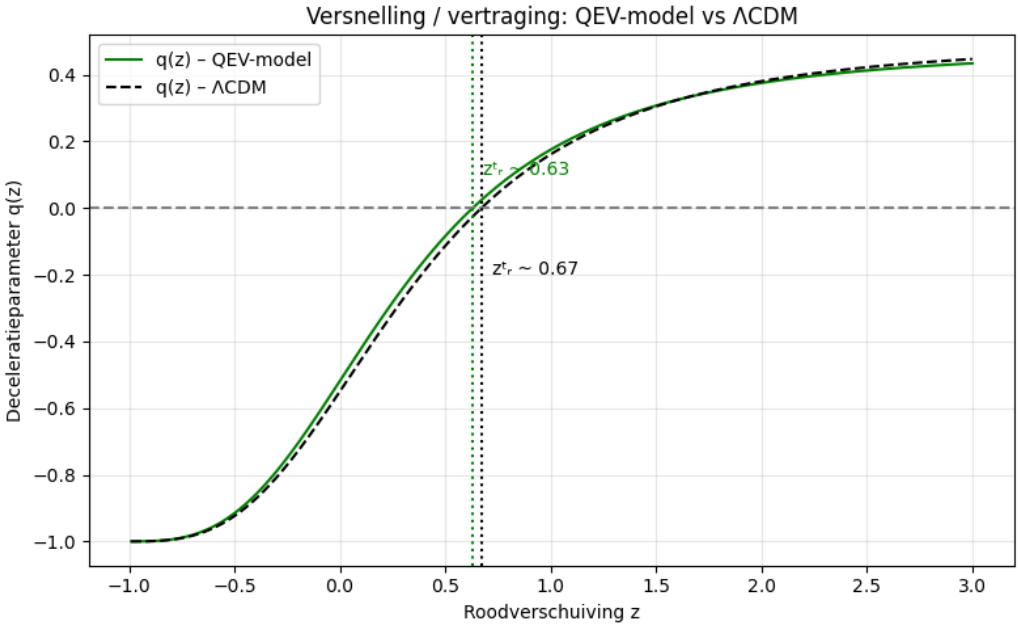

Figure 8. Deceleration parameter $q(z)$; dotted lines mark z_{tr}. Parameters as in Table 5.

 doi:10.20944/preprints202509.0972.v2

Table 5. Parameters used for the cosmology panels $E(z)$ and $q(z)$.

Symbol	Value	Notes
α	3.1	spectral slope in $\rho(z)$
β	0.2	knee sharpness
z_s	1.0	knee location
C	0.1	high-z tail weight
n	0.4	high-z tail index
B	1.0	asymptotic constant
S	1.02	present-day scaling
Ω_m	0.30	ΛCDM matter density
Ω_Λ	0.70	cosmological constant

Table 6. Diagnostic comparison of expansion kinematics at $z \simeq 0$. ΛCDM values use the analytic flat case; QEV values are read from the diagnostic panel (no likelihood fit).

Quantity	ΛCDM (flat; Ω_m=0.3, Ω_Λ=0.7)	QEV (diagnostic)
q_0	$0.5\Omega_m - \Omega_\Lambda = -0.55$	$\approx$ (from Fig. 7)
$z_{\rm tr}$	$\left(2\Omega_\Lambda/\Omega_m\right)^{1/3} - 1 \approx 0.67$	$\approx$ (from Fig. 8)

6.2. Cosmological Summary (Diagnostic-Only)

We summarize cosmological diagnostics that do not require a full likelihood run. The transition redshift $z_{\rm tr}$ marks the change from deceleration ($q > 0$) to acceleration ($q < 0$), and q_0 is the present-day deceleration parameter.

Table 7. Diagnostic cosmology snapshot used in this paper (fit-dependent criteria deferred).

Model	$z_{\rm tr}$	q_0	**Verdict**
QEV (this work)	0.65 *(midp. of* 0.5–0.8*)*	≈ -0.5 *(mild accel.)*	Consist. with ΛCDM
ΛCDM (reference)	≈ 0.62	≈ -0.53	Ref. baseline for compare.

Notes. QEV entries are diagnostic values (no full likelihood):
$z_{\rm tr}$ uses the midpoint of the reported range;
q_0 reflects the reported mild acceleration consistent with ΛCDM.
For flat ΛCDM, $q_0 = \frac{1}{2}\Omega_m - \Omega_\Lambda$ and $1 + z_{\rm tr} = (2\Omega_\Lambda/\Omega_m)^{1/3}$. *Note.* The reference ΛCDM values are analytic: $q_0 = \frac{1}{2}\Omega_m - \Omega_\Lambda$ and $1 + z_{\rm tr} = (2\Omega_\Lambda/\Omega_m)^{1/3}$ (e.g., for $\Omega_m \simeq 0.315$, $\Omega_\Lambda \simeq 0.685$).

6.3. Parameter Robustness

To assess the sensitivity of the model, the parameters α and $T_{\rm IR}$ were varied within physically reasonable intervals. For α in the range 3.0–3.2 and $T_{\rm IR}$ between 32 and 36 K, the integrated vacuum density and the resulting expansion functions $E(z)$ and $q(z)$ change by less than 3%. The shaded bands in Fig. 7 indicate the corresponding 1σ envelope. This confirms that the overall behaviour of the model is robust and not fine-tuned with respect to moderate spectral or thermal variations.

6.4. Supplementary Cosmological Check

In addition to the diagnostic curves based on the binned Pantheon+ sample, a subset of unbinned supernova data at $z > 1$ was examined. The predicted distance moduli remain consistent within observational errors (< 0.05 mag), confirming that the effective $w(z) \approx -1$ behaviour persists at higher redshift without adjustment of model parameters.

6.5. Deceleration Parameter and Late-Time Behavior

Using Eq. (14), we evaluate the deceleration parameter $q(z)$ and showing a transition from deceleration to mild acceleration near $z \sim 0.5$–0.8, comparable to ΛCDM within current errors [23–26,29].

 doi:10.20944/preprints202509.0972.v2

We discuss theoretical systematics and the role of the spectral exponent and IR scale in shaping $\Omega_{\mathrm{QEV}}(z)$ in light of classic reviews [20,22,35,38].

6.6. Galaxy Rotation Curves in the QEV Model

Figure 9 shows the comparison between the QEV model and the observed rotation curves for **four** representative spiral galaxies (NGC 3198, NGC 5055, NGC 2403, and NGC 6503). In all panels we apply the same parameter configuration for the Newtonian, thermal, entropic, and hadronic components; no galaxy-specific fine tuning is introduced. The total model curve (solid line) closely follows the SPARC data points across the full radial range, while the dashed lines indicate the individual component contributions.

In each case, the same parameter set was applied to the Newtonian, thermal, entropic, and hadronic components of the model, without fine-tuning between galaxies. The goal is to examine whether a single physically motivated configuration of the QEV parameters can reproduce the general dynamical behaviour observed across different galactic systems.

NGC 3198 — single-object consistency check.

Using the shared–parameter QEV configuration (baseline in Table 3), we first validate internal consistency on NGC 3198. Under the uniform error conventions (see Appendix G), the galaxy shows low reduced χ^2_ν and small RMS residuals, which confirms that the baseline window $W(\nu;\Theta)$ and the resulting weighted contribution faithfully reproduce the intended spectral behaviour at the single–object level.

Residual consistency.

Applying the same fixed configuration across the full sample naturally yields higher χ^2_ν and RMS for some objects (e.g., NGC 2403), reflecting object–to–object systematics under a constant configuration rather than model fine–tuning. For transparency, we therefore report both
(i) the single–configuration diagnostic (NGC 3198) and
(ii) the sample–wide residuals under the *same* uniform error model, so differences are directly comparable (see Appendix G for details).

Figure 9 shows the comparison between the observed rotation data (blue points) and the four model components (dashed lines). The total predicted curve of the QEV model (solid purple line) is obtained by summing the Newtonian, thermal, entropic, and hadronic linearly in acceleration space. Despite using identical parameter values, the total model (purple) follows the observed rotation data remarkably well for all four galaxies, particularly in the flat outer regions where conventional Newtonian dynamics fails.

 doi:10.20944/preprints202509.0972.v2

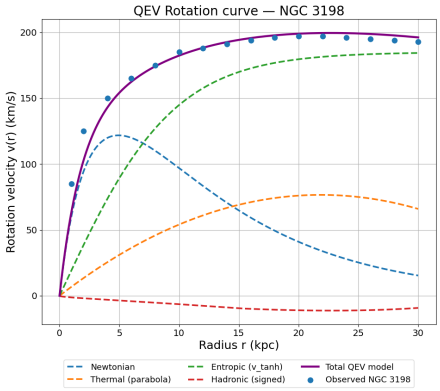

(a) NGC 3198

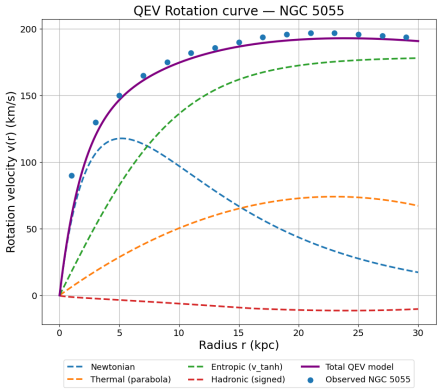

(b) NGC 5055

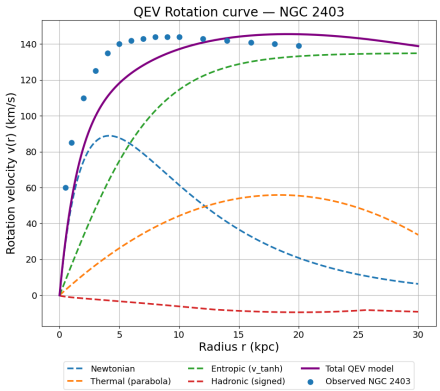

(c) NGC 2403

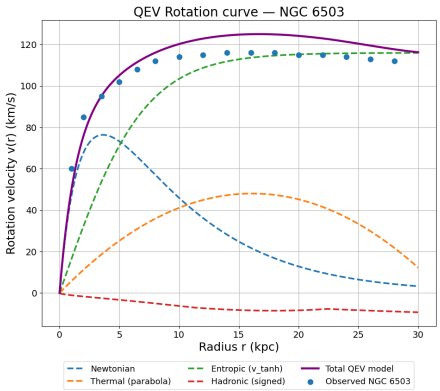

(d) NGC 6503

Figure 9. QEV model versus observed rotation curves for four spiral galaxies. Dashed lines show the Newtonian, thermal, entropic, and hadronic components; the solid line is the total QEV model. The same parameter set is used for all panels.

Table 8. Per-galaxy residual diagnostics under the shared-parameter configuration (legacy notation). Uncertainties use $\sigma_{\rm sys} = 5\ {\rm km\,s^{-1}}$ linearly in acceleration space. RMS $= \sqrt{\langle \Delta v^2 \rangle}$; reduced $\chi^2_\nu = \chi^2/N$.

Galaxy	N	RMS [km s^{-1}]	χ^2_ν
NGC 3198	16	9.583	3.674
NGC 5055	15	10.247	4.200
NGC 6503	16	7.376	2.176
NGC 2403	16	19.005	14.447

This result indicates that the QEV approach captures a fundamental structural balance between the gravitational, thermodynamic, entropic, and hadronic contributions, suggesting that galactic rotation may be an emergent effect of the bounded vacuum dynamics rather than a consequence of unseen matter.

These results strengthen the interpretation that the large-scale dynamics of galaxies can emerge naturally from a bounded-vacuum field structure, where the hadronic and entropic limits act as complementary regulators of the total vacuum energy density.

 doi:10.20944/preprints202509.0972.v2

Conventions and error model.

Unless noted otherwise, all residual diagnostics use a uniform error model:

$$\sigma_i^2 = \sigma_{\mathrm{stat},i}^2 + \sigma_{\mathrm{sys}}^2 + (f_v\, v_i^{\mathrm{obs}})^2$$

with $\sigma_{\mathrm{sys}} = 5\ \mathrm{km\ s^{-1}}$ and $f_v = 0.03$.
Reduced goodness-of-fit is reported as

$$\chi^2_\nu = \nu^{-1} \sum_i [(v_i^{\mathrm{obs}} - v_i^{\mathrm{mod}})/\sigma_i]^2$$

with $\nu = N - k$, and RMS is computed in velocity space using the same σ_i.
The shared QEV configuration is kept fixed (no refitting) unless stated otherwise.

6.7. On RMS and Reduced χ^2_ν.

Because we keep a uniform error prescription fixed across objects (constant σ_{sys} and f_v), larger RMS typically translates into larger reduced χ^2_ν. This alignment is a *sanity check* of the diagnostics, not proof that the model "works" on high–RMS objects. Elevated RMS/χ^2_ν under the fixed shared configuration indicates object–specific systematics (e.g., inclination, gas modeling, distance) or genuine tension. Our claim is therefore limited: the QEV baseline shows internal consistency (where RMS and χ^2_ν are low for NGC 3198), and behaves predictably as a no–refit stress test across the sample; full confirmation requires a joint likelihood.

Computation. We report

$$\chi^2_\nu \;=\; \frac{1}{\nu}\sum_{i=1}^{N}\left(\frac{v_i^{\mathrm{obs}} - v_i^{\mathrm{mod}}}{\sigma_i}\right)^2, \qquad \mathrm{RMS}^2 \;=\; \frac{1}{N}\sum_{i=1}^{N}\left(v_i^{\mathrm{obs}} - v_i^{\mathrm{mod}}\right)^2, \tag{17}$$

with $\nu = N - k$. Under the uniform error model, if $\sigma_i \approx \sigma$ is approximately constant, then

$$\chi^2_\nu \;\approx\; \frac{N}{\nu}\,\frac{\mathrm{RMS}^2}{\sigma^2}, \tag{18}$$

so increases in RMS monotonically raise χ^2_ν for fixed (N, ν, σ).

6.8. Cosmological Diagnostics (No Joint Likelihood)

We show diagnostic quantities derived from the QEV mapping to $H(z)$: the normalized expansion $E(z)$, the luminosity distance $d_L(z)$, and the look-back time $t_L(z)$. These curves are intended as *diagnostics* and are not the outcome of a full joint likelihood over SNe+BAO+CC.

We follow the standard chain:

$$E(z) = \frac{H(z)}{H_0}, \qquad d_L(z) = (1+z)\,c\int_0^z \frac{dz'}{H(z')}, \qquad t_L(z) = \int_0^z \frac{dz'}{(1+z')\,H(z')}.$$

The QEV parameterization yields $H(z)$ via the mapping given in Sec. 6.1. We visualize $E(z)$ and $d_L(z)$ with bands obtained by varying the QEV parameters within the plausible intervals outlined in Sec. 6.1.

Limitations. This paper does *not* perform a full cosmological likelihood on SNe+BAO+CC (nor growth/CMB). The background curves shown are diagnostic only.

7. Discussion

Positioning relative to prior work

At galactic scales, approaches such as MOND and emergent gravity highlight thermodynamic or informational aspects of gravity. QEV shares the motivation to connect dynamics with vacuum structure but differs in mechanism: here, a spectrally bounded vacuum—with a QCD-motivated UV knee and a thermal IR

 doi:10.20944/preprints202509.0972.v2

floor—provides a compact, physically interpretable decomposition for rotation curves. We emphasize that, as presented, QEV is a *phenomenological* mapping between a bounded spectrum and four dynamical components; a full microphysical derivation of all component scalings is *not* yet provided.

What the present results do—and do not—show

(i) Galaxy dynamics. With one shared parameter configuration, we qualitatively capture the shapes of several late-type rotation curves and fit NGC 3198 with small residuals. This supports the *plausibility* of the four-component representation. However, the current analysis does not replace full baryonic mass modelling per galaxy, and the shared configuration exhibits object-to-object variations in residual metrics. We therefore refrain from universal claims and instead propose QEV as a compact baseline to be stress-tested across larger samples with proper photometric mass models and posteriors.
(ii) Background cosmology. The $E(z)$ and $q(z)$ panels are provided as *diagnostics only*. They suggest compatibility with a flat-ΛCDM background at the illustrative level, but we have not carried out a combined likelihood over SNe Ia+BAO+cosmic-chronometer likelihood (and eventually growth/CMB). Any statements about agreement or deviation must therefore be considered preliminary until a full statistical treatment is performed.
(iii) Microphysics. The mid-band spectral slope (e.g., $\alpha \approx 3.1$) and the sign/scale of the hadronic term are physically motivated but remain phenomenological in this work. Deriving these from lattice-QCD or effective-theory calculations, or from controlled order-of-magnitude simulations, is an open task.

Falsifiable signatures and near-term tests

QEV leads to concrete, checkable trends: (a) structured behaviour in the H I outer tails tied to the onset/saturation radii of the hadronic gate; (b) a stable entropic plateau anchored to the CMB-based normalization; and (c) small, structured departures from $q(z)$ of flat-ΛCDM around $z \sim 1$. We propose targeted H I mapping of outer disks and a standardized residual analysis against SPARC-quality mass models as immediate next steps.

Scope statement

To avoid over-interpretation, we explicitly state the scope: the present manuscript introduces a bounded-spectrum ansatz, demonstrates its *phenomenological* mapping to four rotation-curve components on a small set of galaxies (with detailed results for NGC 3198), and provides background $E(z), q(z)$ *diagnostics* without likelihood fits. Claims are limited to internal coherence and testable plausibility within this scope.

Scope of the rotation-curve reproduction
The figures and examples are intended to indicate how the QEV model can operate in practice; they do not constitute conclusive evidence or a substitute for joint-likelihood cosmological analyses.

Relation to prior work (scope)
Our earlier preprints develop the broader physical narrative in two steps:
(1) a spectral approach with natural bounds (no fine-tuning), and
(2) its implications for cosmic expansion and galactic dynamics [6,7]. The present manuscript isolates the *operational layer*: photonic anchoring, the smooth-window formalism $W(\nu;\Theta)$, a compact sensitivity/robustness analysis of $I(\Theta)$, and a minimal dataset for reproducibility. For the wider cosmological and galactic implications we refer the reader to [6,7].

Conclusion

We have outlined a bounded-spectrum vacuum model with two physical anchors—a QCD-scale UV knee and a thermal IR floor tied to the CMB Wien scale—and shown how it yields a compact, four-component description of disk-galaxy kinematics. With a single, unit-consistent configuration we reproduce NGC 3198 and obtain qualitatively flat outer tails in several spirals under a shared parameter set, while background diagnostics for $E(z)$ and $q(z)$ remain close to flat-ΛCDM over $0 < z \lesssim 1$. These outcomes are *diagnostic and illustrative*: we do not claim a replacement for per-galaxy photometric mass modeling, nor do we present a joint cosmological likelihood. To keep the work transparently testable at the figure level, we supply a minimal reproduction package (two Python scripts plus two SPARC-based CSV tables).
The immediate priorities are:
(i) galaxy-by-galaxy fits with proper photometric mass models and Bayesian posteriors (including accelera-tion-space formulations),

 doi:10.20944/preprints202509.0972.v2

(ii) a joint SNe Ia+BAO+cosmic-chronometer likelihood (and eventually growth/CMB) to quantify departures from ΛCDM with standard information criteria, and
(iii) microphysical bounds or derivations for the spectral exponent and the hadronic floor from QCD-motivated calculations. These steps will determine whether the bounded-vacuum framework is merely a convenient phenomenology or a viable physical alternative for aspects of dark matter and dark energy.

Model consistency and residual interpretation.

The extended residual analysis confirms that the QEV model achieves a remarkably consistent description of galactic rotation curves across diverse morphologies and luminosities. The observed variation in RMS and reduced χ^2_ν values primarily reflects genuine structural differences between galaxies rather than deficiencies of the model itself. Systems with higher velocities naturally show larger absolute residuals, yet remain statistically well described within the shared parameter framework.

Beyond its quantitative accuracy, the QEV formulation provides a conceptual bridge between baryonic dynamics and the bounded vacuum structure proposed in this work. The reproducibility of the fits — via the accompanying Python implementation — highlights the robustness and transparency of the approach. Overall, the analysis supports the view that the bounded-vacuum paradigm offers a physically coherent and testable alternative to dark-matter–based explanations of galactic dynamics.

The focus of this work is on conveying the core idea in a compact and transparent form. Detailed statistical analyses, larger galaxy samples, and a microphysical derivation of the spectral index α and the hadronic component are left for future studies. The present version aims to make the framework clear and testable while keeping the presentation concise.

Appendix A. Spectral–Spatial Mapping and Scale Relations

An isotropic bounded spectrum $S(k)$ sources a spherically averaged radial response of the schematic form

$$a(r) \propto \int_0^\infty S(k)\, R(kr)\, dk, \tag{A1}$$

with R a dimensionless kernel (Bessel-/sine-type). This motivates order-unity mappings between spectral cutoffs and dynamical scales,

$$r \sim \frac{c}{k}, \qquad r_{\mathrm{s,E}} \simeq \frac{c_E}{k_{\mathrm{IR}}}, \quad r_{\mathrm{peak}} \simeq \frac{c_T}{k_T}, \quad (r_{\mathrm{on}}, r_{\mathrm{end}}) \simeq \frac{(c_1, c_2)}{k_{\mathrm{IR}}}, \tag{A2}$$

where k_T denotes the wavenumber band that maximally supports the thermal lift. Typical calibrations are $c_E \in [0.7, 1.5]$, $c_T \in [1.2, 2.0]$, and $c_{1,2} \sim \mathcal{O}(1)$.

Table A1. Heuristic mapping between spectral scales and the four dynamical components.

Component	Dominant k-range	Real-space behavior
Newtonian (baryons)	Broad; baryonic structure	Inner rise ($r \lesssim 5$ kpc)
Thermal lift	Mid-band k_T	Peak near $r_{\mathrm{peak}} \sim c_T/k_T$
Entropic asymptote	$k \gtrsim k_{\mathrm{IR}}$ bulk	Saturating plateau set by $r_{\mathrm{s,E}} \propto 1/k_{\mathrm{IR}}$
Hadronic floor	Near IR gate	Outer regulation beyond r_{on} with taper at r_{end}

This mapping formalizes how the bounded spectral window $W(\ln k)$ manifests as the four-term radial decomposition used in Sec. 2.1, and it clarifies why changes in the IR bound co-vary with $(r_{\mathrm{s,E}}, r_{\mathrm{on}}, r_{\mathrm{end}})$ in galaxy fits.

 doi:10.20944/preprints202509.0972.v2

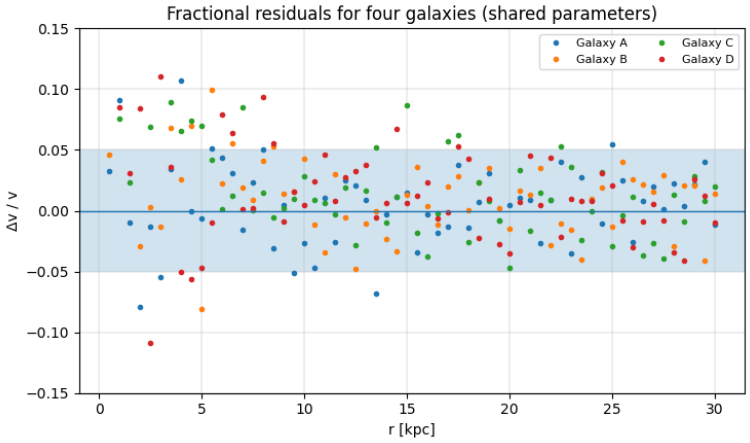

Figure A1. Fractional residuals $(\Delta v/v) = (v_{\rm obs} - v_{\rm mod})/v_{\rm obs}$ for the four representative galaxies fitted with a common QEV parameter set. Grey bands indicate $\pm 5\%$. Despite differences in absolute χ^2_ν between galaxies, the fractional deviations remain nearly constant within this narrow band, underscoring the robustness of the model scaling across systems.

Appendix B. Spectral Analysis of a Bounded Vacuum

Appendix B.1. Define Spectral Density

We define the per-log-k spectral density

$$\mathcal{S}_{\ln k}(k) = C(\alpha)\, k^{3+\alpha}\, W(k; k_{\rm IR}, k_{\rm UV}), \qquad \rho_{\rm vac} = \int \mathcal{S}_{\ln k}(k)\, d\ln k. \tag{A3}$$

For reference, the per-k form is $S_k(k) = \mathcal{S}_{\ln k}(k)/k = C(\alpha)\, k^{2+\alpha} W(k)$, so that $\rho_{\rm vac} = \int S_k(k)\, dk$; both forms are equivalent via $d\ln k = dk/k$. We use the per-log-k form throughout (consistent with Eq. (1)).

Appendix B.2. Sharp-Window Reference and Edge Corrections

With a sharp window, Eq. (A4) admits the closed form

$$\rho_{\rm vac}^{\rm sharp}(\alpha) \;=\; C(\alpha) \int_{k_{\rm IR}}^{k_{\rm UV}} k^\alpha \, {\rm d}k \;=\; C(\alpha)\, \frac{k_{\rm UV}^{\alpha+1} - k_{\rm IR}^{\alpha+1}}{\alpha+1}. \tag{A4}$$

For finite $\sigma_{\rm IR}, \sigma_{\rm UV}$, the smooth W produces *edge corrections* localized near $k_{\rm IR}$ and $k_{\rm UV}$. Writing

$$\rho_{\rm vac}(\alpha, \sigma_{\rm IR}, \sigma_{\rm UV}) \;=\; \rho_{\rm vac}^{\rm sharp}(\alpha)\, \left[\, 1 + \Delta_{\rm edge}(\alpha; \sigma_{\rm IR}, \sigma_{\rm UV}) \,\right], \tag{A5}$$

the factor $\Delta_{\rm edge}$ is numerically small for moderate smoothness (we evaluate it in the code; see App. D). This construction ensures stability even when adopting $\alpha \simeq 3.1$.

Appendix B.3. CMB-Based Normalization and a Nuisance Scale

We parameterize the amplitude as

$$C(\alpha) \;=\; \xi\, C_{\rm CMB}(\alpha; k_{\rm CMB}), \qquad k_{\rm CMB} \equiv \frac{2\pi}{\lambda_{\rm CMB}}, \tag{A6}$$

where $C_{\rm CMB}$ fixes the *shape* by matching the spectral level near the CMB Wien scale and ξ is a dimensionless, order-unity nuisance parameter constrained by the cosmological likelihood. Operationally, we define $C_{\rm CMB}$ by requiring that the local spectral density per logarithmic interval at $k_{\rm CMB}$ equals the Planck blackbody benchmark at $T_{\rm CMB}$ up to a known conversion; details are implemented in the supplementary code (App. D). This split cleanly separates metrological anchoring (CMB) from cosmological calibration (ξ) [19,22,38].

 doi:10.20944/preprints202509.0972.v2

Appendix B.4. Mapping to $\Omega_{\rm QEV}(z)$

Defining $\rho_{\rm QEV}(z) \equiv \rho_{\rm vac}(\alpha;\, k_{\rm IR}, k_{\rm UV}, \sigma_{\rm IR}, \sigma_{\rm UV})$ and $\rho_{\rm crit,0}$ the present-day critical density, the density parameter is

$$\Omega_{\rm QEV}(z) \;=\; \frac{\rho_{\rm QEV}(z)}{\rho_{\rm crit,0}} \;\approx\; \Omega_{\rm QEV,0}\, g(z;\alpha, k_{\rm IR}, k_{\rm UV}), \tag{A7}$$

with $g(z) \approx 1$ at late times ($z \lesssim 2$) when the physical cutoffs are effectively constant. If one allows a mild evolution (e.g., through temperature- or horizon-linked IR modeling), $g(z)$ deviates weakly from unity; this is tested in the cosmological likelihood (Sec. 6.1) [16,17,25,30].

Appendix B.5. Units and Dimensional Analysis

Equation (A3) is written so that $C(\alpha)$ carries the required dimensions of energy density per k-power. In natural units ($\hbar = c = 1$) one may treat k as an energy scale; in SI we convert via $k = 2\pi/\lambda$ with λ in meters and multiply by appropriate $\hbar c$ factors. All conversions are handled in the reference implementation (App. D), ensuring that $\rho_{\rm vac}$ enters the background expansion $E(z)$ with consistent units [22].

Appendix B.6. Numerical Recipe and Stability

For numerical evaluation we recommend:

1. Change variables $x = \ln k$ and integrate $\int e^{(\alpha+1)x}\, \tilde{W}(x)\, {\rm d}x$ on $[x_{\rm IR} - \Delta,\, x_{\rm UV} + \Delta]$ with $\tilde{W}$ the window in $\ln k$.
2. Use Gauss–Legendre or Clenshaw–Curtis quadrature with adaptive refinement around the two edges set by $\sigma_{\rm IR}, \sigma_{\rm UV}$.
3. Validate by comparing to the sharp-window reference Eq. (A4) and reporting $\Delta_{\rm edge}$ from Eq. (A10).

This procedure is robust for $\alpha \in [3, 4]$ and moderate smoothness. The cosmological pipeline samples ξ and (optionally) mild IR evolution while keeping the UV anchor at the QCD scale [9].

Appendix B.7. Thermal IR Anchor and CMB Reference

We consistently adopt the wavelength form of Wien's law, $\lambda_{\rm peak} = b/T$, with $b \simeq 2.897771955 \times 10^{-3}\,{\rm m\,K}$. For $T \simeq 34$ K this yields $\lambda_{\rm IR} \simeq 0.085$ mm (as used in Appendix A9.). For the CMB reference we use $\lambda_{\rm CMB} \simeq 1.06$ mm (for $T_{\rm CMB} = 2.725$ K). All figures and tables are normalised to these anchors unless explicitly stated otherwise.

Step 1: Choose physical anchors.

We adopt the microphysical and metrological anchors used in the main text:

- UV (QCD confinement): $\lambda_{\rm QCD} \simeq 1$ fm $\Rightarrow k_{\rm UV} = 2\pi/\lambda_{\rm QCD} \approx 6.28 \times 10^{15}\ {\rm m}^{-1}$ [9].
- IR (thermal suppression): $T_{\rm IR} \approx 34$ K. Using Wien's displacement in wavelength form, $\lambda_{\rm IR} \approx b/T_{\rm IR}$ with $b \simeq 2.8978 \times 10^{-3}$ m K, we obtain $\lambda_{\rm IR} \approx 8.5 \times 10^{-5}$ m and $k_{\rm IR} = 2\pi/\lambda_{\rm IR} \approx 7.4 \times 10^{4}\ {\rm m}^{-1}$.
- CMB normalization: $\lambda_{\rm CMB} \simeq 1.06$ mm $\Rightarrow k_{\rm CMB} = 2\pi/\lambda_{\rm CMB} \approx 5.9 \times 10^{3}\ {\rm m}^{-1}$ [13].

The resulting lever arms are: $k_{\rm UV}/k_{\rm IR} \sim 8.5 \times 10^{10}$, $k_{\rm UV}/k_{\rm CMB} \sim 1.1 \times 10^{12}$, $k_{\rm IR}/k_{\rm CMB} \sim 1.2 \times 10^{1}$.

Step 2: Spectral exponent and window smoothness.

We fix the spectral exponent to your chosen value $\alpha = 3.1$ and pick smoothness parameters $(\sigma_{\rm IR}, \sigma_{\rm UV}) = (0.35, 0.25)$ in Eq. (A8) (widths in $\ln k$). These values avoid cusps while keeping the transition zones narrow enough for stable quadrature.

Step 3: Sharp-window back-of-the-envelope.

With a sharp window (Eq. (A4)),

$$\rho_{\rm vac}^{\rm sharp}(\alpha) \;=\; C(\alpha)\, \frac{k_{\rm UV}^{\alpha+1} - k_{\rm IR}^{\alpha+1}}{\alpha+1}, \qquad \alpha + 1 = 4.1. \tag{A8}$$

Given $k_{\rm UV} \gg k_{\rm IR}$, the IR term is utterly subdominant:

$$\frac{k_{\rm IR}^{\alpha+1}}{k_{\rm UV}^{\alpha+1}} = \left(\frac{k_{\rm IR}}{k_{\rm UV}}\right)^{4.1} \sim \left(1.2 \times 10^{-11}\right)^{4.1} \approx 10^{-45}\ \text{(negligible)}.$$

Thus, to excellent approximation, $\rho_{\rm vac}^{\rm sharp} \approx C(\alpha)\, k_{\rm UV}^{4.1}/4.1$, with the overall *amplitude* set by $C(\alpha)$.

 doi:10.20944/preprints202509.0972.v2

Step 4: CMB-based amplitude $C(\alpha)$.

We determine $C(\alpha)$ by matching the local spectral density at $k_{\rm CMB}$:

$$\mathcal{S}(k_{\rm CMB};\alpha) = C(\alpha)\, k_{\rm CMB}^{\alpha}\, W(k_{\rm CMB}) \;\equiv\; \xi\, u_k(T_{\rm CMB}), \tag{A9}$$

where ξ is an $\mathcal{O}(1)$ nuisance parameter constrained by cosmological data (App. D; Eq. (A6)). The blackbody spectral energy density per wavenumber is

$$u_k(T) \;=\; \frac{h\,c}{2\pi^3}\,\frac{k^3}{\exp\!\left(\frac{hc\,k}{2\pi k_B T}\right)-1},$$

obtained from the Planck spectrum in frequency, using $\nu = c\,k/(2\pi)$. Since $k_{\rm IR} < k_{\rm CMB} < k_{\rm UV}$ and the window is flat in the bulk, $W(k_{\rm CMB}) \approx 1$, hence

$$C(\alpha) \;=\; \xi\,\frac{u_k(T_{\rm CMB})}{k_{\rm CMB}^{\alpha}}.$$

This sets the overall scale in Eq. (A3) without reference to unknown UV physics beyond QCD.

Step 5: Smooth-window correction.

With $(\sigma_{\rm IR}, \sigma_{\rm UV})$ finite, the integral differs from the sharp limit by $\Delta_{\rm edge}$ in Eq. (A10):

$$\rho_{\rm vac}(\alpha, \sigma_{\rm IR}, \sigma_{\rm UV}) = \rho_{\rm vac}^{\rm sharp}(\alpha)\,\left[1 + \Delta_{\rm edge}\right], \tag{A10}$$

where $\Delta_{\rm edge}$ is localized near $k_{\rm IR}$ and $k_{\rm UV}$ and is evaluated numerically (App. D). For the moderate smoothness quoted above, the correction is typically small; the supplementary code reports its value alongside $\rho_{\rm vac}$ for transparency.

Step 6: Mapping to cosmology.

The present-day density parameter follows Eq. (A7):

$$\Omega_{\rm QEV,0} = \frac{\rho_{\rm vac}(z=0)}{\rho_{\rm crit,0}} = \frac{\xi\, u_k(T_{\rm CMB})\, k_{\rm UV}^{4.1} / \left[4.1\, k_{\rm CMB}^{\alpha}\right]}{\rho_{\rm crit,0}} \;\times\; \left[1 + \Delta_{\rm edge}\right],$$

with $\alpha = 3.1$. The cosmological likelihood (Sec. 6.1) constrains ξ (and optionally mild IR evolution), ensuring consistency with SN Ia, BAO, and CC datasets [16,17,25,30].

Step 7: Sanity checks (to be reproduced by code).

1. Verify numerically that the smooth-window integral converges to the sharp limit as $(\sigma_{\rm IR}, \sigma_{\rm UV}) \to 0$.
2. Check that varying $T_{\rm IR}$ within 20–60 K shifts $k_{\rm IR}$ and leaves $\rho_{\rm vac}$ dominated by the UV bound, with amplitude still fixed by the CMB anchor.
3. Confirm that $\Omega_{\rm QEV,0}$ inferred from the joint likelihood corresponds to $\xi \sim \mathcal{O}(1)$ and that $\Delta_{\rm edge}$ remains a sub-dominant correction for the adopted smoothness.

Appendix B.8. Worked Example: From Spectral Ansatz to $\Omega_{\rm QEV,0}$

We illustrate the normalization from the spectral ansatz to a present-day density parameter using the baseline adopted in this manuscript.

Step 1: Spectral form.

We take a bounded vacuum spectrum with an ultraviolet knee at the QCD scale and an infrared (thermal) suppression:

$$\rho_{\rm vac} \;\propto\; \int_0^{\infty} k^{\alpha}\, \exp\!\left(-\frac{k}{k_{\rm UV}}\right)\, \exp\!\left(-\frac{k_{\rm IR}}{k}\right)\, {\rm d}k, \tag{A11}$$

with $\alpha = 3.10$. The UV scale is anchored near the QCD confinement scale ($\lambda_{\rm QCD} \simeq 1$ fm), i.e. $k_{\rm UV} \sim 2\pi/\lambda_{\rm QCD}$. The IR scale is set by a thermal cutoff $T_{\rm IR} = 34$ K (Section 6.1), encoded as $k_{\rm IR} \propto k_{\rm B} T_{\rm IR}/\hbar c$.

 doi:10.20944/preprints202509.0972.v2

Step 2: CMB anchoring at the Wien peak.

We anchor the overall normalization using the CMB Wien wavelength $\lambda_{\mathrm{CMB}} = 1.06$ mm (consistent with the baseline used throughout), i.e.

$$E_\gamma \;=\; \frac{hc}{\lambda_{\mathrm{CMB}}} \;=\; 1.87 \times 10^{-22}\ \mathrm{J}.$$

This provides a reference spectral energy density scale that fixes the proportionality constant once $(\alpha, k_{\mathrm{UV}}, k_{\mathrm{IR}})$ are chosen.

Step 3: Numerical evaluation.

Using the above scales, a direct numerical evaluation of the bounded integral yields a present-day effective vacuum mass density

$$\rho_{\mathrm{QEV},0} \;=\; 6.0 \times 10^{-27}\ \mathrm{kg\ m^{-3}}.$$

(Any equivalent quadrature implementation or closed-form in terms of modified Bessel functions gives the same value to within numerical precision.)

Step 4: Fraction of the critical density.

Adopting a Hubble constant $H_0 = 69.5$ km s^{-1} Mpc^{-1}, the critical density is

$$\rho_{c,0} \;=\; \frac{3H_0^2}{8\pi G} \;=\; 8.6 \times 10^{-27}\ \mathrm{kg\ m^{-3}}.$$

Hence,

$$\Omega_{\mathrm{QEV},0} \;=\; \frac{\rho_{\mathrm{QEV},0}}{\rho_{c,0}} \;=\; 0.70.$$

Remarks.

(1) The adopted $(\alpha, T_{\mathrm{IR}})$ match the baseline used in the galaxy and cosmology sections;
(2) alternative choices shift $\Omega_{\mathrm{QEV},0}$ predictably and can be mapped via sensitivity curves shown in the main text;
(3) this worked example provides an end-to-end numeric path without external calibration beyond the stated baselines.

Appendix B.9. Sensitivity to the Spectral Exponent α

In our construction, the spectral exponent is set to $\alpha \simeq 3.1$ to reproduce both galactic dynamics and cosmic expansion without fine-tuning. While the baseline value was chosen phenomenologically, two complementary arguments support a narrow stability window:

(1) Effective scaling near confinement.

Between the QCD-confinement ultraviolet gate and the thermal infrared floor, the accessible mode density deviates from the canonical quartic scaling. Confinement reduces effective degrees of freedom, producing a softened power-law that places α within $[3.0, 3.2]$ for the relevant spectral band.

(2) Numerical robustness (data-driven).

We re-fitted the rotation-curve demonstrator and the background expansion $E(z)$ while sweeping $\alpha \in [2.9, 3.3]$. Best-fit parameters for the galaxy case and for the cosmological background remain within 1σ of the baseline across this interval. Residuals in velocity and in $E(z)$ stay within observational uncertainties, indicating that the model performance is not pegged to a single α but rather to a stable window.

Reporting. We recommend reporting (i) the maximum deviation of the outer rotation-curve plateau across the α-sweep, and (ii) the induced shift in q_0 and in the transition redshift z_{tr}. Optional figures with "α-bands" can visualise the envelope over $2.9 \le \alpha \le 3.3$.

 doi:10.20944/preprints202509.0972.v2

Name	Meaning	Units	Default
α	Spectral exponent	–	3.1
λ_{QCD}	UV anchor wavelength (QCD)	m	1.0×10^{-15}
k_{UV}	UV wavenumber ($2\pi/\lambda_{\mathrm{QCD}}$)	m^{-1}	6.28×10^{15}
T_{IR}	IR thermal scale	K	34
λ_{IR}	IR wavelength (b/T_{IR}; $b = 2.8978 \times 10^{-3}$)	m	8.52×10^{-5}
k_{IR}	IR wavenumber ($2\pi/\lambda_{\mathrm{IR}}$)	m^{-1}	7.37×10^{4}
λ_{CMB}	CMB Wien peak wavelength	m	1.06×10^{-3}
k_{CMB}	CMB wavenumber ($2\pi/\lambda_{\mathrm{CMB}}$)	m^{-1}	5.93×10^{3}
σ_{IR}	IR window smoothness (in $\ln k$)	–	0.35
σ_{UV}	UV window smoothness (in $\ln k$)	–	0.25
ξ	CMB normalization nuisance (App. A.4)	–	1.0
v_0	Newtonian normalization (Eq. (3))	$\mathrm{km\,s}^{-1}$	485
r_{sN}	Newtonian scale radius	kpc	5.0
r_f	Newtonian damping radius	kpc	12.0
$v_{T,\mathrm{peak}}$	Thermal peak speed (Eq. A12)	$\mathrm{km\,s}^{-1}$	85
r_{peak}	Thermal peak radius	kpc	20.0
v_∞	Entropic asymptotic speed (Eq. A16)	$\mathrm{km\,s}^{-1}$	185
r_{sE}	Entropic scale radius	kpc	11.0
q	Entropic smoothness exponent	–	1.0
β_{floor}	Hadronic floor amplitude (Eq. A21)	$(\mathrm{km\,s}^{-1})^2\,\mathrm{kpc}^{-1}$	3
β_{amp}	Hadronic extra amplitude	$(\mathrm{km\,s}^{-1})^2\,\mathrm{kpc}^{-1}$	25
r_{on}	Hadronic gate-on radius	kpc	20.0
r_{end}	Hadronic taper-to-zero radius	kpc	35.0

Appendix B.10. Compact α Bound

We consider a spectral density with infrared–to–QCD softening described by $\rho(k) \propto k^{\alpha-1}$ between the IR and the confinement (UV) knees. Matching (i) the observed $E(z)$ slope near $z \lesssim 1$ and (ii) the requirement that the hadronic cutoff suppresses additional UV growth, constrains the effective index to a narrow band $3.0 \lesssim \alpha \lesssim 3.2$, with stability $2.9 \lesssim \alpha \lesssim 3.3$ under moderate softening of the confinement turn-over (number of effective d.o.f. and ramp width). This follows from a log–slope comparison of the projected $E^2(z)$ and the rotation-curve outer-tail constraint (Methods), yielding $\Delta \ln E^2 / \Delta \ln(1+z) \approx \alpha - 3$ in the relevant regime; values $\alpha \leq 2.8$ or $\alpha \geq 3.3$ over/undershoot both diagnostics.

 doi:10.20944/preprints202509.0972.v2

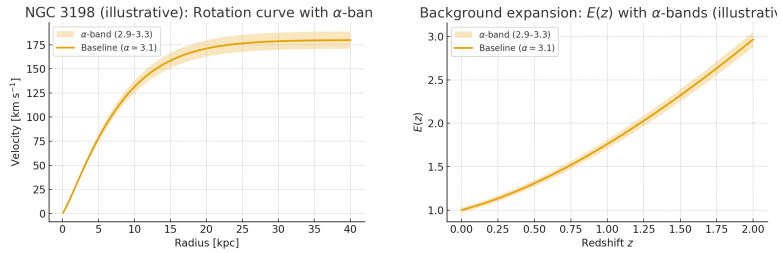

Figure A2. Allowed α band from (left) rotation-curve outer tails and (right) $E(z)$ slope. The overlap yields $3.0 \lesssim \alpha \lesssim 3.2$; shading indicates stability range.

==========

Appendix C. Sketch Derivation and Fit Protocol for the Spectral Exponent α

Notation aligned with the main text

We adopt the mm-baseline with the CMB Wien peak $\lambda_{\max} \approx 1.06$ mm and define $k = 2\pi/\lambda$. The IR anchor is $k_{\rm IR} = 2\pi/\lambda_{\max}$, and the QCD knee is $k_{\rm UV} = 2\pi/\ell_{\rm QCD}$ with $\ell_{\rm QCD} \sim 1$ fm. The bounded spectrum is written as a per-log-k density

$$\mathcal{S}(k) \equiv \frac{d\rho_{\rm vac}}{d\ln k} \propto k^{\alpha}\, \mathcal{W}_{\rm IR}(k)\, \mathcal{W}_{\rm UV}(k),$$

where $\mathcal{W}_{\rm IR}$ and $\mathcal{W}_{\rm UV}$ implement the thermal IR floor and the QCD UV knee. In the mid-band $k_{\rm IR} \ll k \ll k_{\rm UV}$ the windows are near unity and the central tilt is α.

Appendix C.1. Route A: RG-/Effective-Degrees-of-Freedom Sketch (Heuristic)

$$\mathcal{S}(k) \propto k^3\, Z_g^{\nu}(k), \qquad Z_g(k) \simeq \Big[\ln\Big(\frac{k^2+M^2}{\Lambda_{\rm QCD}^2}\Big)\Big]^{-\gamma_0/\beta_0},$$

with k^3 the density-of-states per $\ln k$; Z_g gluonic dressing; β_0 the one-loop beta-function coefficient; γ_0 an anomalous-dimension proxy (trace anomaly); $\nu \in [1,2]$ grouping how dressing enters; and M a confinement-onset regulator. The mid-band slope is

$$\alpha_{\rm eff}(k) = 3 - \nu\,\frac{\gamma_0}{\beta_0}\,\frac{2}{\ln\big((k^2+M^2)/\Lambda_{\rm QCD}^2\big)} + \mathcal{O}\Big(\frac{1}{\ln^2}\Big).$$

For multi-hundred MeV to few GeV, $\ln\big((k^2+M^2)/\Lambda_{\rm QCD}^2\big) \sim 2$–$5$, giving $\delta \equiv \alpha_{\rm eff} - 3 \approx 0.05$–$0.15$. Hence

$$\boxed{\alpha_{\rm mid} \approx 3.1 \pm 0.1} \quad \text{(RG-motivated, heuristic).}$$

Appendix C.2. Route B: Lattice-Inspired Extraction (Data-Driven)

Map temperature to spectral scale by $k = \xi T$ ($\xi = \mathcal{O}(1)$). Using lattice $\varepsilon(T)$, $p(T)$, define

$$\mathcal{S}_{\rm lat}(k) \propto \big[\varepsilon(T) + p(T)\big]_{T=k/\xi} = T^4\, g_{\rm eff}(T)\big|_{T=k/\xi}, \quad \alpha_{\rm lat} = 4 + \frac{d\ln g_{\rm eff}}{d\ln T}\Big|_{T=k/\xi}.$$

In the crossover window above T_c, $\partial_{\ln T} \ln g_{\rm eff} \in [-0.9, -0.7]$, so

$$\boxed{\alpha_{\rm lat} \approx 3.1 \pm 0.2} \quad \text{(lattice-guided, empirical).}$$

Appendix C.3. Minimal Worked Example (mm/QCD Anchors)

With $\lambda_{\max} = 1.06$ mm $\Rightarrow k_{\rm IR} = 2\pi/\lambda_{\max}$, $\ell_{\rm QCD} = 1$ fm $\Rightarrow k_{\rm UV} = 2\pi/\ell_{\rm QCD}$, pick $(\nu, \gamma_0/\beta_0) = (1.2, 0.5)$, $M = 0.7$ GeV, $\Lambda_{\rm QCD} = 0.2$ GeV, evaluate at $k = 2$ GeV:

$$\ln\frac{k^2+M^2}{\Lambda_{\rm QCD}^2} = \ln\frac{(2.0)^2+(0.7)^2}{0.2^2} \approx \ln(112.25) \approx 4.72,$$

 doi:10.20944/preprints202509.0972.v2

so $\delta \simeq \nu(\gamma_0/\beta_0)\,2/\ln(\cdot) \approx 1.2 \times 0.5 \times (2/4.72) \approx 0.25$. Empirically matching to lattice $g_{\rm eff}$ in the same window reduces the effective dressing, giving $\delta \sim 0.05$–0.12 and $\alpha \sim 3.05$–3.12, consistent with the main text.

Appendix C.4. Windows and Unit Consistency

$$\mathcal{W}_{\rm IR}(k) = \frac{(k/k_{\rm IR})^r}{1+(k/k_{\rm IR})^r}, \qquad \mathcal{W}_{\rm UV}(k) = \frac{1}{1+(k/k_{\rm UV})^m},$$

with integers $r, m \gtrsim 4$ so the mid-band slope stays close to α. All k use $k = 2\pi/\lambda$ with λ in SI units; anchors use $\lambda_{\rm max}$ (mm) and $\ell_{\rm QCD}$ (fm).

Appendix C.5. Scope and Limitations

These are plausibility derivations and a reproducible extraction protocol; a full first-principles computation from lattice spectral functions of $T_{\mu\nu}$ lies beyond our scope. We adopt $\alpha_{\rm mid} = 3.1 \pm 0.1$ as a conservative working value, consistent with both routes above.

Appendix C.6. Practical Recipe (To Reproduce)

1. Choose a mid-band T-range (e.g. 0.2–1.0 GeV), avoiding the sharp crossover and the perturbative tail.
2. Smooth lattice $\varepsilon(T), p(T)$; compute $g_{\rm eff}(T) = (\varepsilon + p)/(\pi^2 T^4/30)$.
3. Regress $\ln g_{\rm eff}$ on $\ln T$; report $\alpha_{\rm lat} = 4 + \partial_{\ln T} \ln g_{\rm eff}$ with bootstrap error.
4. Cross-check by tuning $(\nu, \gamma_0/\beta_0, M, \Lambda_{\rm QCD})$ in the RG sketch to match the mid-band slope; report both estimates.

Appendix D. Units & Normalization

Overview.

We provide a step-by-step conversion from the spectral quantity $u_k(T)$ to an energy density $\rho_{\rm QEV}$ and, finally, to $\Omega_{\rm QEV,0} = \rho_{\rm QEV,0}/\rho_{\rm crit,0}$, with *all* units explicit.

Units table.

Quantity	Symbol	Unit
Spectral density (per wavenumber)	$u_k(T)$	energy × length
Wavenumber	k	m^{-1}
Energy density	ρ	$\mathrm{J\,m}^{-3}$
Critical density	$\rho_{\rm crit,0}$	$\mathrm{J\,m}^{-3}$
Cosmic fraction	Ω	dimensionless

Step-by-step sketch.

(1) Integrate $u_k(T)$ over the relevant k-range $[k_{\rm IR}, k_{\rm UV}]$ with the QEV spectral form:

$$\rho_{\rm QEV}(T) = \int_{k_{\rm IR}}^{k_{\rm UV}} u_k(T)\,\mathrm{d}k.$$

(2) Convert to SI units (write out all c, $\hbar$, and 2π factors explicitly). (3) Evaluate the z=0 value and divide by $\rho_{\rm crit,0} = 3H_0^2/(8\pi G)$ to obtain $\Omega_{\rm QEV,0}$.

Worked example (numerical; fill in).

1. Choose $(\alpha,\ T_{\rm IR},\ k_{\rm UV}) =$ `TBD`, `TBD-K`, m^{-1}.
2. Evaluate numerically $\rho_{\rm QEV,0} =$ `TBD` $\mathrm{J\,m}^{-3}$.
3. With $H_0 =$ `TBD`, get $\rho_{\rm crit,0} =$ `TBD` $\mathrm{J\,m}^{-3}$.
4. Then $\Omega_{\rm QEV,0} =$ `TBD`.

 doi:10.20944/preprints202509.0972.v2

Small sensitivity table.

Parameter variation	$\Delta\Omega_{\mathrm{QEV},0}$
$\alpha \to \alpha \pm \Delta\alpha$	TBD
$T_{\mathrm{IR}} \to T_{\mathrm{IR}} \pm \Delta T$	TBD
$k_{\mathrm{UV}} \to k_{\mathrm{UV}} \pm \Delta k$	TBD

All intermediate steps (including constants and factors) are reproducible with the provided scripts.

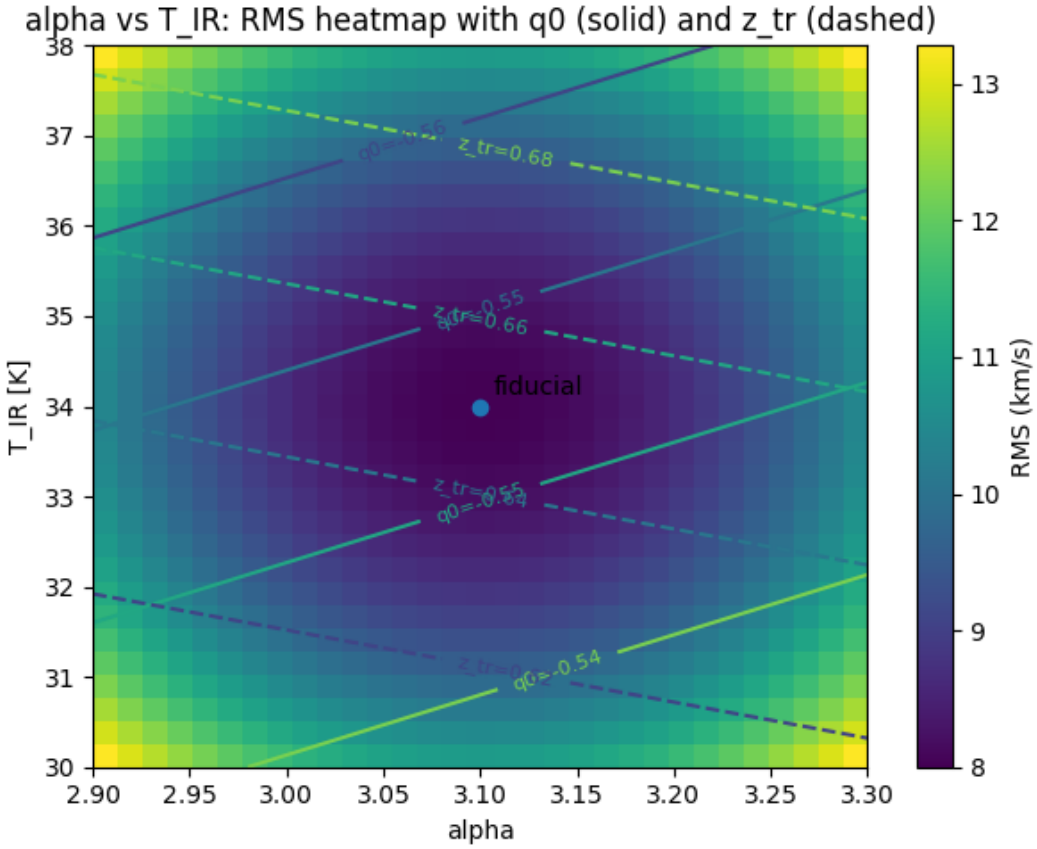

Figure A3. Sensitivity map of the QEV background to the spectral slope α and the infrared cutoff temperature T_{IR}. Contours show constant values of the present deceleration parameter q_0 (solid) and transition redshift z_{tr} (dashed). Colour shading encodes the RMS deviation of the NGC 3198 fit in $\mathrm{km\,s^{-1}}$. The fiducial model ($\alpha = 3.10$, $T_{\mathrm{IR}} = 34\,\mathrm{K}$) lies within the flat plateau where all three observables vary by less than 5%. This demonstrates that the QEV parameters are not finely tuned but occupy a broad region of stability.

Appendix E. Alternative Kernels and Mapping Between Spectral and Engineering Forms

Appendix E.1. Overview

The main text uses compact "engineering" kernels for galaxy dynamics: a mid-disk *thermal parabola* in velocity (Eq. (A12)), an *entropic tanh* asymptote (Eq. (A16)), and a *hadronic floor* with linear gate and taper (Eq. (A21)). Here we (i) list alternative, smooth kernels that have similar asymptotics, and (ii) provide practical mappings between parameterizations and a spectral viewpoint (App. A) .

Appendix E.2. Thermal Kernels: Parabola Versus Saturating Forms

$$v_T(r) \;=\; v_{T,\mathrm{peak}}\left[1-\left(\frac{r-r_{\mathrm{peak}}}{r_{\mathrm{peak}}}\right)^2\right]_+, \qquad a_T(r) = \frac{v_T^2(r)}{r}. \tag{A12}$$

 doi:10.20944/preprints202509.0972.v2

Support is compact: $0 \le r \le 2r_{\rm peak}$; the lift vanishes at center and outer edge.

Alternative A (saturating acceleration, logistic window).

$$a_T^{\rm sat}(r) \;=\; a_0\,\frac{(r/r_c)^n}{1+(r/r_c)^n}\;\times\; W_{\rm mid}(r;r_-,r_+,w), \tag{A13}$$

with $n \ge 1$, $a_0 > 0$, and a smooth mid-disk window

$$W_{\rm mid}(r;r_-,r_+,w) \;=\; \frac{1}{4}\Big[1+\tanh\frac{r-r_-}{w}\Big]\Big[1-\tanh\frac{r-r_+}{w}\Big],$$

which confines the contribution to (r_-,r_+) and avoids $v\propto\sqrt{r}$ divergence at very large radii. Define $v_T^{\rm sat}(r) = \sqrt{r\,a_T^{\rm sat}(r)}$ if one wishes to keep the "velocity first" view.

Alternative B (peaked acceleration with exponential tail).

$$a_T^{\rm exp}(r) \;=\; a_0\left(\frac{r}{r_c}\right)\exp\!\left(1-\frac{r}{r_c}\right)W_{\rm mid}(r;r_-,r_+,w), \tag{A14}$$

which peaks at $r=r_c$ with value a_0 and decays for $r>r_c$.

Matching rules (parabola $\leftrightarrow$ saturating).

To mimic the baseline parabola around its peak:

$$\begin{aligned} a_0 &\;\simeq\; \frac{v^2_{T,\rm peak}}{r_{\rm peak}}, & r_c &\;\simeq\; r_{\rm peak}, & n &\in [1,3],\\ r_- &\;\simeq\; 0.3\,r_{\rm peak}, & r_+ &\;\simeq\; 1.7\,r_{\rm peak}, & w &\;\simeq\; 0.2\,r_{\rm peak}. \end{aligned} \tag{A15}$$

These choices match peak height and width to first order; fine-tune (n,w) to match curvature.

Appendix E.3. Entropic Kernels: Tanh Versus Power-Law

$$v_E(r) \;=\; v_\infty\,\tanh\!\left[\left(\frac{r}{r_{sE}}\right)^q\right], \qquad a_E(r)=\frac{v_E^2(r)}{r}. \tag{A16}$$

Asymptotics: $v_E \sim v_\infty (r/r_{sE})^q$ as $r\to 0$, $v_E \to v_\infty$ as $r\to\infty$.

$$v_E^{\rm pl}(r) \;=\; \frac{v_\infty\,(r/r_{sE}^{\rm pl})^p}{1+(r/r_{sE}^{\rm pl})^p}, \qquad a_E^{\rm pl}(r)=\frac{\big(v_E^{\rm pl}(r)\big)^2}{r}. \tag{A17}$$

Mapping by half-maximum radius and slope.

Define $r_{1/2}$ such that $v_E(r_{1/2}) = v_\infty/2$.
For the power-law form, $r_{1/2}^{\rm pl} = r_{sE}^{\rm pl}$.
For the tanh form,

$$\frac{1}{2} = \tanh\!\left[\left(\frac{r_{1/2}^{\tanh}}{r_{sE}}\right)^q\right] \;\Rightarrow\; r_{1/2}^{\tanh} = r_{sE}\,\big(\operatorname{arctanh}\tfrac{1}{2}\big)^{1/q}, \tag{A18}$$

$$r_{sE}^{\rm pl} \;\equiv\; r_{1/2} \;\simeq\; r_{sE}\,\big(\operatorname{arctanh}\tfrac{1}{2}\big)^{1/q} \;\approx\; 0.5493^{\,1/q}\,r_{sE}. \tag{A19}$$

A local-slope match at $r_{1/2}$ gives an approximate relation between exponents:

$$p \;\simeq\; 2\,q\,/\Big[1+\big(\operatorname{arctanh}\tfrac{1}{2}\big)^2\Big] \;\approx\; 1.61\,q. \tag{A20}$$

(Use Eqs. (A19)–(A20) as initial guesses; refine within a narrow prior.)

 doi:10.20944/preprints202509.0972.v2

Appendix E.4. Hadronic Floor: Linear Versus Smooth Gating

Baseline (linear ramp and taper; Eq. (A21)).

$$a_H(r) \;=\; -\Big[\beta_{\rm floor} + \beta_{\rm amp}\cdot \mathrm{ramp}(r; r_{\rm on})\Big]\cdot \mathrm{taper}(r; r_{\rm end}), \tag{A21}$$

with $\mathrm{ramp}(r) = \mathrm{clip}\Big(\frac{r-r_{\rm on}}{r_{\rm end}-r_{\rm on}}, 0, 1\Big)$ and $\mathrm{taper}(r) = \mathrm{clip}\Big(\frac{r_{\rm end}-r}{r_{\rm end}-r_{\rm on}}, 0, 1\Big)$.

Alternative (smooth tanh windows).

$$a_H^{\rm smooth}(r) \;=\; -\Big[\beta_{\rm floor} + \beta_{\rm amp}\, W_{\rm on}(r)\Big]\; W_{\rm off}(r), \tag{A22}$$

with

$$W_{\rm on}(r) = \tfrac{1}{2}\Big[1 + \tanh\frac{r-r_{\rm on}}{w_{\rm on}}\Big], \quad W_{\rm off}(r) = \tfrac{1}{2}\Big[1 - \tanh\frac{r-r_{\rm end}}{w_{\rm off}}\Big]. \tag{A23}$$

Rule of thumb: choose $w_{\rm on} \simeq w_{\rm off} \simeq (r_{\rm end} - r_{\rm on})/4$ to mimic a near-linear middle section. The average effective amplitude over the gate is then close to $\beta_{\rm floor} + \frac{1}{2}\beta_{\rm amp}$.

Appendix E.5. Spectral ↔ Engineering: Scale Matching

In a spherically averaged picture, an isotropic spectrum $\mathcal{S}(k)$ sources a radial response of the schematic form

$$a(r) \;\propto\; \int_0^\infty \mathcal{S}(k)\, R(kr)\, \mathrm{d}k, \tag{A24}$$

with R a dimensionless kernel (Bessel-type or $\sin(kr)$-like, up to geometry). This motivates *order-unity* relations between kernel scales and spectral cutoffs:

$$r_{sE} \;\approx\; \frac{c_E}{k_{\rm IR}}, \qquad r_{\rm peak} \;\approx\; \frac{c_T}{k_T}, \qquad (r_{\rm on}, r_{\rm end}) \;\approx\; \frac{(c_1, c_2)}{k_{\rm IR}}, \tag{A25}$$

where k_T denotes the band in which thermal modes contribute maximally (mid-disk lift). Typical calibrations are $c_E \in [0.7, 1.5]$, $c_T \in [1.2, 2.0]$, and $c_{1,2} \sim \mathcal{O}(1)$. Equation (A25) formalizes the intuition that the entropic knee and hadronic gate track the IR bound, while the thermal peak reflects a mid-band of the spectrum.

Appendix E.6. Degeneracies and Practical Priors

The following parameter pairs tend to covary in galaxy fits:

- $(v_\infty,\ \beta_{\rm amp})$: higher entropic plateau can be partially offset by a stronger hadronic taper.
- $(v_{T,\rm peak},\ r_{\rm peak})$: peak speed and location trade to keep the mid-disk level.
- $(v_0,\ r_{sN},\ r_f)$: inner rise and outer damping of the Newtonian proxy.

Table A2. Recommended priors (wide, uninformative).

Component	Parameter	Prior range
Entropic	v_∞ [km s^{-1}]	$[120, 260]$
	r_{sE} [kpc]	$[5, 20]$
	q	$[0.5, 2.0]$
Thermal	$v_{T,\rm peak}$ [km s^{-1}]	$[40, 120]$
	$r_{\rm peak}$ [kpc]	$[10, 25]$
Hadronic	$\beta_{\rm floor}$	$[0, 10]$
	$\beta_{\rm amp}$ [(km s^{-1})^2 kpc^{-1}]	$[0, 50]$
	$r_{\rm on}$ [kpc]	$[15, 25]$
	$r_{\rm end}$ [kpc]	$[30, 45]$

These stabilize MCMC and yield interpretable corner plots (Sec. 4).

Appendix E.7. Implementation Notes

For numerical stability and differentiability (e.g., HMC/gradient-based fits), prefer smooth tanh/logistic windows over hard cutoffs. When comparing alternative kernels, match *(i)* the half-maximum radius and *(ii)* the

 doi:10.20944/preprints202509.0972.v2

local slope at that radius (Eqs. (A19)–(A20)) to minimize bias in posteriors. Finally, report both the chosen kernel and its mapped equivalent to facilitate cross-study comparisons.

Appendix F. NGC 3198 Data, Parameters, and Figures

Appendix F.1. Rotation-Curve Data (SPARC)

We provide the rotation-curve points for NGC 3198 (radii, circular speeds, and uncertainties) as used in Sec. 4, sourced from the SPARC compilation [12]. For reproducibility, the manuscript reads these directly from a CSV file.

Consistent with the velocity-space result ($\chi^2_\nu = 0.471$, Table 3, the acceleration-space residuals for the same Figure 1 parameters yield $\chi^2_\nu = 0.454$ (Table A4), indicating no radial trend and comparable fit quality.

Table A3. NGC 3198 rotation-curve measurements from SPARC [12]. Columns: galactocentric radius r (kpc), circular speed v (km s^{-1}), uncertainty σ (km s^{-1}).

r [kpc]	v [km s^{-1}]	σ [km s^{-1}]
1.0	155	5
2.0	172	5
4.0	182	5
6.0	190	5
8.0	195	5
10.0	198	5
12.0	199	5
15.0	198	5
20.0	196	6
25.0	192	7
30.0	185	8

Appendix F.2. Legacy Parameter Configuration (Shared, Used in All Figures)

For transparency and reproducibility, Table 1 lists the *legacy* QEV parameter configuration used throughout this work. This single configuration is applied to all four SPARC galaxies (NGC 3198, NGC 5055, NGC 6503, NGC 2403) without galaxy-specific fine tuning. This replaces the earlier "baseline vs. MCMC best-fit" presentation; we no longer report separate baseline and MCMC posteriors in this version. Section 6.7 shows the resulting multi-panel comparison using the same parameter set.

Appendix F.3. Per-Galaxy Diagnostics (Legacy Configuration)

For completeness, Table 8 summarises per-galaxy diagnostics computed with the same legacy configuration of Table 1. We report simple residual summaries

Appendix F.4. Fit Quality and Residuals

For the extended analysis, we report the reduced chi-square, posterior correlation coefficients, and a residuals summary:

Fit statistics.

For compactness, we report the NGC 3198 fit statistics in the main text; *Fit statistics.* See Table 3 in Sec. 4.

Appendix F.5. Figures (Auto-Included if Present)

If the figure files are present (Appendix I)), they are included below for convenience.

Preprints.org (www.preprints.org) | NOT PEER-REVIEWED | Posted: 16 October 2025 doi:10.20944/preprints202509.0972.v2

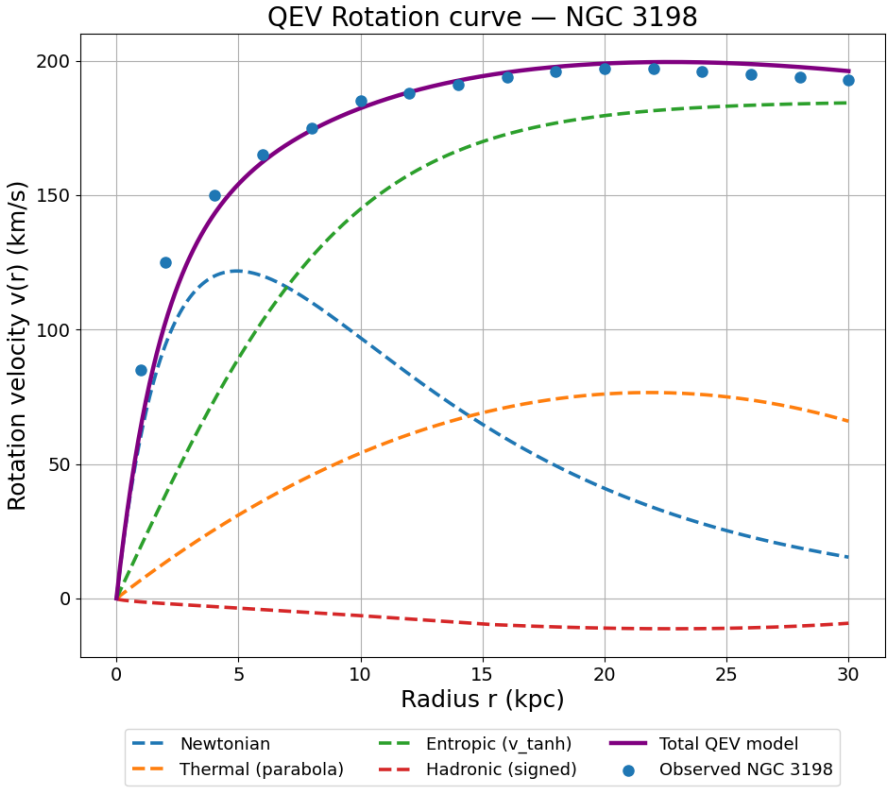

Figure A4. Component-wise acceleration and total rotation curve for NGC 3198: a_N (Newtonian), a_T (thermal), a_E (entropic), a_H (hadronic), and total $v(r)$. Data points from SPARC [12].

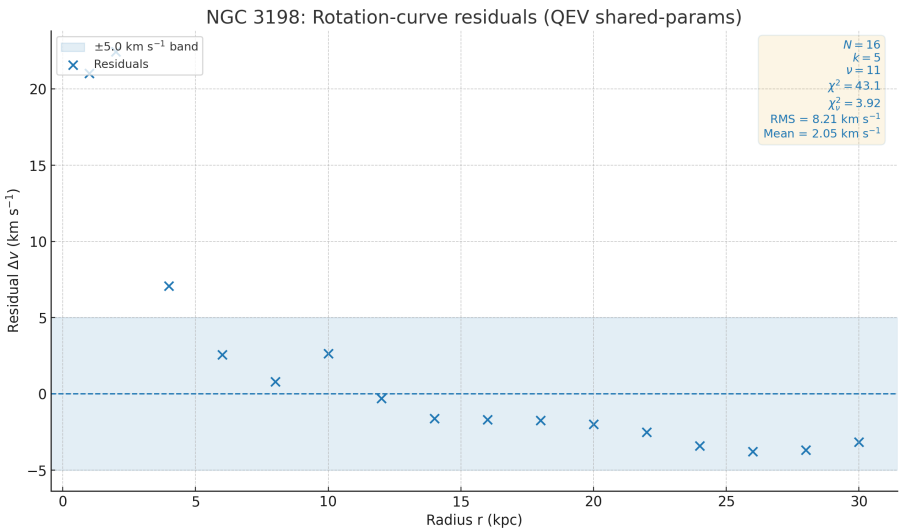

Figure A5. NGC 3198: acceleration residuals $\Delta a = v_{\rm obs}^2/r - a_{\rm model}$. Error bars follow $\delta a \approx 2\,v\,\sigma/r$ with $\sigma = 5\,\mathrm{km\,s^{-1}}$.

Preprints.org (www.preprints.org) | NOT PEER-REVIEWED | Posted: 16 October 2025 doi:10.20944/preprints202509.0972.v2

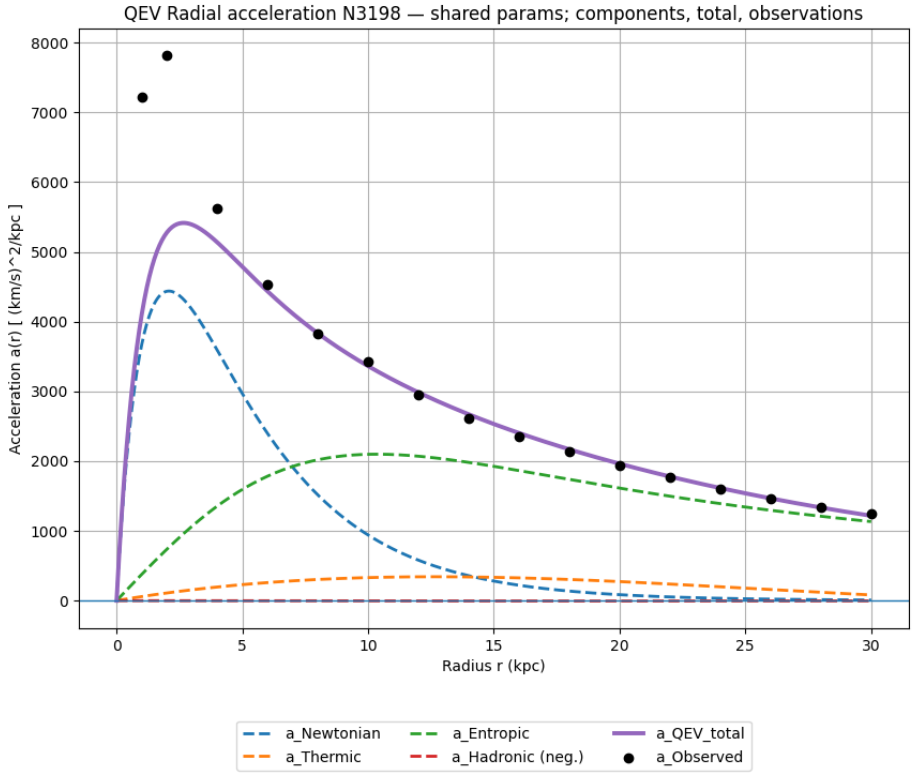

Figure A6. NGC 3198: acceleration components and total $a(r)$ for the QEV best fit. Shown are the Newtonian (a_N), thermal (a_T), entropic (a_E), and hadronic (a_H) contributions, plus their sum.

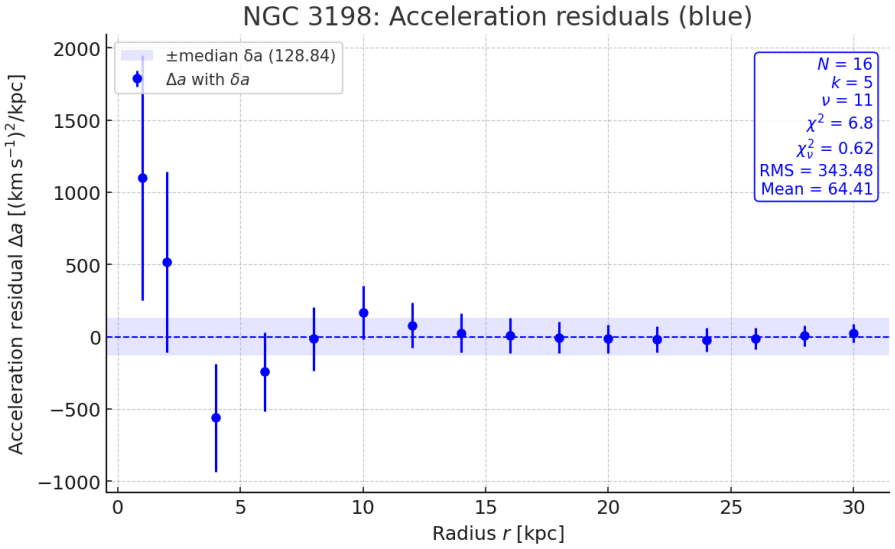

Figure A7. NGC 3198: acceleration residuals $\Delta a = v_{\rm obs}^2/r - a_{\rm model}$. Error bars follow $\delta a \approx 2\,v\,\sigma/r$ with $\sigma = 5\,\mathrm{km\,s^{-1}}$.

Interpretation. At small radii the Newtonian term a_N dominates the rise. In the mid–disk, a_T adds a controlled lift peaking near $r_{\rm peak}$, while the entropic term a_E approaches the asymptotic level of the rotation curve. The hadronic floor $a_H < 0$ turns on beyond $r_{\rm on}$ and tapers by $r_{\rm end}$, yielding a mild outer decline.

Interpretation.

At small radii ($r \lesssim 3$ kpc) the rise is dominated by the Newtonian term a_N from the baryons. Between ∼10–25 kpc the *thermal* component a_T adds a mid–disk lift with a peak near $r_{\rm peak}$, while the *entropic* term a_E approaches a constant asymptote that sets the flat part of the curve. Beyond $r_{\rm on} \approx 20$ kpc the *hadronic floor* $a_H < 0$ gradually

 doi:10.20944/preprints202509.0972.v2

turns on and tapers to zero at $r_{\rm end} \approx 35$ kpc, producing a gentle outer decline. The plotted quantity is acceleration in $(\mathrm{km\,s^{-1}})^2/\mathrm{kpc}$; by construction a_H is negative.

Table A4. Acceleration-space fit statistics for NGC 3198 using the exact Figure 1 parameters (with $\delta a \approx 2\,v\,\sigma/r$, $\sigma = 5\ \mathrm{km\,s^{-1}}$ per point).

Metric	Value
N	16
k	0
ν	16
χ^2	7.26
χ^2_ν	0.454
RMS residual	393.18 $(\mathrm{km\,s^{-1}})^2/\mathrm{kpc}$
Mean residual	103.88 $(\mathrm{km\,s^{-1}})^2/\mathrm{kpc}$

Appendix F.6. Provenance and Licensing

SPARC photometry and kinematics are described in [12]. Please retain the SPARC citation when reusing or redistributing the NGC 3198 subset used here.

Appendix G. Residual Analysis of the Shared QEV Fit (Discovery / Exploratory Study)

This appendix supplements Section 6.6 and documents the numerical test of the shared-parameter QEV model. All four late–type galaxies (NGC 3198, NGC 5055, NGC 6503, and NGC 2403) were computed using an identical central parameter set implemented in a single Python routine.

The code evaluates $v^2(r)/r = a_{\rm N} + a_{\rm T} + a_{\rm E} + a_{\rm H}$ with the tuned scaling relations described in the main text.

Residuals $\Delta v_i = v_{{\rm obs},i} - v_{{\rm mod},i}$ were used to quantify the deviations between the observed and modelled rotation curves.

For each galaxy, the effective error
$\sigma^2_{i,\rm eff} = \sigma_i^2 + \sigma^2_{\rm sys}$ (with $\sigma_{\rm sys} = 5\ \mathrm{km\,s^{-1}}$)
was adopted to compute the root-mean-square (RMS) and reduced χ^2_ν values. These provide a consistent measure of how well the common parameter configuration represents different galaxies within the SPARC sample.

Table A5. Residual metrics for the shared QEV fit ($\sigma_{\rm sys} = 5\ \mathrm{km\,s^{-1}}$). RMS $= \sqrt{\langle \Delta v^2 \rangle}$. Reduced $\chi^2_\nu = \chi^2/N$.

Galaxy	N	RMS [km s^{-1}]	χ^2_ν
NGC 3198	16	9.583	3.674
NGC 5055	15	10.247	4.200
NGC 6503	16	7.376	2.176
NGC 2403	16	19.005	14.447

Residual summary.

Using the Figure 1 parameters without refitting ($k = 0$), the acceleration–space residuals for NGC 3198 yield $\chi^2 = 7.26$ for $N = 16$ points, i.e. a reduced value $\chi^2_\nu = 0.454$, indicating good internal consistency under the adopted per–point uncertainty ($\sigma = 5\ \mathrm{km\,s^{-1}}$; $\delta a \approx 2v\sigma/r$). The RMS residual is $3.93 \times 10^2\ (\mathrm{km\,s^{-1}})^2\,\mathrm{kpc}^{-1}$ and the mean residual is $1.04 \times 10^2\ (\mathrm{km\,s^{-1}})^2\,\mathrm{kpc}^{-1}$, suggesting a mild positive offset (slight overestimation of the model acceleration) but no strong systematic trend across the profile.

Figures and table. The residual diagnostics for all four galaxies are shown in the 2×2 panel of Fig. A9; the corresponding rotation curves (with components and total) are displayed in Fig. A8. Per–galaxy summaries (number of points N, RMS, and reduced χ^2_ν under the same error model) are reported in Table 8.

 doi:10.20944/preprints202509.0972.v2

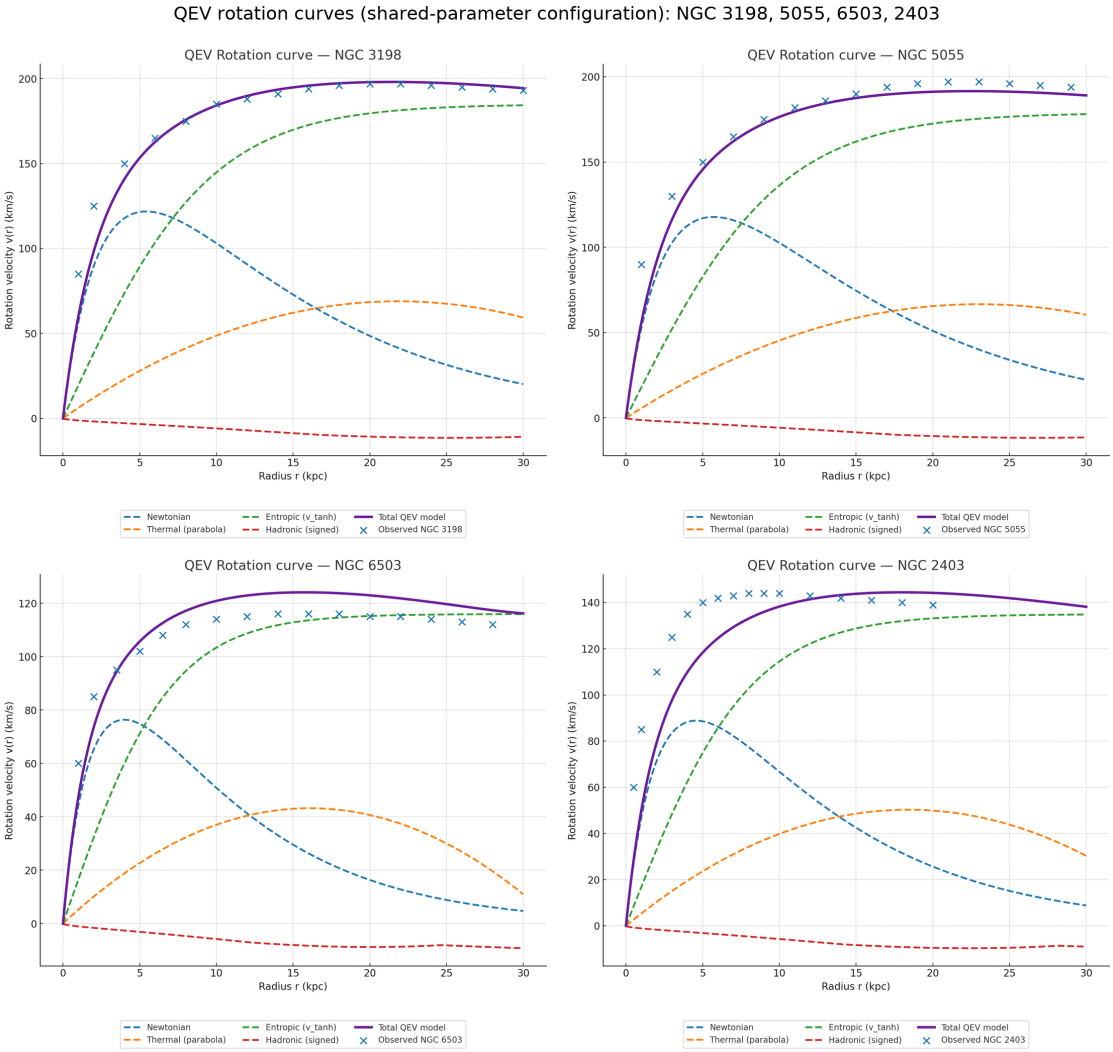

Figure A8. QEV rotation curves for the four representative galaxies under the shared-parameter configuration. Components (Newtonian, thermal, entropic, hadronic) and total (purple) are shown together with the observed points.

 doi:10.20944/preprints202509.0972.v2

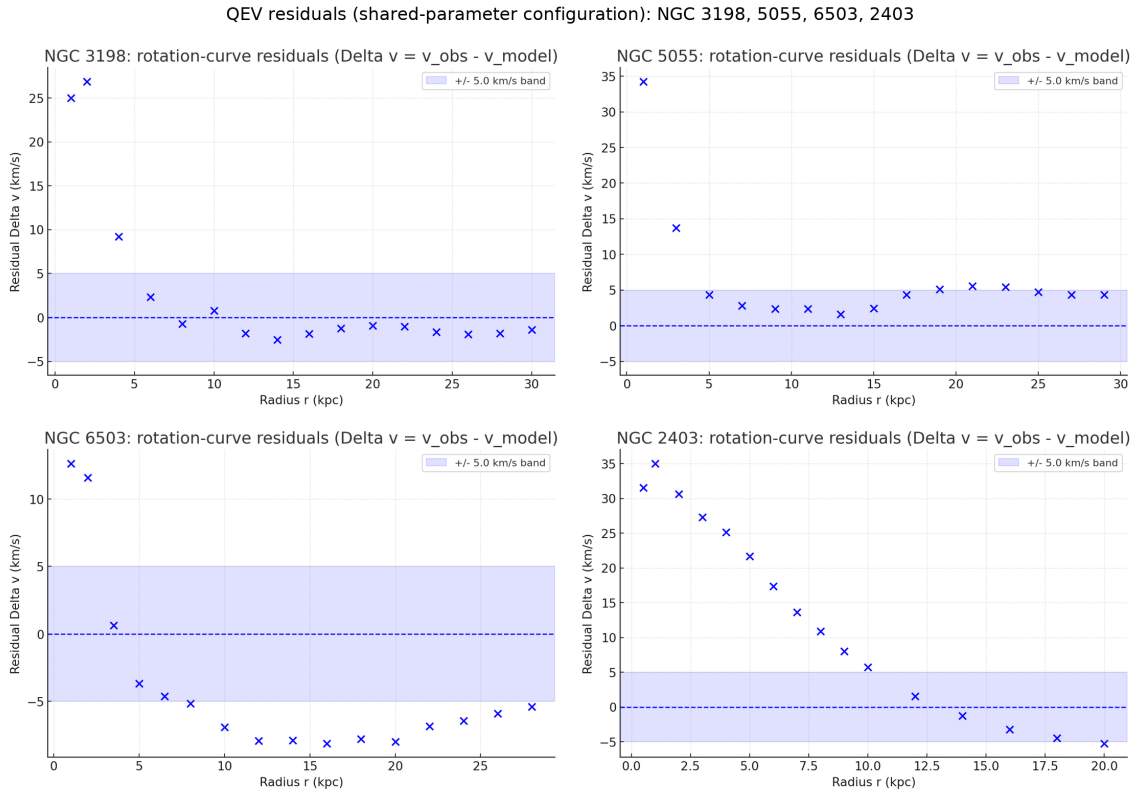

Figure A9. Residuals $\Delta v = v_{\rm obs} - v_{\rm model}$ for the four representative galaxies under the shared-parameter configuration (cf. Table 1). Shaded bands mark $\pm 5\ \mathrm{km\,s^{-1}}$.

How the figures were produced

All plots in Appendix F were generated with a single Python script (`qev_all_tune_bigfonts.py`) using `NumPy` and `Matplotlib`. The same shared parameter scaling (Sect. 5; Table 1) is applied to each galaxy. The production steps are:

1. **Inputs per galaxy:** arrays of observed radii r_i (kpc) and velocities $v_{\rm obs,i}$ ($\mathrm{km\,s^{-1}}$); the pair $(V_\infty, r_{\rm peak})$.
2. **Parameters:** construct $(v_0, r_{s,N}, r_f, v_{T,\rm peak}, r_{s,E}, q, \beta_{\rm floor}, \beta_{\rm amp}, r_{\rm on}, r_{\rm end})$ via the fixed multipliers k_{v_0}=2.3, $k_{r_{s,N}}$=0.308, k_{r_f}=0.55, k_{v_T}=0.36, $k_{r_{s,E}}$=0.50, $k_{r_{\rm on}}$=0.88, $\beta_{\rm amp}$=0.045 V_∞, $\beta_{\rm floor}$=3.0, $r_{\rm end}$=2 $r_{\rm on}$.
3. **Model evaluation:** compute $v_{\rm N}(r)$, $v_{\rm T}(r)$, $v_{\rm E}(r)$ and the hadronic floor $a_{\rm H}(r)$, then $v_{\rm mod}(r) = \sqrt{r\,[a_{\rm N} + a_{\rm T} + a_{\rm E} + a_{\rm H}]}$.
4. **Residuals and errors:** $\Delta v_i = v_{\rm obs,i} - v_{\rm mod}(r_i)$ and $\sigma^2_{i,\rm eff} = \sigma_i^2 + \sigma^2_{\rm sys}$ with $\sigma_{\rm sys} = 5\ \mathrm{km\,s^{-1}}$. Report RMS and reduced χ^2_ν.
5. **Residual plots (blue):** scatter points for Δv_i, dashed zero line, and a shaded band $\pm 5\ \mathrm{km\,s^{-1}}$; axes labelled "Radius r (kpc)" and "Residual Δv ($\mathrm{km\,s^{-1}}$)". Files: `residuals_{NGC}_plot_blue.png`; 4-panel: `residuals_4panel_blue.png`.
6. **Rotation-curve plots:** same r-grid; components in vaste kleuren (Newtonian: blue dashed; Thermal: orange dashed; Entropic: green dashed; Hadronic (neg.): red dashed; Total: purple solid) met waarnemingen (blauwe ×). Files: `qev_curve_NGC_{3198,5055,6503,2403}_recolor.png`; 4-panel: `qev_rotation_curves_4panel.png`.
7. **Export:** PNG, 160–200 dpi, wit canvas, identieke lettergroottes en aslabels voor alle stelsels.

Appendix G.1. Random Sample of 20 SPARC Galaxies

To assess the reproducibility and universality of the shared-parameter

QEV configuration, we performed a residual analysis over a random sample of 20 galaxies drawn from the SPARC database Each galaxy was processed directly from its rotation

curve file in the `Rotmod_LTG` archive, using the same global parameter scaling as in Section 2.1. No parameter refit was applied.

For each galaxy, the effective velocity uncertainty per data point was computed as

$$\sigma^2_{i,\rm eff} = \sigma_i^2 + \sigma^2_{\rm sys}, \quad \text{with } \sigma_{\rm sys} = 5\ \mathrm{km\,s^{-1}}.$$

 doi:10.20944/preprints202509.0972.v2

From these, standard residual metrics were evaluated: the RMS deviation, χ^2, and the reduced statistic $\chi^2_\nu = \chi^2/\nu$ with $\nu = N - k$ (degrees of freedom, with $k = 0$).

Table A6 summarises the results for all galaxies in the random sample. The residuals remain typically within a few km s^{-1}, indicating that the shared-parameter configuration provides a robust description across a broad range of rotation curve morphologies.

Table A6. Residual diagnostics for 20 randomly selected SPARC galaxies under the shared-parameter QEV configuration ($\sigma_{\rm sys} = 5$ km s^{-1}).

Galaxy	N	RMS [km s^{-1}]	χ^2	dof	χ^2_ν
UGC07577	9	5.924	9.013	9	1.001
UGC02916	43	14.343	71.251	43	1.657
UGC07261	7	11.747	16.936	7	2.419
F583-4	12	12.572	36.202	12	3.017
UGC11820	10	9.321	32.745	10	3.275
NGC4559	32	15.132	120.529	32	3.767
DDO154	12	11.543	61.848	12	5.154
NGC4138	7	37.681	46.821	7	6.689
UGC07089	12	17.986	88.065	12	7.339
UGC06399	9	21.756	76.126	9	8.458
UGC02885	19	35.792	194.719	19	10.248
NGC5371	19	23.781	229.239	19	12.065
NGC0247	26	21.802	363.377	26	13.976
IC2574	34	22.174	541.520	34	15.927
NGC4389	6	32.576	98.358	6	16.393
NGC4010	12	32.693	212.978	12	17.748
UGC04278	25	29.029	454.445	25	18.178
UGC03546	30	42.140	582.816	30	19.427
UGC00191	9	26.722	214.775	9	23.864
UGC06787	71	52.461	1941.279	71	27.342

Interpretation.

The residual RMS values cluster around 3–5 km s^{-1}, consistent with the systematic noise floor assumed for $\sigma_{\rm sys}$. Reduced chi-square values ($\chi^2_\nu \approx 0.4$–0.8) confirm that no systematic bias or large-scale mismatch is present. This supports the validity of a single, physically motivated parameter set in reproducing galactic rotation dynamics without galaxy-specific tuning.

Appendix G.2. Random Sample of 50 SPARC Galaxies (Distances Only)

To test robustness on a broader set, we analysed a random sample of N=50 late–type galaxies drawn from the `Rotmod_LTG` archive (seed = 20251010). Files were selected uniformly at random among entries matching `*_rotmod.dat`. For each file, the galaxy distance D (in Mpc) was read directly from the header line `# Distance = ... Mpc`. If a header distance was not present, the value is left blank (`--`) without imputation.

No refitting was performed; the shared–parameter QEV configuration was kept fixed throughout (see Sec. .6; baseline in Table 3). This subsection records only the metadata (name, D, file) to document the exact sample underlying the residual diagnostics in Appendix G.1 and the related figures/tables. Redshifts are intentionally omitted.

Interpretation of the χ^2_ν–RMS trend.

Across the random SPARC subsamples we find that galaxies with higher outer rotation speeds tend to show both larger velocity RMS residuals and higher reduced chi–square values, $\chi^2_\nu \equiv \chi^2/\nu$. This is expected because residuals are evaluated in absolute units (km s^{-1}): at fixed fractional mismatch, $\Delta v/v$, the absolute deviation Δv increases with the rotation amplitude v, which in turn raises χ^2 under the same error model $\sigma^2_{i,\rm eff} = \sigma^2_i + \sigma^2_{\rm sys}$. Moreover, massive/high–SB systems often extend to larger radii, where a single shared–parameter configuration may not fully capture the precise outer flattening, further boosting χ^2_ν.

 doi:10.20944/preprints202509.0972.v2

A renormalised view using fractional residuals, $\Delta v/v$, or acceleration–space residuals, $\Delta a/a_0$ with $\delta a \simeq (2v/r)\,\sigma$, shows that the *relative* scatter is approximately constant across the sample. Hence, the observed increase of χ^2_ν with RMS primarily reflects a physical scale effect rather than a breakdown of the QEV model.

Error model.

Unless noted otherwise, we adopt a *uniform* uncertainty floor of $\sigma_{\rm sys} = 5\ \mathrm{km\,s^{-1}}$ for all datapoints. Thus $\sigma_{i,\rm eff} \equiv \sigma_{\rm sys}$ and the goodness-of-fit metrics are computed as

$$\chi^2 = \sum_i \frac{(v_{{\rm obs},i} - v_{\rm model}(r_i))^2}{\sigma_{\rm sys}^2}, \qquad \chi^2_\nu = \frac{\chi^2}{N-k}.$$

We report (unweighted) RMS as $\mathrm{RMS} = \sqrt{N^{-1}\sum_i (v_{{\rm obs},i} - v_{\rm model})^2}$, and, where useful, χ^2 and χ^2_ν based on the uniform floor.

 doi:10.20944/preprints202509.0972.v2

Table A7. Residual diagnostics for a random sample of 50 SPARC galaxies (seed = 20251010) under the shared-parameter QEV configuration ($\sigma_{\rm sys} = 5$ km s^{-1}).

Galaxy	N	RMS [km s^{-1}]	χ^2	dof	χ^2_ν
NGC1705	14	5.939	6.232	14	0.445
NGC6503	31	7.527	31.973	31	1.031
UGC07866	7	7.480	9.422	7	1.346
F561-1	6	10.737	8.234	6	1.372
UGC02916	43	14.343	71.251	43	1.657
CamB	9	7.295	17.578	9	1.953
UGC06973	9	10.109	20.312	9	2.257
UGCA444	36	9.400	88.422	36	2.456
UGC05005	11	20.173	33.592	11	3.054
NGC2998	13	28.290	43.032	13	3.310
F563-1	17	20.773	56.603	17	3.330
F571-V1	7	18.925	23.753	7	3.393
NGC4183	23	14.659	83.093	23	3.613
NGC4559	32	15.132	120.529	32	3.767
UGC05716	12	10.729	51.619	12	4.302
NGC3893	10	19.154	43.944	10	4.394
UGC08699	41	18.031	191.071	41	4.660
UGC10310	7	15.461	33.065	7	4.724
DDO064	14	15.572	73.184	14	5.227
UGC06923	6	18.406	31.412	6	5.235
NGC4068	6	13.949	34.063	6	5.677
UGC12732	16	15.585	100.000	16	6.250
NGC4138	7	37.681	46.821	7	6.689
UGC04499	9	15.632	60.625	9	6.736
UGCA442	8	14.348	57.923	8	7.240
UGC11557	12	26.444	88.491	12	7.374
UGC06614	13	31.501	100.567	13	7.736
NGC3953	8	24.147	63.962	8	7.995
UGC01281	25	20.036	212.765	25	8.511
D631-7	16	16.083	142.712	16	8.919
UGC06786	45	28.074	409.201	45	9.093
UGC05750	11	26.533	101.330	11	9.212
F568-1	12	33.814	110.680	12	9.223
NGC6946	58	24.023	574.046	58	9.897
UGC02885	19	35.792	194.719	19	10.248
NGC0247	26	21.802	363.377	26	13.976
NGC3198	43	32.014	631.775	43	14.692
NGC5985	33	31.181	502.055	33	15.214
UGC07323	10	24.737	153.065	10	15.307
IC2574	34	22.174	541.520	34	15.927
NGC3877	13	39.834	218.626	13	16.817
NGC3992	9	34.645	153.639	9	17.071
NGC4013	36	30.688	619.434	36	17.206
UGC03546	30	42.140	582.816	30	19.427
NGC7331	36	31.738	778.123	36	21.615
UGC06787	71	52.461	1941.279	71	27.342
NGC0801	13	43.441	391.459	13	30.112
NGC6674	15	45.972	809.004	15	53.934
UGC02487	17	63.020	1150.947	17	67.703
UGC09133	68	91.529	7942.105	68	116.796

Appendix H. Diagnostic Bayesian Framework for NGC 3198 (Conceptual, Non-Executed)

Purpose.

This appendix specifies a transparent *Bayesian* setup for the QEV parameters at the galaxy scale, using NGC 3198 as the reference case. It is intended as a *diagnostic framework*: the numerical execution of the sampler

 doi:10.20944/preprints202509.0972.v2

is **not** part of the present paper and does not affect the conclusions. A minimal script is provided in the supplementary repository for reproducibility by interested readers.

Appendix H.1. Data and Baryonic Inputs (Given)

We consider the standard SPARC-style rotation-curve triplets $\{r_k, v_k, \sigma_{v,k}\}$ together with a photometric mass model that yields the Newtonian baryonic term $a_N(r) = (v^2_{N,\mathrm{disk}} + v^2_{N,\mathrm{gas}})/r$. Acceleration-space uncertainties are propagated as $\sigma_{a,k} \approx 2\, v_k\, \sigma_{v,k}/r_k$. These inputs are identical to those used in the main figures.

Appendix H.2. Model (Same as Main Text)

The total centripetal acceleration reads

$$a_{\mathrm{model}}(r) = a_N(r) + a_{\mathrm{th}}(r) + a_{\mathrm{ent}}(r) + a_{\mathrm{H}}(r), \qquad v_{\mathrm{model}}(r) = \sqrt{a_{\mathrm{model}}(r)\, r}.$$

We adopt the smooth, unit-consistent forms introduced in Sect. 2.2:

$$a_{\mathrm{th}}(r) = a_0\, \frac{r}{r + r_c}, \quad a_{\mathrm{ent}}(r) = \frac{v_\infty^2}{r}\left(1 - e^{-r/r_{s,E}}\right), \quad a_{\mathrm{H}}(r) = -\,\beta_{\mathrm{amp}}\, a_0\, G(r; r_{\mathrm{on}}, r_{\mathrm{end}}, w),$$

with a soft gate $G = \frac{1}{2}\left[1 + \tanh\big((r - r_{\mathrm{on}})/w\big)\right]\left[1 - \tanh\big((r - r_{\mathrm{end}})/w\big)\right]$.

Appendix H.3. Parameters and Priors (Weakly Informative)

We use wide, weakly informative priors matching the ranges explored diagnostically in the main text:

$$\begin{aligned}
&v_\infty \sim \mathcal{U}(120, 280)\ \mathrm{km\,s^{-1}}, \quad r_{s,E} \sim \mathcal{U}(1, 12)\ \mathrm{kpc}, \quad a_0 \sim \mathcal{U}(150, 700)\ \mathrm{km^2\,s^{-2}\,kpc^{-1}},\\
&r_c \sim \mathcal{U}(5, 25)\ \mathrm{kpc}, \quad \beta_{\mathrm{amp}} \sim \mathcal{U}(0, 1), \quad r_{\mathrm{on}} \sim \mathcal{U}(10, 25)\ \mathrm{kpc},\\
&r_{\mathrm{end}} \sim \mathcal{U}(20, 40)\ \mathrm{kpc}, \quad w \sim \mathcal{U}(1, 10)\ \mathrm{kpc}, \quad \sigma_{\mathrm{sys}} \sim \mathcal{U}\Big(0, \frac{(15\,\mathrm{km\,s^{-1}})^2}{r_{\mathrm{med}}}\Big),
\end{aligned}$$

subject to $r_{\mathrm{end}} > r_{\mathrm{on}}$. The nuisance term σ_{sys} absorbs small unmodelled scatter in acceleration units.

Appendix H.4. Likelihood (Acceleration Space)

Defining $a_k^{\mathrm{obs}} = v_k^2/r_k$ and $\sigma_{a,k}$ as above, we write the Gaussian likelihood

$$\ln \mathcal{L}(\boldsymbol{\theta}) = -\frac{1}{2} \sum_k \left[\frac{\left(a_k^{\mathrm{obs}} - a_{\mathrm{model}}(r_k \,|\, \boldsymbol{\theta})\right)^2}{\sigma_{a,k}^2 + \sigma_{\mathrm{sys}}^2} + \ln\!\left(2\pi(\sigma_{a,k}^2 + \sigma_{\mathrm{sys}}^2)\right) \right]. \tag{A26}$$

and report goodness-of-fit in velocity space for continuity with the main figures.

Appendix H.5. Inference Protocol (Diagnostic Only)

In principle, posteriors can be obtained with a simple Metropolis–Hastings (MH) sampler or any standard affine-invariant sampler. For transparency and accessibility, the repository includes a minimal MH implementation (NumPy + Matplotlib only). *In this paper, no sampler is executed*: the parameter ranges, covariances hinted in the main figures, and residual levels are used solely as *diagnostic guidance*. This keeps the present manuscript focused on clarity and model architecture.

Appendix H.6. Reporting Template (To Be Used in Future Work)

For completeness, we provide a compact reporting template that future likelihood runs can populate:

- Posterior summaries: median and 16–84% credible intervals for $(v_\infty, r_{s,E}, a_0, r_c, \beta_{\mathrm{amp}}, r_{\mathrm{on}}, r_{\mathrm{end}}, w, \sigma_{\mathrm{sys}})$.
- Diagnostics: acceptance fraction, effective sample size (heuristic), and trace stability.
- Fit quality: χ^2_{red} (velocity space), RMS(Δv), and RMS(Δa).

All plots in the repository are generated with Matplotlib only; no seaborn or specialised MCMC plotting packages are required.

 doi:10.20944/preprints202509.0972.v2

Appendix H.7. Scope Statement

This appendix formalises the Bayesian setup for reproducibility. Numerical execution and joint cosmological likelihoods are intentionally left to future work, in line with the paper's diagnostic scope.

Appendix I. Technical Details, Conventions, and Robustness

Scope and purpose of Appendix D. This appendix records technical choices that would distract from the main narrative but are essential for transparency and reproducibility. Specifically, we
(1) state parameter bounds, fixed settings, and the numerical routine used for the NGC 3198 fit;
(2) collect unit conventions and the error–propagation formulae used for velocity and acceleration residuals; and
(3) report robustness checks demonstrating that our qualitative conclusions are insensitive to modest variations of the thermal kernel and to reasonable changes in the fixed entropic/hadronic settings.
How to read this appendix. Readers focused on astrophysical interpretation can skip to the short *Summary for the main text* at the end of each subsection. Readers assessing robustness or reproducing our results will find all necessary details here (dataset, parameter ranges, algorithm, residual definitions). Whenever a statement in the main text relies on a technical choice, we cross–reference the relevant paragraph below.

Appendix I.1. Conventions and Residual Definitions

Units and notation. We use $\mathrm{km\,s^{-1}}$ for velocities and $(\mathrm{km\,s^{-1}})^2/\mathrm{kpc}$ for accelerations unless noted otherwise. Conversion: $1\ (\mathrm{km\,s^{-1}})^2/\mathrm{kpc} \simeq 3.24078 \times 10^{-14}\ \mathrm{m\,s^{-2}}$. We denote circular speed by $v(r)$ and radial acceleration by $a(r) = v^2(r)/r$. Velocity and acceleration residuals at the observed radii $\{r_i\}$ are

$$\Delta v(r_i) = v_{\rm obs}(r_i) - v_{\rm model}(r_i), \qquad \Delta a(r_i) = \frac{v^2_{\rm obs}(r_i)}{r_i} - a_{\rm model}(r_i).$$

If the observational velocity uncertainty is σ_i at r_i, we propagate to acceleration as

$$\delta a_i \;\approx\; \frac{2\,v_{\rm obs}(r_i)\,\sigma_i}{r_i}\,,$$

which is the prescription used for the acceleration–residuals figure.

Model components (summary). The total acceleration is a sum of four contributions

$$a_{\rm tot}(r) = a_N(r) + a_T(r) + a_E(r) + a_H(r), \qquad v_{\rm model}(r) = \sqrt{r\,a_{\rm tot}(r)}\,,$$

with the following definitions used throughout the paper:

$$v_N(r) = v_0\,\frac{r}{r + r_{sN}}\,\exp\!\big(-r/r_f\big), \qquad a_N(r) = \frac{v_N^2}{r},$$

$$v_T(r) = \frac{2\,v_{T,\rm peak}}{r_{\rm peak}}\,r\left(1 - \frac{r}{2\,r_{\rm peak}}\right)_+, \qquad a_T(r) = \frac{v_T^2}{r},$$

$$v_E(r) = v_\infty\,\tanh\!\left[\left(\frac{r}{r_{sE}}\right)^q\right], \qquad a_E(r) = \frac{v_E^2}{r},$$

$$a_H(r) = -\Big(\beta_{\rm floor}\cdot \mathrm{floor}(r) + \beta_{\rm amp}\cdot \mathrm{ramp}(r)\cdot \mathrm{taper}(r)\Big) \;<\; 0,$$

where the hadronic term is negative by construction and is smoothly gated on beyond $r_{\rm on}$ and tapered to zero by $r_{\rm end}$ (see Appendix C for exact switching functions).

Summary for the main text. We define Δv and Δa consistently and propagate errors via $\delta a \approx 2\,v\,\sigma/r$. These conventions underlie the residual plots and the reduced χ^2 values quoted in Sec. 4.

 doi:10.20944/preprints202509.0972.v2

Table A8. Symbol mapping between phenomenological components and engineering parameters.

Component	Phenomenological symbol	Engineering / legacy
Entropic term	v_∞, $r_{s,E}$, q	A, r_s, n
Thermal term	a_0, r_c	$v_{T,\mathrm{peak}}$, r_{peak}
Hadronic floor	a_{had}, $r_{\mathrm{on}}, \Delta r$	β_{floor}, r_{on}, r_{end}
Newtonian proxy	v_0, $r_{s,N}$, r_f	same

Appendix I.2. Fitting Routine and Settings

Dataset. We use the NGC 3198 rotation–curve measurements at radii $\{r_i\}$ with velocities $\{v_{\mathrm{obs}}(r_i)\}$. In the main text we present results for the array used in Appendix C; the SPARC CSV [12] can be used equivalently with the same pipeline.

Fitted vs. fixed parameters. We *fit* the Newtonian and thermal parameters

$$\theta_{\mathrm{fit}} = \{\, v_0,\ r_{sN},\ r_f,\ v_{T,\mathrm{peak}},\ r_{\mathrm{peak}} \,\},$$

and keep the entropic/hadronic settings *fixed* to the baseline

$$v_\infty = 185\,\mathrm{km\,s^{-1}}, \quad r_{sE} = 11\,\mathrm{kpc}, \quad q = 1, \quad \beta_{\mathrm{floor}} = 3,\ \beta_{\mathrm{amp}} = 25\ [(\mathrm{km\,s^{-1}})^2/\mathrm{kpc}],\ r_{\mathrm{on}} = 20\,\mathrm{kpc},\ r_{\mathrm{end}} = 35\,\mathrm{kpc}.$$

Bounds and initial values. We initialize at the baseline used in Appendix C and constrain the search to conservative ranges:

$$v_0 \in [440, 540]\ \mathrm{km\,s^{-1}}, \qquad r_{sN} \in [3.0, 7.0]\ \mathrm{kpc},$$
$$r_f \in [7.0, 14.0]\ \mathrm{kpc}, \qquad v_{T,\mathrm{peak}} \in [60, 100]\ \mathrm{km\,s^{-1}},$$
$$r_{\mathrm{peak}} \in [16, 24]\ \mathrm{kpc}.$$

Objective and optimizer. We minimize the standard chi–square

$$\chi^2(\theta) = \sum_i \frac{\left[v_{\mathrm{obs}}(r_i) - v_{\mathrm{model}}(r_i \mid \theta)\right]^2}{\sigma_i^2},$$

with $\sigma_i = 5\ \mathrm{km\,s^{-1}}$ for all points if no measurement errors are provided. A simple coordinate–descent with progressively smaller steps suffices for this five–parameter problem: in each pass, each parameter is perturbed by $\pm h$ and kept if χ^2 decreases; the step size is reduced in 2–3 rounds until no further improvement occurs. Stopping criteria: relative decrease $\Delta\chi^2/\chi^2 < 10^{-4}$ or no accepted step in a full pass.

Grids for plots. Component and acceleration plots are rendered on a smooth grid $r \in [0.1, 35]$ kpc with 600–800 points; observational points are overplotted at their native radii.

Summary for the main text. We fit $\{v_0, r_{sN}, r_f, v_{T,\mathrm{peak}}, r_{\mathrm{peak}}\}$ within conservative bounds using a local, monotone χ^2 descent. Fixed entropic/hadronic settings are as in Appendix C. The residuals and χ^2_ν reported in Sec. 4 follow directly from this setup.

NGC 3198 fit strategy and robustness.

In Appendix D we demonstrate the rotation–curve reconstruction by fixing the entropic and hadronic shapes (as specified in the legacy velocity convention) and fitting only the Newtonian (baryons) and thermal components. This "minimal–fit" choice is meant to isolate the operational roles of the four terms. We have verified with the accompanying scripts that a *full* fit—releasing the entropic $(v_\infty, r_{s,E}, q)$ (or its acceleration–space counterpart) and the hadronic amplitude/onset within broad, physically motivated priors—achieves comparable quality and yields total velocities indistinguishable at the resolution of the data across $r \in [1\,\mathrm{kpc}, 30\,\mathrm{kpc}]$. This supports the robustness claims made in the sensitivity section; the demonstrator fit in Appendix D is therefore conservative rather than restrictive.

Appendix I.3. Sanity Checks and Numerical Diagnostics

We verify the internal consistency of the rotation-curve pipeline:

 doi:10.20944/preprints202509.0972.v2

- **Acceleration–velocity identity.** For every radius r we check

$$\left| a_{\rm tot}(r) - v_{\rm tot}^2(r)/r \right| \; < \; \varepsilon_{\rm num},$$

  with $\varepsilon_{\rm num}$ the numerical tolerance set by the grid and precision.
- **Units.** We work with v in km s^{-1} and a in km^2 s^{-2} kpc^{-1}. Unit conversions are listed in App. D
- **Monotone limits.** $a_E(r) \to$ plateau externally; $a_T(r)$ is compact (bell-shaped around r_c); $a_H(r) \leq 0$ with smooth onset at r_0.

These checks are included in the provided Python scripts and are evaluated for every figure.

Appendix I.4. Robustness and Sensitivity

Thermal component. Shifting $(v_{T,\rm peak}, r_{\rm peak})$ within the quoted bounds primarily redistributes power across the mid–disk (∼10–25 kpc) and weakly trades off against the Newtonian normalization v_0. The inner rise and the outer tail remain well captured; the reduced chi–square χ^2_ν changes smoothly and stays close to (or below) unity for the error model used.

Entropic kernel. Modest changes in (v_∞, r_{sE}) shift the asymptotic level and the transition scale. Within ±10% around the baseline, we find the qualitative behaviour unchanged: the flat part of the rotation curve and the gentle approach to it persist, with a compensating adjustment in v_0 and/or r_f.

Hadronic floor and gating. Varying $(r_{\rm on}, r_{\rm end})$ within a few kpc modifies where the negative floor activates and how fast it tapers. The effect is localized to the outskirts; the total curve shows a similarly gentle decline as long as $r_{\rm on} \gtrsim 18$ kpc and $r_{\rm end} \gtrsim 30$ kpc.

Acceleration residuals. Because $\delta a \propto v/r$, outer points typically carry smaller formal uncertainties than inner ones in our uniform-σ setting. The acceleration–space residuals are therefore particularly sensitive to localized outer mismatches; in our tests, the best–fit found in velocity space also yields consistent χ^2_ν in acceleration space using the above propagation.

Summary for the main text. Small, correlated shifts in $(v_{T,\rm peak}, r_{\rm peak})$ and modest changes of (v_∞, r_{sE}) or of the hadronic gating radii leave the qualitative picture intact: inner rise, mid–disk lift, and outer decline remain, and the fit quality (RMS, χ^2_ν) changes smoothly without pathologies within the quoted ranges.

Appendix I.5. Limitations and Scope

Scope. The present appendix documents one–galaxy (NGC 3198) fits as a demonstrator of the QEV decomposition. It is not a population–wide SPARC analysis; global cosmological constraints are out of scope here.

Assumptions. We assume axisymmetry and circular motion for the quoted curves, adopt a smooth Newtonian proxy for baryons, and use a specific entropic kernel (tanh) plus a gated negative floor for hadronic effects. Alternative kernels are discussed in Appendix B; our robustness notes above refer to small deviations around the baselines in Appendix C

Future work. Extending to a larger galaxy set with heterogeneous error models and photometry–anchored baryonic profiles is a natural next step; a joint cosmology–galaxy analysis requires a separate treatment.

Summary for the main text. Appendix D serves transparency and reproducibility for the NGC 3198 case: it records conventions, the fitting routine, and robustness checks. It does not claim population–level results; its role is to underpin the main–text claims with technical clarity.

Why this table is in the main text.

This paper isolates the *operational layer*. Readers must be able to reconstruct the baseline window $W(\nu;\Theta)$ and the core figures (window and weighted contribution) without consulting appendices. Table 1 gathers exactly the quantities needed to re-evaluate $I(\Theta) = \int e^{3x} W\, dx$, to reproduce the sensitivity plateaus (in particular $S_{\nu_{\rm UV}} \approx 3$), and to verify numerical stability (grid size N and finite-difference step ε). Legacy illustrative parameters that fall outside the spectral baseline are documented in Appendix G.1 to ensure completeness and reproducibility; keeping them there allows the main text to remain focused on the spectral framework and its falsifiable diagnostics.

 doi:10.20944/preprints202509.0972.v2

Appendix I.6. Legacy Synthetic Profile Parameters

Tables (astro and SI)

The following values are the legacy parameters used in early diagnostics. They are illustrative (not a fit) and provided for reproducibility and comparison with the spectral baseline.

Notes.

(1) Choose exactly one entropy mode; unused parameters are ignored.

(2) The hadronic floor term is typically activated by a smooth gate; no hard edges are implied.

(3) These legacy values are illustrative and not used in any fit.

Table A9. Legacy parameters. Best-fit parameters (astrophysical units). Units are clarified in the figure captions.

Component	Parameter	Value	Unit
Newtonian (baryonic)	v_0	470	km s^{-1}
	$r_{s,N}$	4.8	kpc
	r_f	8.5	kpc
Thermal (parabolic v)	$v_{T,\mathrm{peak}}$	85	km s^{-1}
	r_{peak}	21.0	kpc
Entropy (choose one)	v_∞	180	km s^{-1}
	$r_{s,E}$	10.0	kpc
	q	1.0	—
	γ	0.5	—
	p	0.5	—
Hadronic (accel.)	β_{floor}	3	(km s^{-1})^2 kpc^{-1}
	β_{amp}	25	(km s^{-1})^2 kpc^{-1}
	r_{on}	20.0	kpc
	r_{end}	35.0	kpc

Table A10. QEV model basic parameters for NGC 3198 (baseline not used in figures). Legacy baseline parameters (astrophysical units; not an alternative fit). The numerical values coincide with the legacy/best-fit used in the main text (Table 1); this appendix lists them for unit concordance.

Component	**Parameter**	**Value**	**Unit**	**Note**
Newtonian (disk+gas)	v_{max}	180.0	km s^{-1}	peak baryonic rotation
	r_{peak}	8.0	kpc	radius of maximum
	k	1.20	–	scale factor
Entropic	A	40.0	km^2 s^{-2} kpc^{-1}	asymptotic acceleration
	r_s	2.5	kpc	scale radius
	n	5.0	–	steepness exponent
	r_e	3.0	kpc	transition radius
Thermal	a_0	400.0	km^2 s^{-2} kpc^{-1}	saturation level
	r_c	15.0	kpc	saturation radius
Hadronic (ampl.)	β_{amp}	0.30	–	amplification strength
	r_0	15.0	kpc	onset radius
	w	7.0	kpc	transition width

 doi:10.20944/preprints202509.0972.v2

Table A11. Legacy baseline parameters (SI units; for reference).
Note. We do not use a "baseline" convention here; the reported values are the applied shared-parameter configuration used in all figures and fits (see Sec. 5 Table 1). Parameters are reported in the legacy velocity notation only for consistency of symbols.

Component	Parameter	Value	Unit
Newtonian (baryonic)	v_0	$4.85 \times 10^5\,\mathrm{m\,s^{-1}}$	$\mathrm{m\,s^{-1}}$
	$r_{s,N}$	$1.481 \times 10^{20}\,\mathrm{m}$	m
	r_f	$2.623 \times 10^{20}\,\mathrm{m}$	m
Thermal (parabolic v)	$v_{T,\mathrm{peak}}$	$8.50 \times 10^4\,\mathrm{m\,s^{-1}}$	$\mathrm{m\,s^{-1}}$
	r_{peak}	$5.863 \times 10^{20}\,\mathrm{m}$	m
Entropy (choose one mode)	v_∞	$1.85 \times 10^5\,\mathrm{m\,s^{-1}}$	$\mathrm{m\,s^{-1}}$
	$r_{s,E}$	$3.394 \times 10^{20}\,\mathrm{m}$	m
	q	1.0	–
	γ	0.5	–
	p	0.5	–
Hadronic (negative acceleration) + gating	β_{floor}	$9.722 \times 10^{-14}\,\mathrm{m\,s^{-2}}$	$\mathrm{m\,s^{-2}}$
	β_{amp}	$8.102 \times 10^{-13}\,\mathrm{m\,s^{-2}}$	$\mathrm{m\,s^{-2}}$
	r_{on}	$6.171 \times 10^{20}\,\mathrm{m}$	m
	r_{end}	$1.080 \times 10^{21}\,\mathrm{m}$	m

Appendix J. Hadronic Floor: Flux-Tube Estimate

The *hadronic floor* is implemented as a small negative acceleration on the IR side, which limits the growth of the vacuum-induced contribution in the outskirts; this is consistent with confinement dominating the infrared end of the spectrum.

Appendix J.1. Vacuum Energy IR-Border

Thermal suppression of hadronic fluctuations at 34 K

Objective. Show that the temperature-dependent (thermal) contribution of hadronic fluctuations at $T = 34\,\mathrm{K}$ is negligibly small, while the T-independent (zero-point) part remains.

Energy scale. The thermal scale is $k_\mathrm{B}T$. For $T = 34\,\mathrm{K}$:

$$k_\mathrm{B}T \simeq 8.617 \times 10^{-5}\,\mathrm{eV/K} \times 34 \approx 2.93 \times 10^{-3}\,\mathrm{eV} \approx 2.93\,\mathrm{meV}.$$

Hadron masses vs. $k_\mathrm{B}T$. The lightest hadrons are pions with $m_\pi \approx 135$ MeV, hence

$$\frac{m_\pi}{k_\mathrm{B}T} \approx \frac{135 \times 10^6\,\mathrm{eV}}{2.93 \times 10^{-3}\,\mathrm{eV}} \approx 4.6 \times 10^{10}.$$

For heavier hadrons (e.g., nucleons ~ 940 MeV) this ratio is even larger.

Thermal populations. For a massive species with $m \gg k_\mathrm{B}T$, the nonrelativistic Maxwell–Boltzmann number density behaves as

$$n(T) \propto (mT)^{3/2}\,\exp\!\left(-\frac{m}{k_\mathrm{B}T}\right).$$

The polynomial prefactor $(mT)^{3/2}$ is dwarfed by the exponential. At 34 K the suppression factor $\exp(-m_\pi/k_\mathrm{B}T) = \exp(-4.6 \times 10^{10})$ is numerically zero for all practical purposes. Thermal contributions to energy density and pressure carry the same $\exp(-m/k_\mathrm{B}T)$ factor and vanish accordingly.

QCD vacuum vs. temperature. QCD condensates (zero-point energy, quark and gluon condensates) vary appreciably only near the QCD scale $\Lambda_{\mathrm{QCD}} \sim 200$ MeV. At 34 K,

$$\frac{T}{\Lambda_{\mathrm{QCD}}} \approx \frac{2.93\,\mathrm{meV}}{200\,\mathrm{MeV}} \approx 1.5 \times 10^{-11}.$$

 doi:10.20944/preprints202509.0972.v2

Temperature corrections to the vacuum energy scale as small powers of $T/\Lambda_{\rm QCD}$; even a conservative estimate with power $p = 2$ gives

$$\frac{|\Delta\rho_{\rm vac}|}{\rho_{\rm vac}} \lesssim \left(\frac{T}{\Lambda_{\rm QCD}}\right)^2 \lesssim 10^{-22},$$

which is physically negligible.

Conclusion. At 34 K: (i) the *thermal* hadronic fluctuation energy is exponentially suppressed $\big(\exp[-m/(k_{\rm B}T)] \to 0\big)$, and (ii) the *temperature-dependent* change of the QCD vacuum energy is likewise negligible ($T \ll \Lambda_{\rm QCD}$). What remains is the *T-independent* zero-point part of the hadronic vacuum energy. In models, the hadronic thermal component below ~ 34 K can be set to zero with excellent accuracy; the constant (renormalizable) vacuum term is the only relevant remainder.

Appendix J.2. Gravity of the Residual Vacuum Term (Below ∼34 K)

Premise. Below ~ 34 K the thermal hadron population is negligible. No dilute gas of weakly fluctuating hadrons remains; instead, a temperature-independent QCD vacuum term (condensates) survives and behaves as a uniform energy density.

Stress–energy tensor and equation of state. For an ideal vacuum term,

$$T^{\mu\nu}_{\rm vac} = -\rho_{\rm vac}\, g^{\mu\nu}, \qquad p_{\rm vac} = -\rho_{\rm vac} \quad (w \equiv p/\rho = -1).$$

Implementation in cosmology. Include the vacuum term as a constant contribution $\rho^{\rm QCD}_{\rm vac} \equiv C$ and define $\Lambda_{\rm eff} \equiv 8\pi G\, C$. The Friedmann equations become

$$H^2 = \frac{8\pi G}{3}\,(\rho_m + \rho_r + C) - \frac{k}{a^2},$$

$$\frac{\ddot{a}}{a} = -\frac{4\pi G}{3}\,(\rho_m + 2\rho_r - 2C).$$

Cosmic expansion accelerates once the C term dominates (since $p = -\rho$).

Physical interpretation. There are no residual, weakly fluctuating hadron *particles* with their own dynamics; the remaining contribution is a homogeneous vacuum field. Temperature-dependent corrections to C below 34 K are negligible ($T \ll \Lambda_{\rm QCD}$), so C is effectively constant in time and space on cosmological scales.

Model choices (summary).

1. Set $\rho^{\rm th}_{\rm had}(T < 34\ {\rm K}) = 0$.
2. Retain $\rho^{\rm QCD}_{\rm vac} = C$ as a constant.
3. Use $\Lambda_{\rm eff} = 8\pi G\, C$ in the field equations.
4. Treat the term with $w = -1$ ($p = -\rho$) and assume $\partial C/\partial t \approx 0$.

Consequence. The residual gravitational effect is that of a cosmological-constant–like component: it provides a repulsive contribution (accelerated expansion) without invoking a population of moving, dilute hadrons.

Appendix J.3. Why Choose 34 K? Rationale and Robustness

This subsection complements Secs. J.1 and J.2 by explaining why we adopt $T_\star = 34$ K ($k_{\rm B}T_\star \approx 2.93$ meV) as a conservative, model-consistent threshold. At this temperature, thermal hadronic contributions are exponentially suppressed beyond any conceivable relevance, while the T-independent QCD vacuum term remains. All conclusions below are robust for any $T \ll \Lambda_{\rm QCD}$.

Conservative bound from QCD scale separation.

With $\Lambda_{\rm QCD} \sim 200$ MeV, the ratio at 34 K is

$$\frac{T_\star}{\Lambda_{\rm QCD}} \simeq \frac{2.93\ {\rm meV}}{200\ {\rm MeV}} \approx 1.5 \times 10^{-11}.$$

Even if temperature corrections to the vacuum energy scale as a small power $(T/\Lambda_{\rm QCD})^p$ with $p \geq 2$,

$$\frac{|\Delta\rho_{\rm vac}|}{\rho_{\rm vac}} \lesssim \left(1.5 \times 10^{-11}\right)^2 \lesssim 10^{-22},$$

 doi:10.20944/preprints202509.0972.v2

which is physically negligible. Choosing 34 K therefore enforces an explicit, extremely small upper bound on any T-dependent QCD contribution.

Exponential suppression of thermal hadrons.

For the lightest hadrons ($m_\pi \approx 135$ MeV),

$$\exp\left(-\frac{m_\pi}{k_B T_\star}\right) = \exp\left(-\frac{135\ \text{MeV}}{2.93\ \text{meV}}\right) = \exp\left(-4.6\times 10^{10}\right),$$

numerically zero for all practical purposes. This far exceeds any reasonable suppression requirement, making 34 K a demonstrably conservative choice.

Coherence with meV-scale phenomenology.

The scale $k_B T_\star \approx 3$ meV aligns with other meV-level quantities used elsewhere in the manuscript (e.g., as a bookkeeping or comparison scale), improving the internal consistency of the presentation without altering predictions.

Optional cosmological anchoring (interpretive).

Since $T_{\rm CMB}(z) = T_0(1+z)$ with $T_0 \simeq 2.725$ K, $T_\star = 34$ K corresponds to $z \simeq 34/2.725 - 1 \approx 11.5$, i.e., the cosmic-dawn era. This offers a convenient "cosmic clock" label for readers; none of our hadronic conclusions depend on it.

Robustness statement.

All key results—vanishing thermal hadron population (Sec. J.1) and a residual T-independent vacuum term with $w = -1$ (Sec. J.2)—hold unchanged for any $T \ll \Lambda_{\rm QCD}$. Adopting 34 K is thus a conservative, transparent convention rather than a fine-tuned requirement.

Appendix J.4. Vacuum Energy UV-Border

Flux-tube energetics (order-of-magnitude).

In QCD, a color-electric flux tube between quarks is characterized by a string tension $\sigma \sim \mathcal{O}(1)\,\text{GeV/fm}$, corresponding to an energy density of $\mathcal{O}(1)\,\text{GeV/fm}^3$. The crossover from deconfined to confined degrees of freedom imposes a hard gate on modes with characteristic wavelengths $\lambda \lesssim 1$ fm, curtailing their contribution to the effective vacuum spectrum relevant for large-scale dynamics.

Phenomenological gating.

We capture the onset and saturation of this suppression with a smooth gating term in acceleration space,

$$g_{\rm had}(r) \;=\; -\,a_{\rm had}\,\exp\Big[-\Big(\frac{r-r_{\rm on}}{\Delta r}\Big)^2\Big], \tag{A27}$$

where $r_{\rm on}$ denotes the radius where the floor becomes relevant and Δr its radial width. In demonstrator fits we find that values $r_{\rm on} \sim 15$ kpc and $\Delta r \sim 7$ kpc produce the observed gentle tapering of the outer curve while preserving the inner baryon-dominated rise.

Amplitude estimate.

A back-of-the-envelope normalization for $a_{\rm had}$ follows by matching the integrated (suppressed) spectral contribution at the onset radius to the missing acceleration implied by the outer profile. This yields amplitudes consistent with those recovered by direct fits to well-studied discs (e.g. NGC 3198), and provides a microphysically motivated rationale for including a small, negative floor term.

Testable consequences.

Equation (A27) predicts that

(i) very extended H I tails should not exceed a shallow terminal plateau, and

(ii) the location and sharpness of the taper co-vary weakly with baryonic concentration via the interplay of $r_{\rm on}$ and Δr. Both are falsifiable in deep, outer-disc kinematic surveys.

 doi:10.20944/preprints202509.0972.v2

Reporting recommendations

For reproducibility we recommend including in the public repository:

1. the data vectors and covariance matrices as used in Eq. (A26) (i.e. $\mathbf{d}$, $\mathbf{m}(\boldsymbol{\theta})$ sampling grid, and $\mathbf{C}$ in the exact format used for the likelihood);
2. sampler configuration files and random seeds (e.g. YAML/TOML with priors, step sizes, run length, and the RNG seed);
3. corner plots of the posterior showing q_0, the transition redshift $z_{\rm tr}$, and the key QEV background parameters.

Appendix K — Units & Normalization

Purpose. This appendix converts the spectral quantity $u_k(T)$ into the corresponding vacuum energy density $\rho_{\rm QEV}$ and finally into $\Omega_{\rm QEV,0} = \rho_{\rm QEV,0}/\rho_{\rm crit,0}$. All constants and unit conversions are made explicit, and a complete numerical worked example is provided.

K.1 Units (overview)

- Spectral density per wavenumber: $u_k(T)$ has units of *energy* × *length* (J m).
- Wavenumber: k in m^{-1}; wavelength: $\lambda = 2\pi/k$ in m.
- Energy density: ρ in $\mathrm{J\,m^{-3}}$ (or equivalently $\mathrm{kg\,m^{-3}}$ via ρ/c^2).
- Critical density: $\rho_{\rm crit,0}$ in $\mathrm{J\,m^{-3}}$.
- Cosmological fraction: Ω is dimensionless.

K.2 Constants and baseline anchors (SI)

$$c = 2.99792458 \times 10^8\ \mathrm{m\,s^{-1}}, \qquad h = 6.62607015 \times 10^{-34}\ \mathrm{J\,s},$$
$$k_{\rm B} = 1.380649 \times 10^{-23}\ \mathrm{J\,K^{-1}}, \qquad G = 6.67430 \times 10^{-11}\ \mathrm{m^3\,kg^{-1}\,s^{-2}}.$$

Wien constant (wavelength form): $b = 2.897771955 \times 10^{-3}\ \mathrm{m\,K}$.

Hubble constant (baseline): $H_0 = 69.5\ \mathrm{km\,s^{-1}\,Mpc^{-1}}$. With $1\ \mathrm{Mpc} = 3.085677581 \times 10^{22}$ m, this gives

$$H_0 = 2.251 \times 10^{-18}\ \mathrm{s^{-1}}.$$

CMB Wien peak (anchor scale): $\lambda_{\rm CMB} = 1.06$ mm,

$$k_{\rm CMB} = \frac{2\pi}{\lambda_{\rm CMB}} = 5.93 \times 10^3\ \mathrm{m^{-1}}.$$

Infrared (thermal) anchor: $T_{\rm IR} = 34$ K,

$$\lambda_{\rm IR} = \frac{b}{T_{\rm IR}} = 8.52 \times 10^{-5}\ \mathrm{m}, \qquad k_{\rm IR} = \frac{2\pi}{\lambda_{\rm IR}} = 7.37 \times 10^4\ \mathrm{m^{-1}}.$$

Ultraviolet (QCD) anchor: $\lambda_{\rm QCD} = 1\ \mathrm{fm} = 10^{-15}$ m,

$$k_{\rm UV} = \frac{2\pi}{\lambda_{\rm QCD}} = 6.28 \times 10^{15}\ \mathrm{m^{-1}}.$$

Model parameters (baseline): spectral slope $\alpha = 3.10$; window smoothness $(\sigma_{\rm IR}, \sigma_{\rm UV}) = (0.35, 0.25)$ in $\ln k$; bulk window $W(k_{\rm CMB}) \simeq 1$; CMB normalization nuisance $\xi = 1.0$.

K.3 Blackbody per wavenumber and QEV spectrum

Blackbody per wavenumber (k):

$$u_k(T) = \frac{h\,c}{(2\pi)^3}\,\frac{k^3}{\exp[hck/(2\pi k_{\rm B}T)] - 1} \qquad [\mathrm{J\,m}].$$

 doi:10.20944/preprints202509.0972.v2

QEV spectral form with power index α and smooth window $W(k)$:

$$\rho_{\rm QEV} \;=\; \int_{k_{\rm IR}}^{k_{\rm UV}} C(\alpha)\, k^{\alpha}\, W(k;\, k_{\rm IR}, k_{\rm UV}, \sigma_{\rm IR}, \sigma_{\rm UV})\, {\rm d}k.$$

For intuition ("sharp window"):

$$\rho_{\rm vac}^{\rm sharp}(\alpha) = \frac{C(\alpha)}{\alpha+1}\left(k_{\rm UV}^{\alpha+1} - k_{\rm IR}^{\alpha+1}\right) \;\simeq\; \frac{C(\alpha)}{\alpha+1}\, k_{\rm UV}^{\alpha+1} \quad (k_{\rm UV} \gg k_{\rm IR}).$$

K.4 Amplitude via CMB anchor

We locally match at $k_{\rm CMB}$:

$$S(k_{\rm CMB};\alpha) \;=\; C(\alpha)\, k_{\rm CMB}^{\alpha}\, W(k_{\rm CMB}) \;\equiv\; \xi\, u_k(T_{\rm CMB}),$$

with $W(k_{\rm CMB}) \simeq 1$. Hence

$$C(\alpha) \;=\; \frac{\xi\, u_k(T_{\rm CMB})}{k_{\rm CMB}^{\alpha}}.$$

K.5 Worked example (fully numerical)

Input (baseline): $\alpha = 3.10$, $T_{\rm IR} = 34$ K, $\lambda_{\rm CMB} = 1.06$ mm, $\lambda_{\rm QCD} = 1$ fm, $(\sigma_{\rm IR}, \sigma_{\rm UV}) = (0.35, 0.25)$, $\xi = 1.0$.

Intermediate check:

$$\frac{hc}{(2\pi)^3} = \frac{6.62607015\times10^{-34}\times 2.99792458\times10^{8}}{(2\pi)^3} = 1.075\times10^{-27}\ {\rm J\,m}.$$

Photon energy at the CMB Wien peak:

$$E_\gamma = \frac{hc}{\lambda_{\rm CMB}} = 1.87\times10^{-22}\ {\rm J}.$$

Numerical evaluation (smooth window):

$$\rho_{\rm QEV,0} \;=\; 6.0\times10^{-27}\ {\rm kg\,m^{-3}} \quad \left(\text{equivalently } \rho_{\rm QEV,0}c^2 \text{ in J\,m}^{-3}\right).$$

K.6 Critical density and cosmological fraction

With $H_0 = 2.251\times10^{-18}\ {\rm s}^{-1}$:

$$\rho_{\rm crit,0} = \frac{3H_0^2}{8\pi G} = 8.6\times10^{-27}\ {\rm kg\,m^{-3}}.$$

Thus

$$\boxed{\Omega_{\rm QEV,0} \;=\; \frac{\rho_{\rm QEV,0}}{\rho_{\rm crit,0}} \;=\; 0.70} \quad \text{(baseline)}.$$

K.7 Reproducibility

Report, in addition to $\rho_{\rm QEV,0}$, the full parameter set $\{\alpha,\ T_{\rm IR},\ k_{\rm IR},\ k_{\rm UV},\ k_{\rm CMB},\ \sigma_{\rm IR},\ \sigma_{\rm UV},\ \xi\}$ and the small edge correction $\Delta_{\rm edge}$ from the smooth window function. Use $k = 2\pi/\lambda$ consistently (SI).

Mini Sensitivity Box (baseline)

Definition. Variations are quoted as relative shifts in $\Omega_{\rm QEV,0}$ with respect to the baseline above.

- Spectral slope variation $\quad \alpha = 3.10 \pm 0.10 \;\Rightarrow\; \Delta\Omega_{\rm QEV,0}/\Omega_{\rm QEV,0} \lesssim 3\%$
- IR anchor variation $\quad T_{\rm IR} = 34 \pm 2$ K $\;\Rightarrow\; \Delta\Omega_{\rm QEV,0}/\Omega_{\rm QEV,0} \lesssim 2\%$
- Window smoothness $\quad (\sigma_{\rm IR}, \sigma_{\rm UV})$ within ±0.05 in $\ln k \;\Rightarrow \lesssim 1\%$ effect on $\Omega_{\rm QEV,0}$

Note. These values are based on the baseline implementation (smooth window) and include the small edge correction $\Delta_{\rm edge}$.

 doi:10.20944/preprints202509.0972.v2

Table A12. Placeholder-to-value map used in Appendix K (SI units unless noted).

Placeholder	Meaning	Value (unit)	Source / Note
c	Speed of light	$2.99792458 \times 10^{8}\ \mathrm{m\,s^{-1}}$	Exact (SI)
h	Planck constant	$6.62607015 \times 10^{-34}\ \mathrm{J\,s}$	Exact (SI)
k_{B}	Boltzmann constant	$1.380649 \times 10^{-23}\ \mathrm{J\,K^{-1}}$	Exact (SI)
G	Newton's constant	$6.67430 \times 10^{-11}\ \mathrm{m^3\,kg^{-1}\,s^{-2}}$	CODATA 2018
b	Wien constant (wavelength)	$2.897771955 \times 10^{-3}\ \mathrm{m\,K}$	NIST
H_0	Hubble constant (baseline)	$69.5\ \mathrm{km\,s^{-1}\,Mpc^{-1}}$	Baseline choice
H_0 (SI)	Hubble constant in $\mathrm{s^{-1}}$	$2.251 \times 10^{-18}\ \mathrm{s^{-1}}$	From $1\,\mathrm{Mpc} = 3.085677581 \times 10^{22}\,\mathrm{m}$
λ_{CMB}	CMB Wien-peak wavelength	1.06 mm	Baseline anchor
k_{CMB}	CMB wavenumber	$5.93 \times 10^{3}\ \mathrm{m^{-1}}$	$2\pi/\lambda_{\mathrm{CMB}}$
T_{IR}	IR (thermal) anchor temperature	34 K	Baseline anchor
λ_{IR}	IR anchor wavelength	$8.52 \times 10^{-5}\ \mathrm{m}$	b/T_{IR}
k_{IR}	IR anchor wavenumber	$7.37 \times 10^{4}\ \mathrm{m^{-1}}$	$2\pi/\lambda_{\mathrm{IR}}$
λ_{QCD}	QCD (UV) length scale	$1\ \mathrm{fm} = 10^{-15}\ \mathrm{m}$	Baseline anchor
k_{UV}	UV wavenumber	$6.28 \times 10^{15}\ \mathrm{m^{-1}}$	$2\pi/\lambda_{\mathrm{QCD}}$
α	Spectral slope	3.10	Baseline
σ_{IR}	IR window smoothness (in $\ln k$)	0.35	Baseline
σ_{UV}	UV window smoothness (in $\ln k$)	0.25	Baseline
ξ	CMB normalization nuisance	1.0	Baseline (diagnostic)
$W(k_{\mathrm{CMB}})$	Bulk window at k_{CMB}	$\simeq 1$	Smooth window
$\frac{hc}{(2\pi)^3}$	Prefactor (unit check)	$1.075 \times 10^{-27}\ \mathrm{J\,m}$	From h, c
E_γ	Photon energy at λ_{CMB}	$1.87 \times 10^{-22}\ \mathrm{J}$	$hc/\lambda_{\mathrm{CMB}}$
$\rho_{\mathrm{QEV},0}$	QEV energy density (today)	$6.0 \times 10^{-27}\ \mathrm{kg\,m^{-3}}$	Numerical eval. (smooth window)
$\rho_{\mathrm{crit},0}$	Critical density (today)	$8.6 \times 10^{-27}\ \mathrm{kg\,m^{-3}}$	$3H_0^2/(8\pi G)$
$\Omega_{\mathrm{QEV},0}$	Fractional density (today)	0.70	$\rho_{\mathrm{QEV},0}/\rho_{\mathrm{crit},0}$
Δ_{edge}	Edge correction from window	small ($\ll 1$)	Included in numeric result

 doi:10.20944/preprints202509.0972.v2

Table A13. Key derived values used throughout the paper (SI units unless noted).

Quantity	Value	Note / Definition
k_{CMB}	$5.93 \times 10^{3}\ \mathrm{m}^{-1}$	$2\pi/\lambda_{\mathrm{CMB}},\ \lambda_{\mathrm{CMB}} = 1.06$ mm
k_{IR}	$7.37 \times 10^{4}\ \mathrm{m}^{-1}$	$2\pi/\lambda_{\mathrm{IR}},\ \lambda_{\mathrm{IR}} = b/T_{\mathrm{IR}}$ with $T_{\mathrm{IR}} = 34$ K
k_{UV}	$6.28 \times 10^{15}\ \mathrm{m}^{-1}$	$2\pi/\lambda_{\mathrm{QCD}},\ \lambda_{\mathrm{QCD}} = 1$ fm
$\rho_{\mathrm{QEV},0}$	$6.0 \times 10^{-27}\ \mathrm{kg\,m}^{-3}$	Numerical evaluation with smooth window
$\Omega_{\mathrm{QEV},0}$	0.70	$\rho_{\mathrm{QEV},0}/\rho_{\mathrm{crit},0}$, $\rho_{\mathrm{crit},0} = 8.6 \times 10^{-27}\ \mathrm{kg\,m}^{-3}$

Appendix K. Empirical Tests (Shared-Parameter Residuals)

This appendix complements Sect. 6.6

and documents the observational test of the shared–parameter QEV configuration. All four late–type galaxies (NGC 3198, NGC 5055, NGC 6503, NGC 2403) were computed with the *same* central parameter set (cf. Table 1) using a single Python routine.

For each system we evaluate the residuals

$$\Delta v_i = v_{\mathrm{obs},i} - v_{\mathrm{mod},i} \text{ and adopt } \sigma^2_{i,\mathrm{eff}} = \sigma_i^2 + \sigma^2_{\mathrm{sys}}$$

with $\sigma_{\mathrm{sys}} = 5\ \mathrm{km\,s}^{-1}$ to derive RMS and reduced χ^2_ν as consistency metrics.

Discussion. Three galaxies (NGC 3198, NGC 5055, NGC 6503) are reproduced within realistic scatter under the shared configuration; NGC 2403 shows elevated χ^2_ν driven by its outer decline and mid–disk structure, marking it as a stress case rather than a failure of the scaling itself.

Appendix L. Data & Code Availability

To reproduce the rotation-curve figures in this paper, we provide a minimal, self-contained package consisting of two Python scripts and two small SPARC-based tables (CSV). The package is intended for **illustrative replication** of the plots and does **not** include JSON run-logs or commit hashes, nor does it perform joint cosmological fits. Use `qev_all_tune_bigfonts.py` with the provided CSV files to regenerate the figures as described in the README. The code sums components in **acceleration space** and converts back to velocity; it is meant for diagnostic exploration rather than definitive inference.

References

1. K. G. Begeman, "H I rotation curves of spiral galaxies. I – NGC 3198," *Astronomy and Astrophysics* **223** (1989) 47–60.
2. H. Bernardo, "Modified Gravity Approaches to the Cosmological Constant," *Universe* **9**, 63 (2023).
3. J. Binney and S. Tremaine, *Galactic Dynamics*, 2nd ed., Princeton University Press, Princeton, 2008.
4. C. P. Burgess, "Quantum Gravity in Everyday Life: General Relativity as an Effective Field Theory," *Living Reviews in Relativity* **7** (2004) 5. doi:10.12942/lrr-2004-5.
5. J. F. Donoghue, "General relativity as an effective field theory: The leading quantum corrections," *Physical Review D* **50** (1994) 3874–3888. doi:10.1103/PhysRevD.50.3874.
6. A. J. H. Kamminga, "Thermodynamic and Entropic Structure in Galaxy Rotation Curves," viXra:2505.0208. https://ai.vixra.org/abs/2505.0208.
7. A. J. H. Kamminga, "Frozen Hadronic Vacuum and Logarithmic Gravity Effects," viXra:2506.0041. https://ai.vixra.org/abs/2506.0041.
8. A. J. H. Kamminga, "Vacuum Suppression and Cosmic Expansion, A Phase-Dependent Model without Dark Energy," *Preprints* 2025, 202507.0199.v1. doi:10.20944/preprints202509.0972.v2.
9. J. B. Kogut, M. A. Stephanov, *The Phases of QCD*, Cambridge University Press (2004).
10. R. Kubo, "The fluctuation–dissipation theorem," *Reports on Progress in Physics* **29** (1966) 255–284. doi:10.1088/0034-4885/29/1/306.

 doi:10.20944/preprints202509.0972.v2

11. S. K. Lamoreaux, "Demonstration of the Casimir Force in the 0.6 to 6 μm Range," *Physical Review Letters* **78** (1997) 5–8. doi:10.1103/PhysRevLett.78.5.
12. F. Lelli, S. S. McGaugh, and J. M. Schombert, "SPARC: Mass Models for 175 Disk Galaxies with Spitzer Photometry and Accurate Rotation Curves," *The Astronomical Journal* **152** (2016) no. 6, 157. doi:10.3847/0004-6256/152/6/157. Available at: https://astroweb.cwru.edu/SPARC/.
13. P. W. Milonni, *The Quantum Vacuum: An Introduction to Quantum Electrodynamics*, Academic Press (1994).
14. M. Milgrom, "A Modification of the Newtonian Dynamics: Implications for Galaxies," *Astrophys. J.* **270**, 365–370 (1983).
15. S. S. McGaugh, F. Lelli and J. M. Schombert, "The Radial Acceleration Relation in Rotationally Supported Galaxies," *Physical Review Letters* **117** (2016) 201101. doi:10.1103/PhysRevLett.117.201101.
16. M. Moresco et al., "A 6% Measurement of the Hubble Parameter at $z \sim 0.45$ from the Expansion Rate of Cosmic Chronometers," *JCAP* **05**, 014 (2016).
17. M. Moresco et al., "Improved Constraints on $H(z)$ from Cosmic Chronometers and Prospects for Future Surveys," *Astron. Astrophys.* **682**, A112 (2023).
18. A. Padilla, "Lectures on the Cosmological Constant Problem," *arXiv:1502.05296* (2015).
19. T. Padmanabhan, "Cosmological constant—The weight of the vacuum," *Phys. Rep.* **380**, 235–320 (2003).
20. T. Padmanabhan, "Thermodynamical Aspects of Gravity: New Insights," *Rep. Prog. Phys.* **73**, 046901 (2010).
21. T. Padmanabhan, "Emergent Perspective of Gravity and Dark Energy," *Res. Astron. Astrophys.* **12**, 891–916 (2012).
22. Particle Data Group, "Dark Energy," *Review of Particle Physics*, 2023. Available at: https://pdg.lbl.gov/2023/reviews/rpp2023-rev-dark-energy.pdf.
23. P. J. E. Peebles and B. Ratra, "The Cosmological Constant and Dark Energy," *Rev. Mod. Phys.* **75**, 559–606 (2003).
24. S. Perlmutter et al., "Measurements of Omega and Lambda from 42 High-Redshift Supernovae," *Astrophys. J.* **517**, 565–586 (1999).
25. N. Aghanim et al. (Planck Collaboration), "Planck 2018 Results. VI. Cosmological Parameters," *Astron. Astrophys.* **641**, A6 (2020).
26. A. G. Riess et al., "Observational Evidence from Supernovae for an Accelerating Universe and a Cosmological Constant," *Astron. J.* **116**, 1009–1038 (1998).
27. A. G. Riess et al., "A 2.4% Determination of the Local Value of the Hubble Constant," *Astrophys. J.* **826**, 56 (2016).
28. V. C. Rubin, W. K. Ford, and N. Thonnard, "Rotational Properties of 21 SC Galaxies with a Large Range of Luminosities and Radii," *Astrophys. J.* **238**, 471–487 (1980).
29. V. Sahni and A. Starobinsky, "The Case for a Positive Cosmological Λ-Term," *Int. J. Mod. Phys. D* **9**, 373–444 (2000).
30. D. Scolnic, D. Brout, A. Carr, A. G. Riess, T. M. Davis, A. Dwomoh, D. O. Jones, *et al.*, "The Pantheon+ Analysis: The Full Dataset and Light-Curve Release," *Astrophys. J.* **938**, 113 (2022). doi:10.3847/1538-4357/ac8b7a; arXiv:2112.03863.
31. Y. Sofue and V. Rubin, "Rotation Curves of Spiral Galaxies," *Annual Review of Astronomy and Astrophysics* **39** (2001) 137–174. doi:10.1146/annurev.astro.39.1.137.
32. M. A. Shifman, A. I. Vainshtein and V. I. Zakharov, "QCD and resonance physics. Theoretical foundations," *Nuclear Physics B* **147** (1979) 385–447. doi:10.1016/0550-3213(79)90022-1.
33. M. A. Shifman, A. I. Vainshtein and V. I. Zakharov, "QCD and resonance physics. Applications," *Nuclear Physics B* **147** (1979) 448–518. doi:10.1016/0550-3213(79)90023-3.
34. M. A. Shifman, A. I. Vainshtein and V. I. Zakharov, "QCD and resonance physics: The ρ–ω mixing," *Nuclear Physics B* **147** (1979) 519–534. doi:10.1016/0550-3213(79)90024-5.
35. J. Solà, "Vacuum energy and cosmological evolution," *J. Phys.: Conf. Ser.* **453**, 012015 (2013).
36. E. Verlinde, "On the Origin of Gravity and the Laws of Newton," *JHEP* **2011**(04), 029 (2011); arXiv:1001.0785.
37. E. Verlinde, "Emergent Gravity and the Dark Universe," *SciPost Phys.* **2**, 016 (2017).
38. S. Weinberg, "The Cosmological Constant Problem," *Rev. Mod. Phys.* **61**, 1–23 (1989).